Dissertation

The response of insulator surfaces to a slowly approaching highly charged ion

ausgeführt zum Zwecke der Erlangung des akademischen Grades eines
Doktors der technischen Wissenschaften
unter der Leitung von

Univ.-Prof. Dr. Friedrich Aumayr
E134
Institut für Allgemeine Physik

eingereicht an der Technischen Universität Wien
Technisch-Naturwissenschaftliche Fakultät

von

Dipl.-Ing. Walter Meissl
Mat.Nr.: 9730415
Dittesgasse 16/9, 1180 Wien

Wien, am 29. Oktober 2008

für meine Frau, Elfi,

die bei aller Wissenschaft

das spannendste Rätsel

in meinem Leben geblieben ist

Kurzfassung

Die vorliegende Dissertation behandelt die Wechselwirkung hochgeladener Ionen mit Isolatoroberflächen. Ionenstrahlen sind im Moment ein rasch an Bedeutung gewinnendes Mittel zur Oberflächenmodifikation, dabei aber gleichzeitig das womöglich am wenigsten entwickelte der modernen Werkzeuge zur Nanostrukturierung bei industrierelevanten Anwendungen.

Mithilfe von Rasterkraftmikroskopie wurde nachgewiesen, dass einzelne hochgeladene Ionen echt-topographische Strukturen im Nanometerbereich auf Kalziumfluorid-Einkristalloberflächen erzeugen können. Die erzeugten Oberflächendefekte zeigten nur eine schwache Abhängigkeit von der kinetischen Energie der Projektile im Bereich von einigen keV bis über 300 keV, jedoch eine starke Abhängigkeit von deren potentieller Energie. Ein Schwellwert in der potentiellen Energie zwischen 12 und 14 keV konnte für das Auftreten der Strukturen nachgewiesen werden. Langsame Elektronen, die vom Projektil in den Festkörper emittiert werden, führen zu einer Erhitzung des Kristallgitters in der unmittelbaren Umgebung des Einschlags. Dies ruft einen Phasenübergang (Schmelzen) im Nanometerbereich hervor, der für das Erzeugen der Strukturen verantwortlich gemacht werden konnte. Nanostrukturen wurden nach dem Beschuss nur für den Fall, dass die eingebrachte Energie pro Targetatom die lokale Schmelzwärme übersteigt, gefunden. Da Kalziumfluorid epitaktisch auf Silizium-Einkristalloberflächen wächst und als Isolator in der Halbleiterindustrie verwendet wird, könnten die vorliegenden Ergebnisse zur künftigen Verwendung hochgeladener Ionen in der Mikroelektronik-Produktion beitragen.

Um den Weg für den Einsatz hochgeladener Ionen als Werkzeug zur Nanostrukturierung in industrierelevanten Anwendungen zu ebnen, ist eine einfache Demonstration der Möglichkeit von Oberflächenmodifikation mit Hilfe der potentiellen Energie der Projektile nicht genug. Um für die Industrie attraktiv zu werden, wird ein tieferes Verständnis des Wechselwirkungsprozesses angestrebt, um die Resultate der Bestrahlung mit hochgeladenen Ionen den vordefinierten Erwartungen anpassen zu können.

Die Emission von Elektronen während des Einfalls hochgeladener Ionen auf einen Festkörper erlaubt Einsichten in die relevanten Prozesse der elektronischen Evolution von Projektil und Oberfläche. Im Rahmen dieser Arbeit wurde ein neuer Apparat zur quantitativen Bestimmung der Elektronenausbeute beim Einschlag von extrem langsamen hochgeladenen Ionen auf Isolator-oberflächen konstruiert. Mit diesem Apparat wurden Elektronenausbeuten beim Einschlag hoch-geladener Argon-, Xenon- und Quecksilberionen (in Ladungszuständen bis hinauf zu 64+) auf Isolator-oberflächen gemessen und ihre Abhängigkeit von Ladungszustand, Geschwindigkeit und Winkel bestimmt. Die erhaltenen Daten zeigen, dass die Interaktionszeit vor der Oberfläche für moderat langsame Projektile bei weitem nicht ausreicht, um die elektronische Evolution des Systems abzuschließen. Ein immer noch hochgeladenes Projektil tritt in den Festkörper ein und trägt durch Elektronenemission unterhalb der Oberfläche in signifikantem Ausmaß zur Gesamtausbeute bei. Im Vergleich zu leitenden Oberflächen wurde nur eine schwache Abhängigkeit der Ausbeute von der Geschwindigkeit bis hinunter zu etwa 10^5 ms^{-1} gefunden. Darunter zeigte sich für die höchsten Projektil-Ladungszustände ein starker Abfall der Ausbeute am Isolatortarget. Als mögliche Erklärung wird die Zurückhaltung langsamer, andernfalls emittierter, Elektronen durch eine Ansammlung positiver Ladungen auf der Oberfläche, die beim Einschlag gebildet werden, präsentiert.

Abstract

The present thesis deals with the interaction of slow highly charged ions (HCI) with insulator surfaces. Ion beams are a rapidly emerging tool for surface modifications and probably the least developed of the current techniques for nanostructuring in industry relevant applications.

Using atomic force microscopy, single impact of slow highly charged xenon ions was proven to induce stable and truly topographic nanometric surface structures CaF_2 single crystal surfaces. The surface defects showed only a weak dependence on the projectile's kinetic energy in the range of a few keV up to more than 300 keV, but a strong dependence on the potential energy of the ions. A threshold in potential energy of the projectile between 12 and 14 keV was found for the onset of nanostructuring. The mechanism behind the production of these structures was identified as a phase-transition (melting) on the nano-scale induced by the emission of electrons into the solid, which leads to heating of the lattice in the immediate vicinity. Nanostructures were only found when the energy per atom delivered to the lattice exceeded the melting temperature. CaF_2 can be grown epitaxially on silicon surfaces and is an insulator used by the semiconductor industry; therefore the present findings may lead to future application of HCI in microelectronics production.

To pave the way for HCI as a new tool for nanostructuring in industry-relevant applications, a simple demonstration of surface modifications by the potential energy of the projectile is not deemed enough. In order to become attractive for industry, a deeper understanding of the interaction process is necessary, which then allows tuning the results of HCI irradiation in the correct way to meet predefined expectations.

The emission of electrons during HCI impact on a surface allows insights in the relevant processes of the electronic evolution of the projectile and the surface. A new setup was constructed for the determination of electron yields during impact of extremely slow HCI on insulating targets. For highly charged argon, xenon and mercury ions up to charge states of 64+, electron yields were obtained for impact on an insulating LiF surface and their dependence on charge state, velocity and impact angle analyzed. The acquired data show that for moderately slow HCI, the interaction time of the ion above the surface is by far insufficient for the electronic evolution of the projectile to finish. A still highly excited projectile penetrates the surface and leads to a significant contribution of below-surface electron emission to total yields. Compared to conducting targets, only a weak dependence of the electron yield on the impact velocity was found above approximately 10^5 ms^{-1}. For the highest charge state used (40+), a sharp drop of the electron yield was observed for the insulator at very low impact velocities. The retention of slow, otherwise emitted, electrons by a positive charge patch formed on the insulating surface during HCI impact is considered to be a possible explanation of the observed drop.

table of contents

Kurzfassung iii

Abstract iv

1 Introduction 1

1.1 List of Publications 2

1.2 Conference Participation 3

1.3 List of Abbreviations 5

2 State of the Art 6

2.1 Highly Charged Ions 6

2.1.1 Hollow Atoms 9

2.1.2 Trampoline Effect 10

2.1.3 Sources for Highly Charged Ions 11

2.1.3.1 The Heidelberg Electron Beam Ion Trap 11

2.1.3.2 The Dresden Electron Beam Ion Trap 12

2.2 Nanostructuring of Surfaces 14

2.2.1 Swift Heavy Ion Irradiation 15

2.2.2 Slow Highly Charged Ion Irradiation 16

2.2.2.1 Mica 16

2.2.2.2 Graphite 17

2.2.2.3 Silicon 19

2.2.2.4 Titanium Oxide 19

2.3 Electron emission studies 20

2.3.1 Classification 20

2.3.2 Total Electron Yields from Conducting Targets 20

2.3.3 Total Electron Yields from Insulating Targets 22

3 Nanostructuring of Calcium Fluoride 25

3.1 Experimental Methods 25

3.1.1 Irradiation target holder 25

3.1.2 Atomic Force Microscopy 27

3.2 Results and Discussion 31

3.2.1 Hillocks 31

3.2.2 Potential Energy Threshold 33

3.2.2.1 Experimental Evidence 33

3.2.2.2 Discussion 35
3.2.3 Dependence on the Ion's Impact Velocity 38
3.2.3.1 Experimental Evidence 38
3.2.3.2 Discussion 40
3.3 Comparison 43
4 Electron Emission 45
4.1 Experimental Methods 45
4.1.1 Electron Number Statistics 45
4.1.2 Improved Data Analysis 48
4.1.3 Electron Collection Geometries 49
4.1.3.1 Simulations 50
4.1.3.2 Fountain-type 51
4.1.3.3 90° type 53
4.1.3.4 Curtain type 55
4.1.4 Ion Beam Scan Electronics 59
4.1.5 Timing Electronics 62
4.2 Results and Discussion 64
4.2.1 qRIBS - A Novel Tool for Ion Beam Analysis 64
4.2.2 Charging Effects 67
4.2.3 Electron Emission at Moderate Impact Velocities 69
4.2.3.1 Conducting Targets 69
4.2.3.2 Insulating Targets 72
4.2.3.3 Above and Below Surface Electron Emission 75
4.2.4 Electron Emission at Very Low Impact Velocity 78
4.2.4.1 Reliability of the Setup 78
4.2.4.2 Electron yields 82
4.2.4.3 Interpretation 87
4.2.5 Time Structure Analysis 92
5 Conclusions and Outlook 97
6 Acknowledgements 99
7 References 101

"Good news, everyone!"
Prof. Hubert Farnsworth of futurama
created by Matt Groening

1 Introduction

The present thesis comprises results from work performed in the group of Prof. Friedrich Aumayr at the Institut für Allgemeine Physik of Vienna University of Technology, Austria in the years 2004 to 2008. During this PhD work, several diploma students have participated in these experiments and thereby contributed greatly to the successes and results that were achieved. Their respective diploma theses often describe some of the experiments performed in greater detail than the present document, which focuses more on the achieved results and their discussion. For a full understanding of the experimental methods used, the following diploma theses are highly recommended

- **Martin Simon**, *"Elektronen Emission bei Beschuss von Isolator- und Metall-Oberflächen mit hochgeladenen Ionen"* [1] (in German) deals with the determination of electron yields for impact of moderately slow highly charges ion (HCI) on insulator surfaces (c.f. chapter 4.2.3) and gives a detailed description of the electron beam ion trap (EBIT) in Heidelberg
- **Robert Ritter**, "*Ion-induced surface modifications investigated with scanning probe microscopies*" [2]. Deals with irradiation of mica and HOPG (graphite) samples by slow HCI and the observation of induced surface defects (c.f. chapter 2.2.2) and contains a detailed introduction to atomic force microscopy (AFM).
- **Daniel Winklehner**, "*Electron Emission from Insulators upon Impact of Highly Charged Ions*" [3] deals with electron emission at very slow HCI impact on insulator surfaces (c.f. chapter 4.2.4) and contains a detailed description of the EBIT at the Forschungszentrum Dresden (FZD – Dresden research center) as well as a thorough introduction into the electronics used for the determination of electron yields.

The present work deals with different aspects of the interaction of slow highly charged ions with insulator surfaces. It is split up into two relatively disjunct parts:

- Nanostructuring of surfaces, studied by AFM of irradiated surfaces *after* exposure to HCI.
- Electron emission, studied by an electron detector *in situ* during HCI irradiation.

Although both phenomena are the result of slow HCI irradiation of insulating targets, the experimental methods and observed results differ considerably. To increase the readability of the present document, they are treated in separate sections (3 and 4), where each is again subdivided into experimental methods and results. As the projectiles of choice for both parts (HCI) were obtained from the same type of ion source, the electron beam ion trap (EBIT), this is treated in chapter 2.1.3, not in the experimental methods. Section 2 is a general chapter aimed at providing an overview of the relevant accumulated scientific knowledge at the time this PhD work started, to put the achieved results into a proper perspective.

1.1 List of Publications

Several publications resulted from the present PhD work, and parts of this thesis have been taken from these papers. However, not all of the work that was carried out is described in this thesis.

- A.S. El-Said, R. Heller, **W. Meissl**, R. Ritter, S. Facsko, C. Lemell, B. Solleder, I.C. Gebeshuber, G. Betz, M. Toulemonde, W. Möller, J. Burgdörfer, and F. Aumayr
  Nano-hillocks on CaF_2 surfaces created by the potential energy of slow highly charged projectile ions [4]
  Physical Review Letters **100** (2008) 237601

- **W. Meissl**, D. Winklehner, F. Aumayr, M.C. Simon, R. Ginzel, J.R. Crespo López-Urrutia, J. Ullrich, B. Solleder, J. Burgdörfer
  Electron emission from insulators irradiated by slow highly charged ions [5]
  e-Journal of Surface Science and Nanotechnology **6** (2008) 54 - 59

- S. Facsko, R. Heller, A.S. El-Said, **W. Meissl**, F. Aumayr
  Surface Nanostructures by Single Highly Charged Ions (review paper)
  J. Phys.: Condens. Matter (in print)

- F. Aumayr, A. S. El-Said, and **W. Meissl**
  Nano-sized surface modifications induced by the impact of slow highly charged ions – a first review (review paper) [6]
  Nuclear Instruments and Methods in Physics Research B **266** (2008) 2729 - 2735

- C. Lemell, A. S. El-Said, **W. Meissl**, I. C. Gebeshuber, C. Trautmann, M. Toulemonde, J. Burgdörfer, and F. Aumayr
  On the nano-hillock formation induced by slow highly charged ions on insulator surfaces [7]
  Solid State Electronics **51** (2007) 1398-1404

- M. Fürsatz, **W. Meissl**, S. Pleschko, I. C. Gebeshuber, N. Stolterfoht, HP. Winter, and F. Aumayr
  Charging and discharging of nano-capillaries during ion-guiding of multiply charged projectiles [8]
  Journal of Physics: Conference Series **58** (2007) 319 – 322

- A. S. El-Said, **W. Meissl**, M. C. Simon, J. R. Crespo López-Urrutia, I. C. Gebeshuber, J. Laimer, HP. Winter, J. Ullrich, and F. Aumayr
  Creation of surface nanostructures by irradiation with slow highly charged ions [9]
  Radiation Effects & Defects in Solids **162** (2007), 467–472

- A. S. El-Said, **W. Meissl**, M.C. Simon, J. R. Crespo López-Urrutia, C. Lemell, I. C. Gebeshuber, HP. Winter, J. Ullrich, C. Trautmann, M. Toulemonde, and F. Aumayr
  Potential energy threshold for nanohillock formation by impact of slow highly charged ions on a CaF_2(111) surface [10]
  Nuclear Instruments and Methods in Physics Research B: **258** (2007) 167-171

- A. S. El-Said, **W. Meissl**, M. C. Simon, J.R. Crespo López-Urrutia, I. C. Gebeshuber, M. Lang, HP. Winter, J. Ullrich, and F. Aumayr
  Surface nanostructures induced by slow highly charged ions on CaF_2 single crystals [11]
  Nuclear Instruments and Methods in Physics Research B **256** (2007) 346 - 349

- **W. Meissl**, M. C. Simon, J. R. Crespo López-Urrutia, H. Tawara, J. Ullrich, HP. Winter, and F. Aumayr
  Highly charged ion induced potential electron emission from clean Au (111): Dependence on the projectile angle of incidence [12]
  Nuclear Instruments and Methods in Physics Research B **256** (2007) 520-523

- **W. Meissl**, M. C. Simon, J. R. Crespo López-Urrutia, H. Tawara, J. Ullrich, HP. Winter, and F. Aumayr
  Novel method for unambiguous ion identification in mixed ion beams extracted from an electron beam ion trap [13]
  Review of Scientific Instruments **77** (2006) 093303 (4 pages)

- F. Aumayr, J. Stöckl, M. Fürsatz, **W. Meissl**, and HP. Winter
  Interaction of slow multiply charged Ar ions with a LiF insulator surface [14]
  e-Journal of Surface Science Nanotechnology. 4 (2006) 388 - 393

1.2 Conference Participation

The present work has already been presented orally or as a poster by the author of this thesis on several international conferences and workshops:

- **W. Meissl**:
  Response of insulator surfaces to a very slowly approaching highly charged ion
  invited progress report at the 14th Intern. Conf. on the Physics of Highly Charged Ions (HCI-2008), University of Electro-Communications, Chofu, Tokyo/Japan (invited); 09-01-2008

- **W. Meissl**, D. Winklehner, R. Heller, S. Facsko, W. Möller, and F. Aumayr:
  Electron emission from insulators bombarded with very slow highly charged ions
  Poster: 14th Intern. Conf. on the Physics of Highly Charged Ions (HCI-2008), University of Electro-Communications, Chofu, Tokyo/Japan; 09-02-2008

- **W. Meissl**, R. Heller, A.S. El-Said, M. Simon, R. Ritter, S. Facsko, I. Gebeshuber, J.R. Crespo López-Urrutia, W. Möller, J. Ullrich, F. Aumayr:
  Nano-hillocks on CaF_2 surfaces created by the potential energy of slow highly charged projectile ions
  Poster: Symposion on Surface Science 2008 (3S08), St. Christoph am Arlberg; 03-04-2008

- **W. Meissl**, M. Simon, J.R. Crespo López-Urrutia, J. Ullrich, and F. Aumayr:
  Electron emission from highly charged ion irradiated alkali-halide targets
  Poster: 6th Intern. Symposium on Atomic Level Characterizations for New Materials and Devices (ALC'07), Kanazawa, Ishikawa/Japan; 10-30-2007

- **W. Meissl**:
  Identification and application of highly charged ions extracted from an EBIT
  Talk: 10th Intern. Symp. on the Physics and Applications of Electron Beam Ion Sources and Traps (EBIS/T), Heidelberg/D; 08-03-2007

- **W. Meissl**, M. Simon, J.R. Crespo López-Urrutia, H. Tawara, J. Ullrich, and F. Aumayr:
  Electron emission from insulator surfaces induced by impact of slow highly charged ions
  Poster: 25th Intern. Conf. on Photonic, Electronic and Atomic Collisions (XXV ICPEAC), Freiburg/Breisgau/D; 07-27-2007

- **W. Meissl**, M. Simon, HP. Winter, F. Aumayr, B. Solleder, C. Lemell, J. Burgdörfer, J.R. Crespo López-Urrutia, H. Tawara, J. Ullrich:
  Electron emission from insulator surfaces induced by impact of slow highly charged ions
  Poster: 16th Intern. Workshop on Inelastic Ion-Surface Collisions (IISC-16), Hernstein/NÖ; 09-21-2006

- **W. Meissl**, M. Fürsatz, S. Pleschko, M. Simon, I. Gebeshuber, N. Stolterfoht, HP. Winter, F. Aumayr:
  Charging and discharging of nano-capillaries during ion-guiding of multiply charged projectiles
  Poster: 16th Intern. Workshop on Inelastic Ion-Surface Collisions (IISC-16), Hernstein/NÖ; 09-19-2006

- **W. Meissl**, M. Simon, J.R. Crespo López-Urrutia, H. Tawara, J. Ullrich, HP. Winter, and F. Aumayr:
  Electron emission from insulator surfaces induced by impact of slow highly charged ions
  Poster: 22th Int. Conf. on Atomic Collisions in Solids (ICACS-2006), Berlin/D; 07-25-2006.

- **W. Meissl**, A.S. El-Said, M. Simon, J.R. Crespo López-Urrutia, H. Tawara, HP. Winter, M. Lang, and F. Aumayr:
  Surface modifications on and electron emission from insulator surfaces induced by impact of slow highly charged ions
  Poster: Symp. on Surface Science 2006 (3S'06), St. Christoph am Arlberg; 03-07-2006

1.3 List of Abbreviations

The following is a list of abbreviations commonly used throughout the document:

ADC	analog-to-digital converter
AFM	atomic force microscopy
CaF_2	Calcium Fluoride
COB	classical-over-the-barrier model
E_{kin}	kinetic energy
E_{pot}	potential energy
EBIT	electron beam ion trap
FZD	Forschungszentrum Dresden in Rossendorf
HA	hollow atom
HCI	highly charged ion
HOPG	highly oriented pyrolytic graphite
KBr	Potassium-Bromide
KE	kinetic electron emission
LiF	Lithium-Fluoride
MCA	multi-channel-analyzer
PE	potential electron emission
PIPS	planar implanted passivated silicon (detector)
SCA	single-channel-analyzer
STM	scanning tunneling microscope
TAC	time-to-amplitude converter
UHV	ultra-high vacuum

"You win again, gravity!"
Zapp Brannigan of futurama,
crashing another spaceship

2 State of the Art

Impact of slow ions (impact velocity < 1 a.u. = 25 keV/amu) on solid surfaces is of genuine interest in plasma- and surface physics and related applications [12]. Nature and intensity of the resulting inelastic processes depend both on the kinetic and the potential (= internal) ion energy carried towards the surface. For most practical applications as, e.g., ion-induced kinetic electron emission (KE [15-18]) or ion-surface scattering and kinetic sputtering [19, 20], the kinetic projectile energy is of primary importance. However, ion-induced processes may also depend on the internal (potential) projectile energy, in particular if the latter exceeds the kinetic projectile energy. This will give rise to further electron emission (potential electron emission PE [18, 21-25]) and for certain target materials also to a special kind of sputtering (potential sputtering [26-28]) as well as nano-sized surface damage [4, 6, 29].

High-energy photons, electrons, and ions are frequently employed as tools to lithographically modify surfaces on the nanometer scale [4]. Among them, ion beams are, perhaps, still the least developed technique in the field of nano-lithography, in part due to the fact that many fundamental aspects of their interactions with the surface are not yet well understood. Three techniques, focused ion beam, proton beam writing and ion projection lithography, have now breached the technologically difficult 100 nm barrier, and are capable of fabricating structures on the nano-scale [30]. Current research in the field of advanced ion-beam technique focuses on the energy and charge state dependence of the primary beam. While the interaction of intense beams of keV ions with surfaces can result in well-ordered patterns, such as ripples or self-ordered dots [31-33], drastic modifications to the surface topography by individual ions are only induced if the material is exposed to energetic ions (MeV to GeV region). At these high impact energies the energy deposition leads to the creation of nano-sized hillocks or craters randomly distributed on the surface. Recently, the formation of multiple, regularly spaced nanodots on $SrTiO_3$ surfaces has been demonstrated for single swift Xe ion impact under grazing angles of incidence [34].

2.1 Highly Charged Ions

Considerable potential energy is being stored in a highly charged ion (HCI) Z^{q+} during its production when q electrons are removed from an originally neutral particle, e.g. 14 keV for bare Ar^{18+}, 121 keV for He-like Xe^{52+} and 250 keV for Ne-like Th^{80+} (see Fig. 2.1-1) [12].

This potential energy is released again when the HCI is neutralized at a solid surface. According to the currently accepted scenario [23, 25, 28, 35, 36], the approach of very slow highly charged ion is governed at first by the image charge acceleration of the projectile towards the surface. This acceleration defines a minimum kinetic energy that the HCI can have on its final approach (see Fig. 2.1-2). HCI neutralization then starts with the formation of a transient, multiply-excited particle with some empty inner shells, which has been called „hollow atom"(HA) (see next chapter). For metal

target surfaces, the above surface part of this interaction can be well described by the so-called "classical over-barrier model" (COB) [35] and leads to the emission of a large number of low energy electrons. As soon as the HA approaches closely the surface, it will be screened by the metal electron gas which further accelerates its deexcitation. Inside the solid until now surviving inner shell vacancies of the strongly screened HA will recombine by emission of projectile-characteristic fast Auger electrons and/or soft X-rays, depending on the respective fluorescence yield.

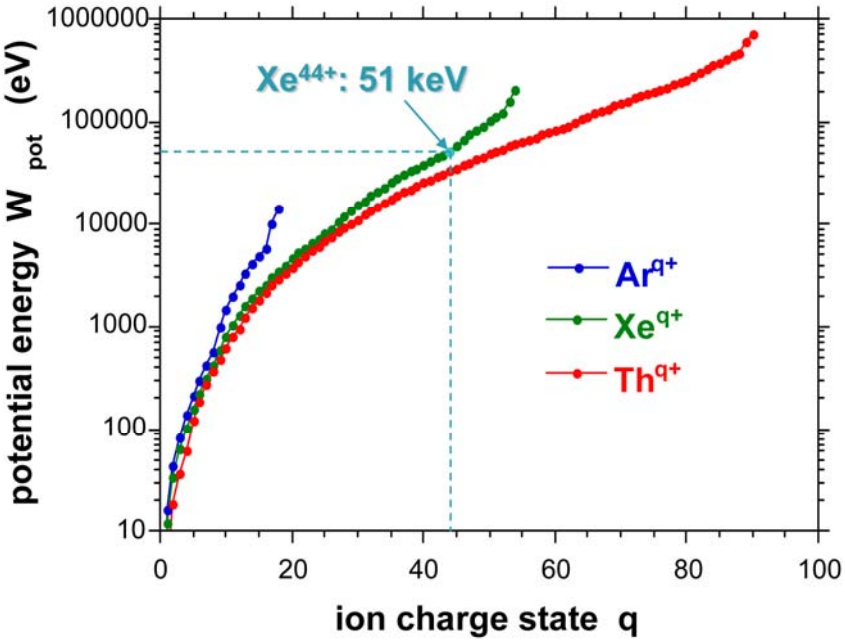

Fig. 2.1-1: The potential energy of highly charged ions is plotted versus their charge state for different ion species. Xe^{44+} with a potential energy of 51 keV is highlighted [28].

For metal surfaces these processes could largely be identified by experimental and theoretical investigations during the last two decades [23, 25, 36, 37]. Similar processes for semiconductor and insulator targets, however, are not as well understood. The possibility of exploiting the huge amount of potential energy stored in HCI for nano-fabrication has captured the imagination of researchers for some time [38]. Electronic processes induced by very slow (close to the image charge acceleration limit) HCI are limited to the uppermost layers of a solid. With decreasing dimensions of semiconductor devices, processes at the surface become increasingly important. Slow HCI could thus provide unique opportunities for etching, ultra-thin-film growth and nanostructuring. While nanostructures produced by kinetic sputtering by and implantation of fast ions are subject to unwanted radiation damage to deeper layers, potential sputtering and surface nano-defect production by slow HCI promises a much gentler nanostructuring tool. CaF_2, which was used as the primary target material for nano-defect studies in this work, can be grown epitaxially on Si single-crystals; therefore the present thesis might be of interest for future applications in the semiconductor industry.

To be useful as a tool for nanostructuring, the kinetic energy of the HCI has to be sufficiently low so that they only interact with the first few atomic layers of the target material without penetrating the bulk and inducing radiation damage there. One of the central questions of this thesis is therefore: “what is the minimum impact energy of a highly charged ion impinging on an insulator surface?” For

different reasons, the answer to this question cannot simply be deduced from the present knowledge of HCI – metal interactions:

- The dielectric response of insulating surfaces (image charge acceleration, hole mobility, etc…) is quite different from that of a metallic target, resulting in new phenomena observable in experiment and (due to their complexity) posing a considerable challenge to theory
- Electron transfer from an insulator to a highly charged projectile can lead to local charging-up of the surface. The image charge acceleration usually observed for metal surfaces could thus be altered or even overcome, leading to a repulsion of the projectile by the positive hole charges on the surface ("trampoline effect" [39], c.f. chapter 2.1.2)
- The wide electronic band gap will affect and alter electronic transfer, emission and excitation processes as compared to conducting surfaces

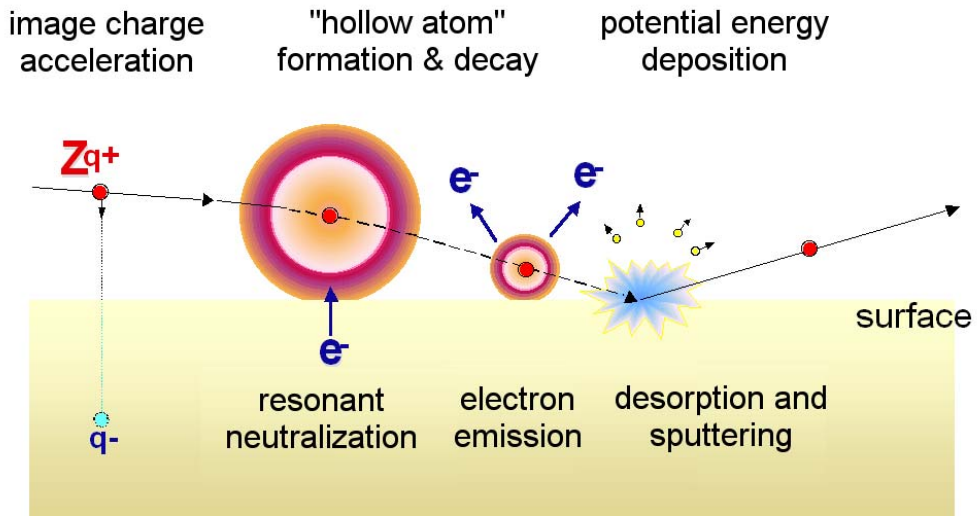

Fig. 2.1-2: The commonly accepted model for highly charged ion impact on metal surfaces. For explanations of the different processes c.f. text [28].

The present thesis aims at testing slow HCI for their abilities as gentle tools for nanostructuring. The atomic force microscopy investigations of irradiated surfaces presented in chapter 3 can determine the conditions under which HCI induce nanostructures on insulator surfaces. Electron emission measurements presented in chapter 4 are performed in order to get a deeper understanding of the HCI-insulator interaction.

2.1.1 Hollow Atoms

The classical-over-the-barrier (COB) model developed by Burgdörfer [35-37] predicts first quasi-resonant electronic transitions from the surface to the HCI to arise at a critical distance R_c into highly exited projectile states with hydrogenic principal quantum numbers n_c.

$$R_c \approx \frac{(2q)^{1/2}}{W_\Phi} \qquad (1)$$

$$n_c \approx \frac{q^{3/4}}{W_\Phi^{1/2}} \qquad (2)$$

where q is the projectile charge state and W_φ is the work function of the material. Both equations use atomic units. For fully stripped Ar^{18+} ions on Al(111) (W_φ = 0.16 a.u.) the COB model predicts R_c = 2 nm and n_c = 22.

The COB model only accounts for transitions where the potential barrier between the approaching HCI and the solid becomes sufficiently low to be passed classically by electrons from the Fermi edge. As these distances are typically large enough for tunneling to be extremely unlikely, this assumption has proven reasonable. Subsequent multiple electron capture results in the formation of a short-lived multiply exited quasi-neutral atom which carries a large part of its electrons in high-n levels while most inner shells remain unoccupied. This state has been termed “hollow atom” by Briand [40] to pictorially illustrate an electronic structure leading to the appearance of projectile-characteristic soft X-ray emission upon HCI surface impact. Such X-rays arise primarily in the late stage of the HA decay already inside the target bulk, whereas the largest part of the slow electrons will be emitted by autoionization (AI) still before the HA has touched the surface [23].

This extreme population inversion can last up to about a few tens of fs during the approach of a slow HCI towards the surface. Despite its short life-time the formation and decay of hollow atoms may be studied through their ejected electrons and characteristic soft X-rays, as well as their trajectories, energy loss and final charge state distribution of surface-scattered projectiles [23, 41-43]. Prior to their impact hollow atoms decay primarily via auto-ionization and other Auger-type processes by ejection of slow electrons. The thesis of Simon [1] gives a detailed overview of those processes. Subsequent re-neutralization and electron emission continue until the hollow atom collapses upon close contact with the surface. Until its full neutralization the projectile will be accelerated towards the surface by its rapidly decreasing image charge, which provides an additional “vertical kinetic energy”:

$$\Delta E_{im} \approx \frac{3}{4} \cdot q^{3/2} \cdot W \qquad (3)$$

For the above example of bare Ar^{18+} on aluminum, the image charge potential amounts to 80 eV.

The image charge acceleration has been experimentally confirmed using different techniques [44-47], in excellent agreement with COB model predictions [48]. One technique makes use of the emission of slow electrons. The corresponding electron yields increases with decreasing perpendicular impact energy. The energy gain by image charge acceleration E_{im}, however, sets a lower limit for the effective impact energy of the projectile and therefore the yield saturates below

certain nominal impact energies. Thus, the image charge acceleration can be deduced from an analysis of the velocity dependence of electron yields [46]. Alternatively, another method makes use of the fact that for grazing incidence of HCI on a flat mono-crystalline target surface the angle of the outgoing trajectory of the neutralized projectile can be steeper than the specular angle of the incoming ion trajectory due to image charge acceleration [45].

2.1.2 Trampoline Effect

For HCI impact on insulator surfaces instead of metals, several new aspects have to be considered (c.f. chapter 2.1). At distances larger than the critical value R_c for electron capture, the projectile will be accelerated by the self-image interaction (which can be significantly reduced as compared to an ideally conducting surface). As electron capture initially populates highly excited Rydberg states of the projectiles, a hollow ion will be transiently formed. The localization of valence electrons around atomic centers at the surface (e.g. F^- in LiF) and the lack of cylindrical symmetry of the electronic potential now significantly modify the electronic evolution in the projectile [49]. Electron capture will create holes in the electronic structure of the surface, which – unlike metals – may not be rapidly refilled. Hole formation reduces the capture rate for electrons unless the holes diffuse through the crystal.

The mobility of the holes in the crystal and the subsequent capture of more tightly bound electrons from the same ionic state will have a decisive influence on the number of emitted electrons [50]. If the supply for subsequent electron capture is diminished by these effects the projectile ion may even feel a local positive charge while still above the surface leading to a deceleration of the projectile. In fact, Briand et al. [39] have put forward the intriguing hypothesis that the repulsive interaction between the holes and the projectile when still (highly) ionized can become stronger than the attractive self-image force and eventually lead to backscattering of the projectiles from the surface without touching it (see Fig. 2.1-3). This “trampoline effect” has to be distinguished from the more conventional backscattering due to close binary collisions with surface atoms/ions [51] and deflection of the impinging ions due to macroscopic charge-up by previous projectiles.

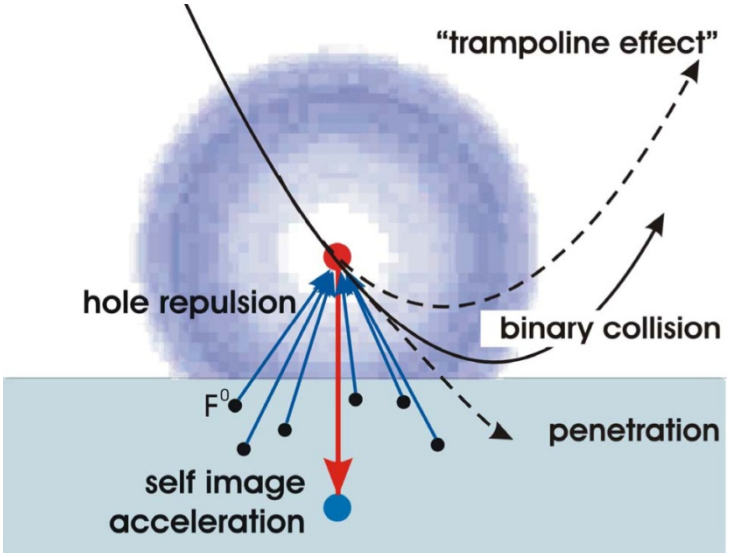

Fig. 2.1-3: Illustration of the trampoline effect postulated by Briand et al [39]. When the repulsive force between holes in the target material and the approaching ion becomes strong enough to overcome image charge acceleration, it may be reflected without hitting the surface [50].

2.1.3 Sources for Highly Charged Ions

Continuous development of ion source technology in the recent years made it possible to produce beams of slow ($v < v_{Bohr} = 2.19 \cdot 10^6$ ms^{-1}) highly charged ions (HCI) and use them for ion-surface interaction studies [38, 52-57]. Of the different types of ion sources available, the Electron Beam Ion Trap (EBIT [58]) was exclusively used to produce projectile ions for the present study, thus the discussion of ion sources is limited to this device.

An EBIT is a device to breed, store, investigate and also to extract highly charged ions (HCIs) [46, 52, 59-61]. Of the few devices that can produce HCI of the highest charge states, which are the subject of the present thesis, the EBIT is definitely the most cost efficient and widely used. They are used to investigate a wide variety of processes related to the physics of highly charged ions. Of fundamental importance are spectroscopic measurements of line radiation emitted from excited HCIs in order to test relativistic quantum mechanics, quantum electrodynamics (QED), electron correlation and nuclear physics (for recent work see e.g. [62-64]). More recently, ion beams extracted from an EBIT are utilized in a wide range of applications, from those associated with fusion plasma physics to those associated with nano-scale device fabrication [65, 66].

In an EBIT, the ions of interest are produced by bombardment with a mono-energetic electron beam. It is produced at a cathode and accelerated into the trap region, where a strong magnetic field compresses the electron beam to small diameters (usually less than 100 µm). This increases the current density and thus also the chance for successive ionization of the same target atom/ion. The compressed electron beam exerts a negative space charge, which, together with the axial magnetic field, traps the produced ions radially. A set of electrodes at the trap region, called drift tubes, provides the axial trap potential. During their confinement in the trap, the ions are brought consecutively to higher charge states by collisions with beam electrons (see e.g. [65-67] and refs. therein). HCI are thus produced in the trap region, where the electron beam energy defines the highest achievable charge state (it has to be larger than the ionization potential). The actual charge state distribution is governed by the mean trapping time of the ions. To minimize loss of HCI via charge exchange with neutral atoms, the residual gas pressure in the trap region is usually in the 10^{-10} mbar range or less. A beam of HCI can be extracted either continuously via thermal excitation by the beam until their energy is sufficiently high to escape the trap, or by repeated opening of the confining drift tube potential (pulsed extraction).

Although the two sources used for this study, namely the Heidelberg EBIT at the Max Planck Institute for Nuclear Physics and the Dresden EBIT at the Forschungzentrum Dresden/Rossendorf, both in Germany, are both EBITs and share the same basic principle, they differ considerably in their details. For this reason, both are discussed separately in the following.

2.1.3.1 The Heidelberg Electron Beam Ion Trap

The Heidelberg EBIT is an improved clone of the Super-EBIT built at the Lawrence Livermore National Laboratory (LLNL) in the United States. It is designed to achieve the highest possible charge states, which are bare ions of heavy elements (e.g. U^{92+}). A Pierce-type electron gun delivers up to 500 mA of electron current, which can by accelerated up to about 15 keV by biasing of the drift tube array. By separately applying high voltage of up to -120 kV to the electron gun, the necessary electron energy for the stripping of K-shell electrons of heavy elements can be achieved. The electron beam is compressed by an 8 T magnetic field provided by a pair of superconducting Helmholtz-coils

(see Fig. 2.1-4). The Heidelberg-EBIT uses a horizontal geometry for the electron beam, which, together with an improved thermal isolation of the cooled region decreased the consumption of liquid Helium by an order of magnitude to 0.2 l/h as compared to the original EBIT at LLNL. The electron beam is compressed to about 50 µm by the magnets, which amounts to a space charge of up to 500 V. The axial confinement via the drift tube potentials is typically about 300 V. Neutral atoms are injected into the trap region as a supersonic jet for gaseous sources, or via a Knudsen-cell sublimator for solids. The trap region acts like a cryo-pump due to the liquid Helium cooling of the surrounding magnets, keeping the residual gas pressure well below 10^{-10} mbar. On their way to the collector, which is on cathode potential, electrons are decelerated while ions are accelerated. Fast ions pass the collector and are focused electrostatically into the charge-state separating magnet of the beam line. Typical extracted HCI beams in leaky mode are at a few thousand particles per second (for a single charge state).

From the electron gun to the collector, the Heidelberg-EBIT is about 4 m long. Together with its power supplies and other electronics, it fills a small laboratory all by itself. Its main design goal was the achievement of high charge states, but so far no deceleration beam line has been built in the lab, so that the range of available kinetic energies per charge state is between 3 and 12 keV/q. For a more detailed review of the Heidelberg EBIT, refer to the diploma thesis of Simon [1].

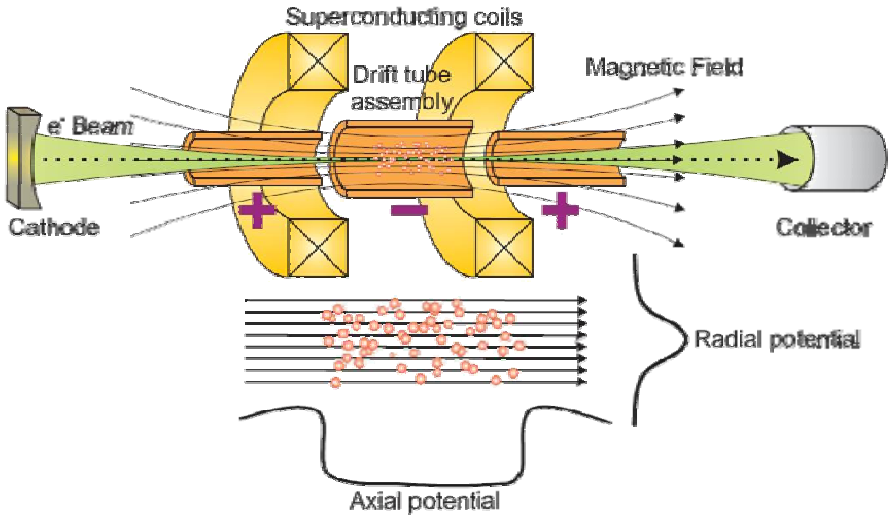

Fig. 2.1-4: Schematics of the Heidelberg EBIT [68]

2.1.3.2 The Dresden Electron Beam Ion Trap

Contrary to the source described in the previous sub-chapter, the Dresden EBIT is a compact device that was optimized for extraction of ions in moderate charge states. Its overall size is about 0.5 m (see Fig. 2.1-5). Its design parameters (and costs) are considerably lower than that of the Heidelberg EBIT, yet it provides high currents of ions in medium charge states (e.g. up to Xe^{40+}). The Dresden EBIT at FZD is built into a deceleration beamline, which allows the tuning of final kinetic energies per charge state from 10 eV/q up to 4.5 keV/q. Details of the source can be found elsewhere [69, 70].

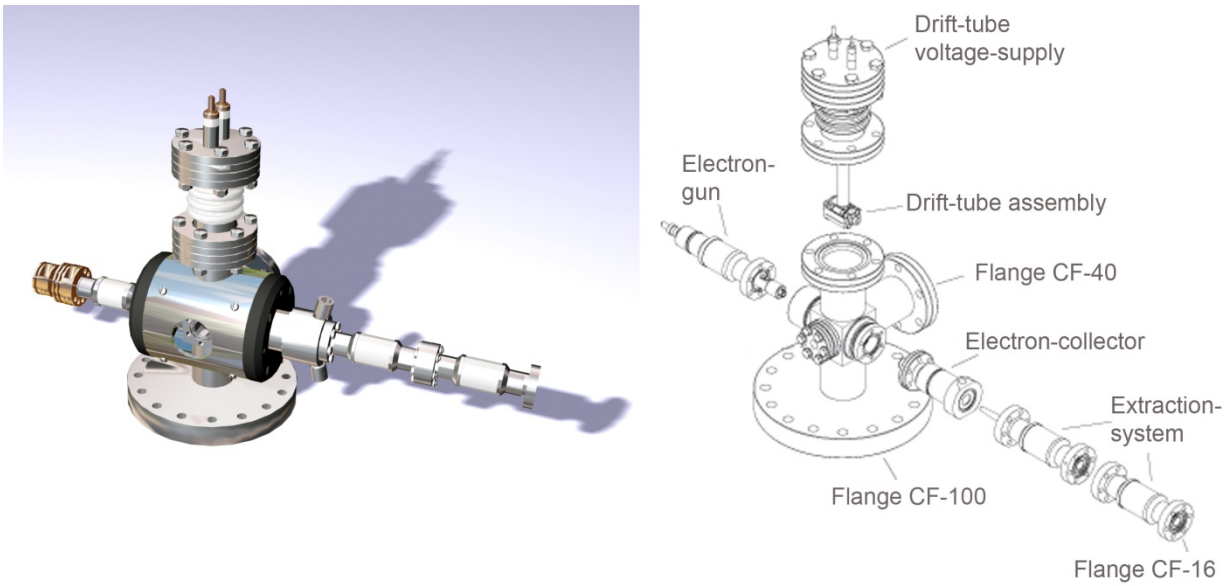

Fig. 2.1-5: Left: Dresden EBIT-II, Right explosion view of the Dresden EBIT-II. Note the small size of the ion source (The extraction system is built inside CF-16 vacuum components). Picture courtesy of R. Heller.

The following is a brief summary of the working parameters of the Dresden EBIT. For more details refer to the diploma thesis of Winklehner [3]

- *Cathode.* The cathode heating current is > 2A and produces an electron beam current of up to 75 mA.
- *Trap (drift tubes).* The drift tube region has a length of 18 mm. Typical trap potentials applied to the outer drift tubes are ~20 V.
- *Magnets.* The magnetic field compressing is formed by two Samarium-Cobalt ($SmCo_5$) permanent magnets, eliminating the need for liquid helium cooling. In the region of the axis of the drift tubes, they produce a magnetic field of ~0.25 T.
- *Electron beam.* The final kinetic electron energy is 2-28 keV. The electron-beam current-density is ~200 Acm^{-2}. The diameter of the electron beam is 100-200 µm.
- *Ion beam (leaky-mode).* Typical ion currents in the leaky mode are: 100 pA for Ar^{+}, 40 pA for Ar^{10+} and 0.5 pA for Ar^{16+} [71]. For the measurements with the present setup, a much lower current of 10-100 fA of $Xe^{10+...40+}$ ions was desired and realized.
- *Ion beam (pulsed mode).* In the pulsed mode, the trap is opened periodically for some milliseconds. Typical trap frequencies are in the range of 0.3 to 10Hz. Ion numbers are e.g. Ar^{18+}…8000 ions/pulse with a corresponding peak current of 16 nA or Xe^{44+}…5000 ions/pulse with a corresponding peak current of 10 nA [71].
- *Vacuum.* The vacuum in the chamber with an electron beam is > $2 \cdot 10^{-10}$ mbar. Working gas pressures are typically in the range of 10^{-10} to 10^{-8} mbar.

2.2 Nanostructuring of Surfaces

CaF_2 is used as an insulator in silicon microelectronic devices [17, 18] and can be epitaxially grown on semiconductor surfaces [19]. High resolution patterning of thin CaF_2 films on silicon is of interest for the creation of nanostructured templates for adlayer growth during fabrication of CaF_2/Si-based epitaxial insulator-semiconductor structures. It is a non-amorphizable alkali-earth-halide crystal. Single crystals of CaF_2 can be cleaved to produce surfaces of large atomically flat terraces separated mostly by monolayer steps. The cleaving procedure is comparably simple, and calls for a short application of mechanical stress to the crystal by means of a hammer and a sharp razor-blade.

Damage creation in ion-surface collisions is strongly correlated to ion-energy deposition in the solid and therefore depends on both the kinetic and the potential energies carried by the ions [20]. The kinetic energy loss of a projectile (stopping power) is usually subdivided into an ‘‘electronic’’ (inelastic) and a ‘‘nuclear’’ (elastic) part (see insert in Fig. 2.2-1). For slow singly charged or neutral atoms, nuclear stopping dominates the energy loss (case 2 in Fig. 2.2-1). This energy transfer to target cores leads to atomic displacements and lattice vibrations in the target (phonons) and can become sufficiently large to initiate a collision cascade where also the recoiling target atoms contribute to electronic excitation and displacement in the solid [19]. The low kinetic energy of the incident projectile limits its total path length and therefore the region where energy is deposited to a few monolayers close to the surface [72]. For swift ions or atoms (case 3 in Fig. 2.2-1) scattering from the target nuclei becomes negligible, but the now dominant electronic energy loss leads to a high ionization density around the (practically straight) ion tracks (see e.g. [73, 74] and references therein). In addition, inner shell ionization processes produce fast δ electrons which can considerably enlarge the region where electronic excitation/ionization of the target takes place. In contrast to this, slow highly charged ions (HCI, case 1 in Fig. 2.2-1) also mostly interact with the electronic sub-system of the target, by means of their potential energy, which can be similar to or even exceed the ions kinetic energy [11].

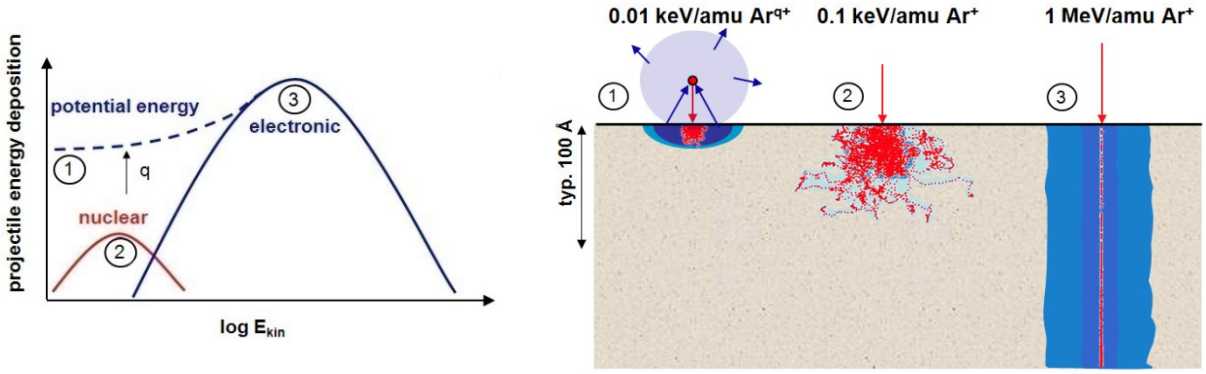

Fig. 2.2-1: Energy deposition during interaction with a solid surface (schematically, c.f. text) of (1) very slow highly charged ions, (2) slow single charged ions or neutral atoms, (3) swift ions or neutral atoms [75].

2.2.1 Swift Heavy Ion Irradiation

In recent years, great efforts have been made to investigate the surface damage induced by high energy ions (MeV to GeV impact energy region) in several ionic fluoride single crystals e.g. LiF, CaF_2, BaF_2, MgF_2 and LaF_3 [76-80]. While the long term goal of these studies was to reach a clearer understanding of the damage creation mechanisms, the short term goal aimed at obtaining information about the created surface features and their dependence on the ion-beam parameters and material properties. Atomic force microscopy (AFM) has been used as the primary tool to observe surface structures on insulating surfaces on a nanometer scale [81]. The AFM micrographs of the swift ion-irradiated single ionic fluoride crystals showed nanoscopic hillocks protruding from the surface. However, such hillocks are only found for projectile ions where the electronic energy loss (S_e) exceeds typically a threshold of 5 keV/nm [77, 79]. Above this threshold both the diameter and height of the hillocks increase with the electronic stopping power S_e [79], which is defined as the amount of energy transferred to the electronic sub-system of the target by the projectile per unit of path length (considering its dimension, it should actually be called stopping force) [11]. The nanostructures created by swift heavy ions are usually accompanied by damage created deep inside the bulk. This sets limits for using high-energy ions in nano-technological applications.

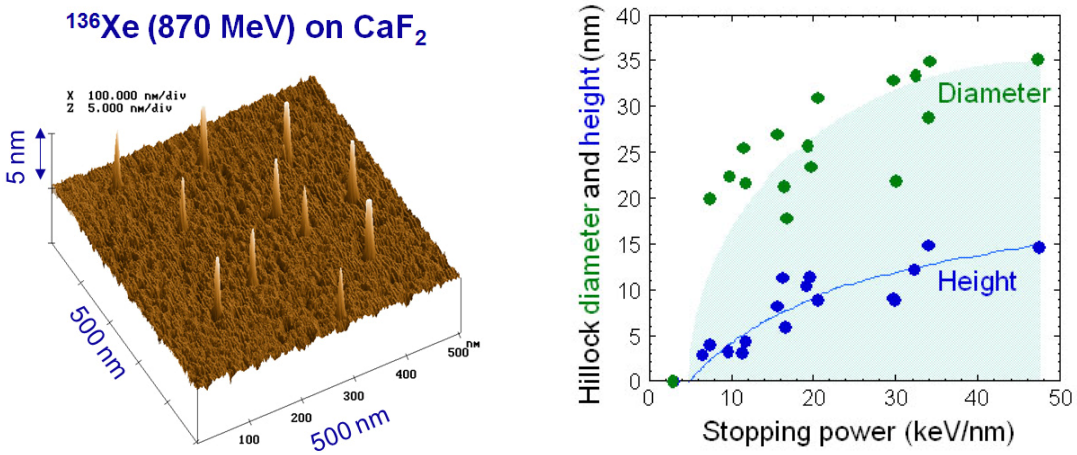

Fig. 2.2-2: AFM image of a CaF_2 surface irradiated by swift heavy ions (left) [78]. Height and diameter of the induced nanostructures as a function of the electronic stopping power of the projectiles (right) [78, 82]. Note the threshold at 5 keV/nm.

Impact of swift heavy ions is known to induce physical, chemical, and structural modifications not only on the surface but also in the bulk (see e.g. [83-85] and references therein) [10]. Individual projectiles form cylindrical tracks around their trajectory of a few nanometers in diameter. Depending on the solid, tracks consist of amorphized or defect-rich material. In non-amorphizable alkali and alkaline earth halides (e.g. LiF and CaF_2) the damage process is governed by exciton-mediated defects such as color centers and defect clusters [86, 87]. Above a critical value of dE/dx, damage produced in the core of the track leads to a macroscopic volume increase (swelling, [88, 89]), track etchability [86], and stress [90]. At the surface of ionic crystals, swift ions induce nanometric hillocks [78, 79] above a threshold value similar to that for swelling [88].

While there is no question that the intense electronic excitation of a confined volume around the ion trajectory due to the electronic stopping of the swift ions is the major cause for this modifications [20], the exact mechanism how this energy is transferred to the lattice is still under discussion and probably strongly depending on the type of material. Several simple mechanisms have

been proposed. In the Coulomb explosion model (e.g. [91]) the positively charged lattice atoms created by the slowing projectile via ionization processes, repel each other, thus leading to a shock wave. In the thermal spike model (e.g. [92]) the kinetic energy of the electrons is transferred to the lattice atoms efficiently enough to increase the lattice temperature locally above the melting temperature, followed by a rapid quenching. For ionic crystals like alkali halides (LiF) or fluorides (CaF_2) sub-lattice effects exist, in which the electronic excitation is mainly deposited in the anion sub-lattice, leading to specific point defects or even defect clusters (resulting from self trapped excitons, V_k centers etc.) which are connected to track formation, surface hillock production and increased sputtering yields [6, 26-28].

2.2.2 Slow Highly Charged Ion Irradiation

One major limitation for the application of swift heavy ions to three-dimensional structure formation is the radiation damage of deeper layers [4]. The desire to confine the energy deposition to the surface layer has stimulated the interest in slow (eV to keV) and highly charged ions. With increasing charge state these ions carry a large amount of potential energy (e.g. 14 keV for bare Ar^{18+}, 51 keV for Ne-like Xe^{44+}). The potential energy deposition and electron depletion induced by the neutralization sequence of slow highly charged ions (HCI) on insulator targets is expected to be confined to a nanometer sized volume close to the surface and to occur on a femtosecond time scale [23]. Intuitively, one expects the formation of nano-sized surface craters due to Coulomb explosion. In contrast to these expectations, the first experiments with 7 keV/q HCI (q denoting their incident charge state) on Muscovite mica showed nano-hillocks [93, 94] when the interaction zone was inspected by atomic force microscopy (AFM). For ion charge states below q = 30 no damage could be identified. Systematic experiments on Mica revealed that the observed structures do not represent topographic changes of the surface but rather changes in the surface friction leading to the observation of ”hillocks” and sometimes ”craters” depending on the scanning direction of the AFM [94]. Furthermore, the observed structures were not stable and disappeared after repeated scanning with AFM. The volume of the ”apparent” structures was found to be roughly proportional to the potential energy of the impinging ions [94-96] while only weakly dependent on the projectile kinetic energy [96]. Studies on other surfaces (such as HOPG) found similar results (for a recent review of this field see [6]). However, due to the high kinetic energy of the projectile ions (up to several hundred keV as a result of 5 – 10 kV acceleration voltage) kinetic effects (e.g. contributions from kinetic energy transfer to the target cores or electrons) could not be ruled out.

This chapter will review the current state of this rather new field of slow HCI-induced nanostructures. The circumstances and conditions under which nano-sized features on particular surfaces can be produced by impact of slow highly charged ions.

2.2.2.1 Mica

Muscovite mica ($KAl_3Si_3O_{10}(OH)_2$) is known as an easily cleavable layered compound providing very smooth and atomically flat surfaces. It was therefore among the first materials to be studied. Topographic changes due to irradiation of Mica with slow HCI have first been reported by the Livermore group [93, 94, 97]. Using atomic force microscopy (AFM) in air and irradiation by 7 keV/q Kr^{35+}, Xe^{44+}, U^{70+} and Th^{74+} ions they observed the formation of what they called "blister" - like defects protruding from the surface. From the area density of the observed blisters and the total number of ions used they concluded that each hillock is the result of a single ion impact. The volume of the blisters was found to be proportional to the charge state and roughly proportional to the potential

energy of the used ions [94]. No structures could be identified in the AFM images for the case of similar fast (300 keV) singly charged Xe^{+} impact on Mica (even for ion fluences 10 times that for the HCI case) [93]. These HCI on Mica measurements were later repeated by a Kansas State University - NIST Gaithersburg collaboration [95, 96] at constant kinetic energy (0.75 keV/amu) of the incident Xe^{q+} ions ($25 \leq q \leq 50$). These authors observed circular hillocks, whose volume increased linearly with the potential energy of the projectile ions (Fig. 2.2-3) [95], but showed no pronounced dependence on the ions kinetic energy [96]. For projectile ions below q = 30 no damage could be identified [6].

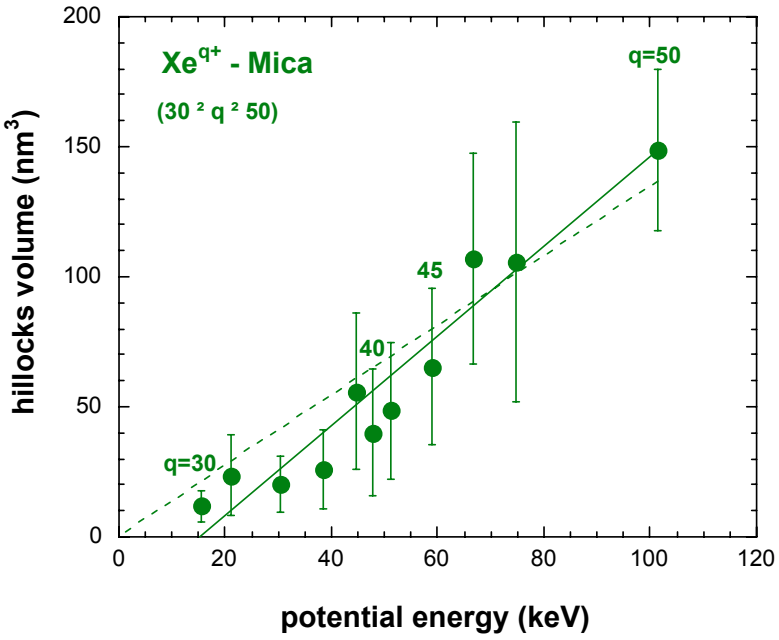

Fig. 2.2-3: Volume of hillocks produced on Mica due to impact of 100 keV Xe^{q+} ions ($30 \leq q \leq 50$) as measured by AFM (data taken from ref. [95]). Figure from [6].

2.2.2.2 Graphite

Scanning tunneling microscopy (STM) with atomic scale resolution has been applied to study surface defects in highly oriented pyrolytic graphite (HOPG) produced by impact of slow HCI. The TU Wien group [55] compared ultra-slow (150 eV) singly and multiply charged Ar ions (charge state up to 9+) studied in-situ (i.e. without breaking the UHV between irradiation and STM measurements). In all cases hillock - like surface defects protruding from the atomically flat surface were observed in the STM images (Fig. 2.2-4, left image). Their area density was in good agreement with the applied ion fluence, implying that about every single ion impact causes one protrusion. A $\sqrt{3}\times\sqrt{3}\ R\ 30°$ surface reconstruction, as characteristic for interstitial defects in HOPG, was observed in the vicinity of most defects (see Fig. 2.2-4) [55, 98]. As the most remarkable result they found that the measured size of the hillocks (mean diameter and height) increases with projectile charge state (Fig. 2.2-5) [55].

It is worthwhile noticing that hillocks of very similar size are also observed for irradiation of HOPG with swift heavy ions. Fig. 2.2-4 compares STM images of surface defects produced by the impact of a single 150 eV Ar^{9+} ion (potential energy of about 1 keV) on HOPG [55] with the case of 1.5 GeV Xe ions [99] which deposit a similar amount of electronic energy into the first atomic layer of HOPG.

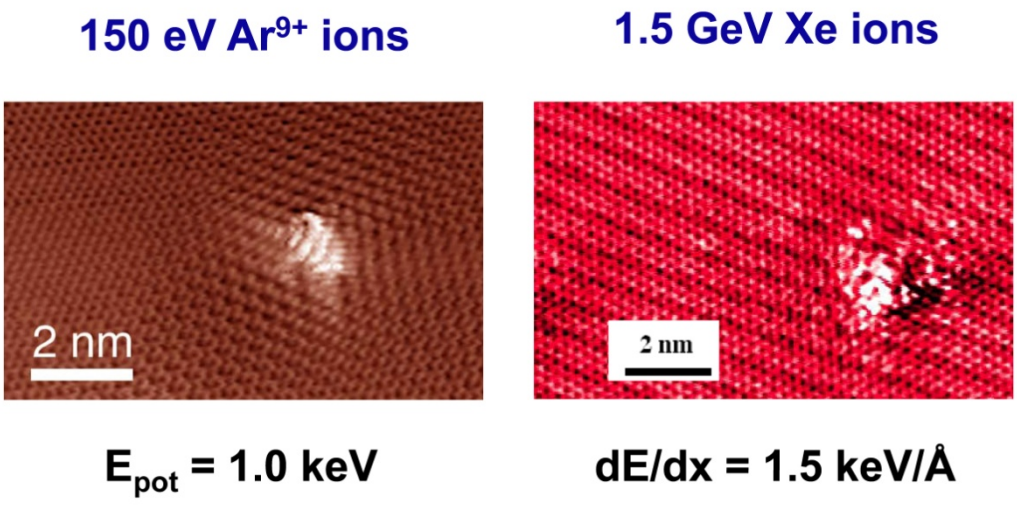

Fig. 2.2-4: Hillock-like surface defects produced by the impact of a single ion on HOPG as seen by STM with atomic resolution. Left image: for impact of a single Ar^{9+} ion with 150 eV kinetic energy [55]; right image: for impact of a single Xe ion with 1.47 GeV [99], (courtesy of C. Trautmann). Figure from [6].

An increase of hillock size on HOPG with the charge state of the impinging Ar^{q+} ($q \leq 8$) ions was also reported by Mochiji et al. [100] (Fig. 2.2-5). Since the protrusions were only visible in STM but not in AFM images, these authors concluded that the defects are of electronic rather than topographic nature.

Using Raman and tunneling spectroscopy Meguro et al. [101] showed that the impact of single Ar^{q+} ($q \leq 8$) ions and the subsequent treatment of the irradiated spot by electron injection (either from the STM tip or by laser irradiation) induces a local transition from sp^2 to sp^3 hybridization in HOPG, resulting in the formation of nano-scale diamond-like structures (nano-diamonds) at the impact region.

The measurements on HOPG could be extended to higher charge states using Xe^{q+} projectiles ($q= 23, 44$ [102], $q \leq 46$ [56, 57]). The results of all measurements on HOPG are summarized in Fig. 2.2-5, where the hillock diameter as measured in STM is plotted as a function of the projectiles potential energy.

Since the kinetic energy of the various projectile ions shown in Fig. 2.2-5 was generally different, it is important to note that a Japanese group could demonstrate that the kinetic energy of the ions, which was varied between 1 keV - 200 keV, has practically no influence on the hillock diameter or height [56]. Moreover, for Xe^{46+} projectiles the hillocks were not only visible in STM but also in the AFM image taken at the same impact sites [57]. The hillock diameters as observed with AFM were nearly equal, the heights slightly smaller to that observed with STM.

Compared to the case of Mica the hillocks observed on HOPG are much smaller in size. Although the potential energy has a strong influence on the feature size the formation of hillock-like defects does not seem to require a minimum potential energy, since these defects could even be observed for slow singly charged ion impact. However, a stronger increase of the hillock size above a certain potential energy (Fig. 2.2-5) could point to a different mechanism for hillock formation during the deposition of large amounts of potential energy [6].

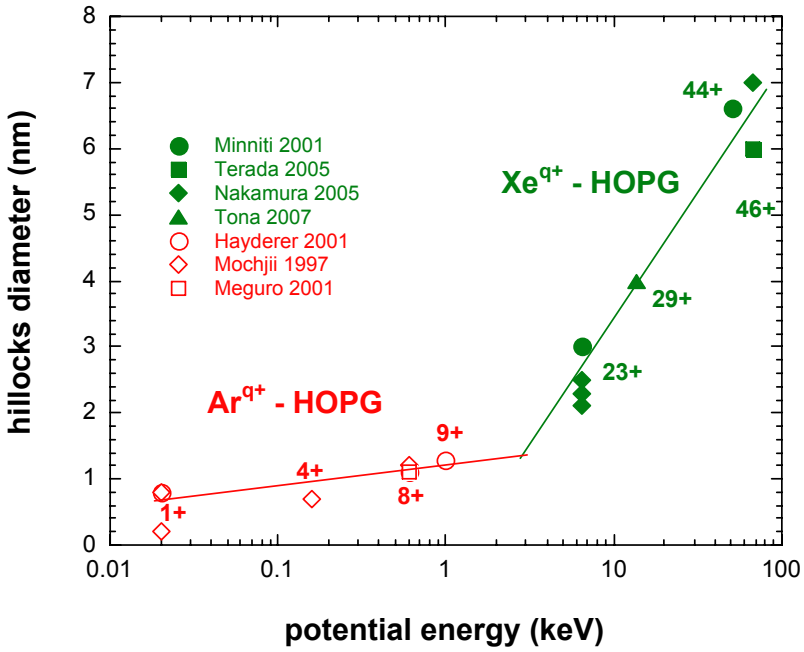

Fig. 2.2-5: Diameter of hillock-like nanostructures as produced on HOPG surfaces due to impact of single Ar^{q+} ($1 \le q \le 9$) and Xe^{q+} ions ($23 \le q \le 46$) and investigated by STM (data taken from refs. [55-57, 100-103]). Figure from [6].

2.2.2.3 Silicon

Using STM with atomic resolution Tona et al. [104-106] could recently observe radiation effects on a Si(111)-(7 x 7) after irradiation with slow HCI from the Tokyo EBIT. Bombardment of the in-situ prepared Si surface with I^{q+} projectiles in charge states q=30, 40 and 50 (impact energy 3 keV x q) yielded nanometer sized crater-like structures (typical diameters ranging from 1.5 - 3 nm) as visible on STM images taken in-situ (i.e. without breaking the UHV). In the atomically resolved STM images craters have brighter sites on the edges around the missing topmost layers. Depth-profiles of these craters showed that the depth of the crater reaches at least 0.35 nm for the case of an I^{50+} impact. The crater size rapidly increased with the projectiles potential energy [104]. First indications of a kind of potential energy threshold at around q=30 will have to be confirmed by more systematic studies that vary the HCI charge state in the future [6].

2.2.2.4 Titanium Oxide

The Tokyo group also irradiated TiO_2(110) surface by slow I^{51+} projectiles and could observe "caldera" like structures (i.e. craters with a protruding rim) with sizes larger than the craters observed on the Si(111) surface [103]. The caldera height (typ. 1 nm) was higher than the atomic step of the TiO_2(110)-(1x1) surface (typ. 0.3 nm) and the depth reached at least 1.5 nm. This implies that the same potential energy of a HCI projectile leads to larger nanostructures on a TiO_2 than on a Si(111) surface [103] [6].

2.3 Electron emission studies

2.3.1 Classification

Electron emission is generally divided into two different categories:

- kinetic emission (KE), c.f. [15] and references therein
- potential emission (PE), c.f. [25] and references therein

where the first is caused by the projectiles kinetic energy (defined by its velocity) and the second by the projectiles potential energy (defined by its charge state, c.f. chapter 2.1). In extreme cases, pure KE could be induced by neutral ground-state projectiles without any potential energy, whereas pure PE could be induced by charged projectiles with close to zero velocity. Although one advanced measurement schemes allow the determination of pure PE yields even at the presence of considerable KE contributions [107], generally the two contributions cannot be separated by simple electron yield measurements. Therefore one usually tries to measure in a regime where one of the two contributions is dominant. For PE measurements, this is achieved either by measuring at velocities smaller than the KE threshold (pure PE), or using ions of very high charge states, where the PE contribution can be orders of magnitude above the KE yield.

The existence of a projectile velocity threshold v_{th} for KE follows from energy conservation in the 2 body system of the heavy projectile and the light target electron at the Fermi edge, where the gain of the latter has to be sufficient to overcome the binding energy W_Φ.

$$v_{th} \approx \frac{1}{2} v_F \left(\sqrt{1 + \frac{W_\Phi}{E_F}} - 1 \right) \qquad (4)$$

where v_F is the Fermi velocity of target electrons and E_F the Fermi energy. KE originates solely from beneath the target surface, while PE occurs above the surface, at the time of impact as well as after the ion has penetrated the solid (see 2.3.1). For a detailed description of the relevant processes like Auto-ionization (AI), Auger Neutralization (AN) and Auger Deexcitation (AD) refer to the review of Aumayr [25] or the original work of Hagstrum [21, 22].

2.3.2 Total Electron Yields from Conducting Targets

Potential electron emission from conducting targets under HCI impact has been studied extensively over the past 20 years and is now very well understood in the frame of the classical-over-the-barrier (COB) model [35] (c.f. chapter 2.1.1). While a linear dependence of the yield on the potential energy of the ion was observed for very low charge states, this relationship breaks down for medium and high charge states. Fig. 2.3-1 shows total electron yields measured with a “fountain type” electron statistics setup (see chapter 4.1.1 and 4.1.3.2) [46]. For the lower of the two velocities used during these measurements, no significant KE contribution is to be expected and the total yields represent pure PE.

The velocity dependence of electron yields for impact of HCI on metals has the following qualitative behavior: Starting at the lowest possible velocities (defined by the self-image charge acceleration of the projectile towards the surface) the yield drops with increasing velocities as the time for hollow atom formation and decay in front of the surface decreases. A minimum is reached

upon which the total yield increases again due to the onset of KE (c.f. Fig. 2.3-2). In the exclusive PE regime, electron yields γ_{PE} follow the predictions by COB theory [36, 108] for increasing velocity *v*:

$$\gamma_{PE}(v) \approx \frac{c}{\sqrt{v}} + \gamma_{\infty} \qquad (5)$$

where c and γ_{∞} have to be determined empirically for a given collision system and the velocity *v* has to include image charge attraction.

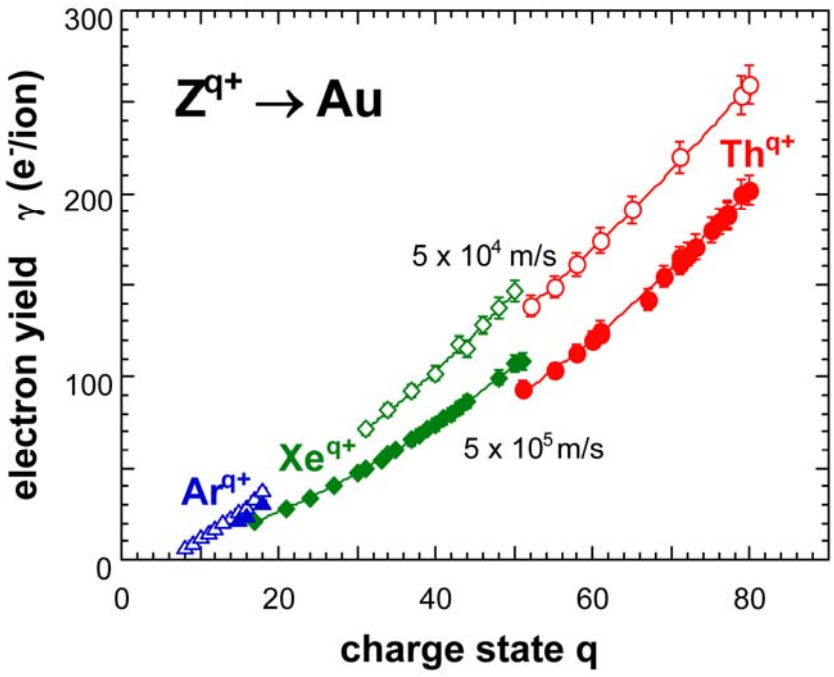

Fig. 2.3-1: Total electron yields measured at two different impact velocities for Ar^{q+}, Xe^{q+} and Th^{q+} impact on a clean gold surface under normal incidence [46].

Measurements of HCI impact on gold surfaces under grazing incidence by Lemell et al [109] have shown that at least for medium charge states, the time for hollow atom decay above the surface is the determining factor for electron emission. As the interaction time is defined by the normal component of the impact velocity $v_{\perp}$, the angular dependence of PE yields for metals can be written as

$$\gamma_{PE}(\theta, v_{\perp}) \approx \frac{c'}{\sqrt{v_{\perp}}} + \gamma_{\infty} = \frac{c'}{\sqrt{v_0 \cos(\theta)}} + \gamma_{\infty} \qquad (6)$$

where θ is the impact angle with respect to the surface normal and v_0 is the projectile velocity.

The total image charge acceleration depends on the hollow atom formation and decay dynamics, as the charge of the projectile changes before the final impact. Aumayr et al. [46] have measured the magnitude of image charge acceleration for impact of up to Th^{79+} ions on gold and found good agreement with the so-called “staircase approximation” of the COB model [110].

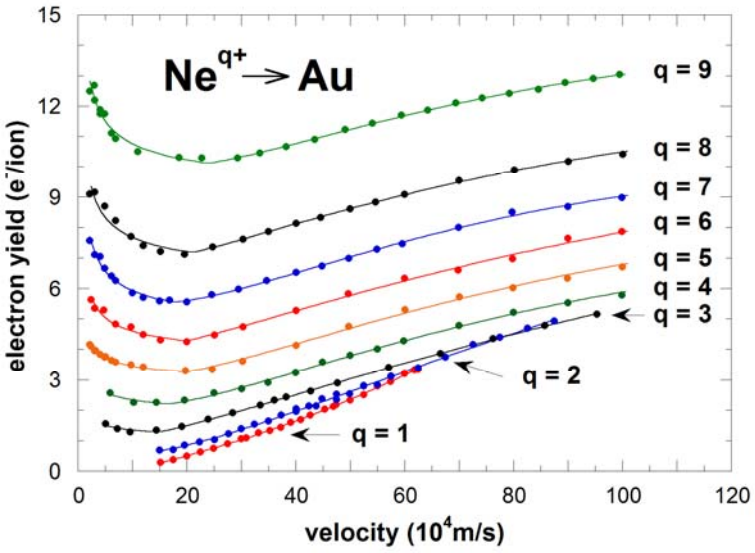

Fig. 2.3-2: Velocity dependence of total electron yields (γ) for impact of different charge states of neon ions on a gold surface [111].

2.3.3 Total Electron Yields from Insulating Targets

Projectile image charge acceleration has so far only been observed for a few insulator surfaces as for example LiF, and moderate charge states of projectile ions under grazing angles of incidence (see [112] and references therein). Surprisingly, the measured energy gain due to image charge acceleration yields similar results as for the same HCI on a conducting surface. This has been explained by two counteracting effects. Firstly, the reduced image potential due to the lower permittivity of the material leads to less acceleration. Secondly, the closer projectile – surface distance for electron capture from an insulator surface due to the larger binding energy of the valence electrons leads to an increased time of acceleration until the projectile becomes neutralized.

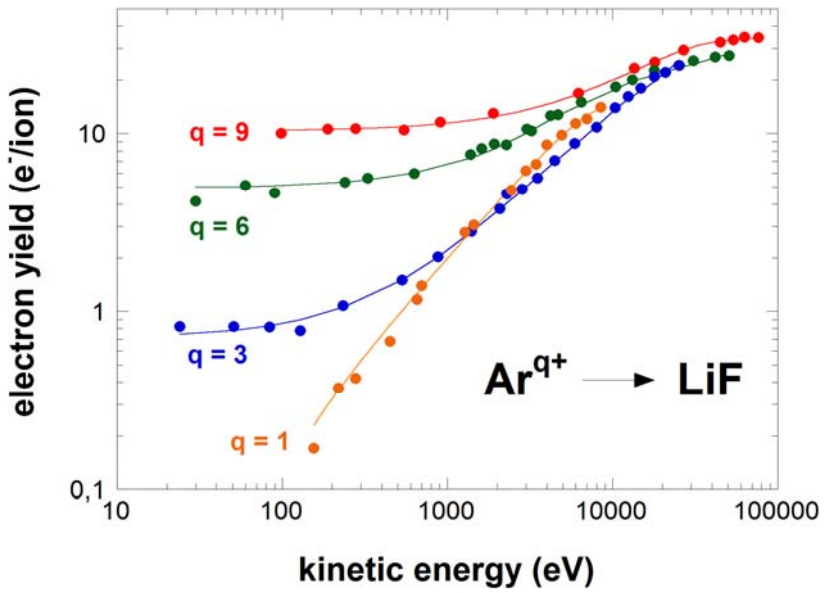

Fig. 2.3-3: Velocity dependence of total electron yields for Ar^{q+} impact on an insulating LiF surface [113].

The theoretical description is complicated by the fact that in an ionic crystal such as LiF, valence band electrons are localized at the halogen site and are subject to additional (long and short range) potentials (e.g. Madelung potential) [50, 114-116]. In principle, electron capture has to be described as a local process with the history of the holes left behind to be taken into account.

Experimental evidence on HCI-induced electron emission from insulator surfaces is scarce and limited to low projectile charge states. A comparison between potential electron yields for normal impact of Ar^{q+} ($q \leq 9$) and N^{q+} ($q \leq 6$) on LiF and gold (see Fig. 2.3-3) [113, 117] showed that, in general, fewer electrons are emitted from the insulator, but this effect is masked by a strong contribution from kinetically emitted electrons. In the presence of energetic K-shell holes in the projectile, however, electron yields from both materials were comparable, which was explained by the relatively more efficient secondary electron production by fast electrons in LiF, and the high inelastic mean free paths of slow electrons which allows secondary electrons to escape the solid.

Stöckl et al. [107] have used a time-of-flight setup to measure the projectile's energy loss in coincidence with emitted electrons for grazing impact of Ar^{q+} ($q \leq 8$) on LiF (see Fig. 2.3-4). By extrapolation of the measured electron yields to zero energy loss of the projectile, pure PE yields were obtained. For all charge states under investigation, the measured PE yields were in good agreement with the theoretical upper limit posed by the work function W_φ of the material:

$$\gamma_{PE,\max} = \frac{E_{pot}}{2W_\Phi} \qquad (7)$$

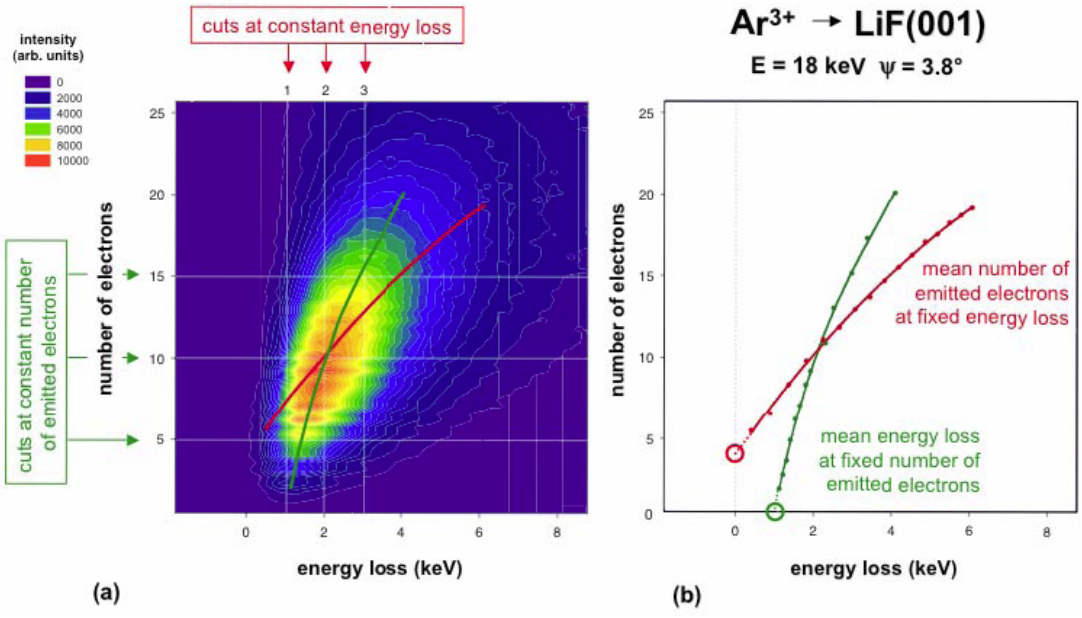

Fig. 2.3-4: a) The number of emitted electrons was measured in coincidence with the projectile's energy loss for grazing incidence of 18 keV Ar3+ on LiF. b) An extrapolation of the mean number of electrons emitted at fixed energy loss to zero energy loss allows the determination of pure potential electron emission yields. From [107].

Any Auger-type electron emission process consumes at least twice the work function from the available potential energy E_{pot} of the projectile [21, 22, 25]. Thus it was observed that the limitations of an insulator (charge mobility, band gap) pose no barrier for the provision of sufficient electrons to

complete the hollow atom decay in front of the surface. Due to the grazing trajectory of the projectile, the approaching HCI continuously moves into pristine areas of the target surface and leaves positive holes behind.

In recent years, insulating capillaries have surprised the scientific community, because it was observed that they are able to guide ion beams even when the tilt angle of the capillary with respect to the ion beam direction is larger than the aspect ratio of the capillaries [8, 118]. Tapered glass capillaries have even been shown to enhance the current density of the incident HCI beam [119]. A self-organized charge-patch inside the capillaries was found to be responsible for the capillary guiding effect [120]. Emission of electrons upon impact of the HCI on the insulator surface has so far not been included in the theoretical models of this effect. Although electron emission in the capillary cannot change the overall charge balance of the impact, the electrons can effectively transport holes around the surface of the insulator material. Precise determination of electron yields for HCI impact on insulators over a wide velocity regime would therefore also help the scientific advancement in this field.

"If you do things right, people won't be sure you've done anything at all"
the universe to Bender, in futurama

3 Nanostructuring of Calcium Fluoride

3.1 Experimental Methods

3.1.1 Irradiation target holder

In the course of this study, a special target holder for irradiation of different targets with slow HCI has been constructed to meet the following criteria

- an option to carry multiple targets in order to minimize unnecessary pumping time between irradiations
- the ability to carry targets of different sizes and shapes
- means to locate the position of the beam relative to the targets and to allow precise positioning of small beams on the target
- the possibility to carry the target holder in an exsiccator (vacuum vessel) without damaging the targets

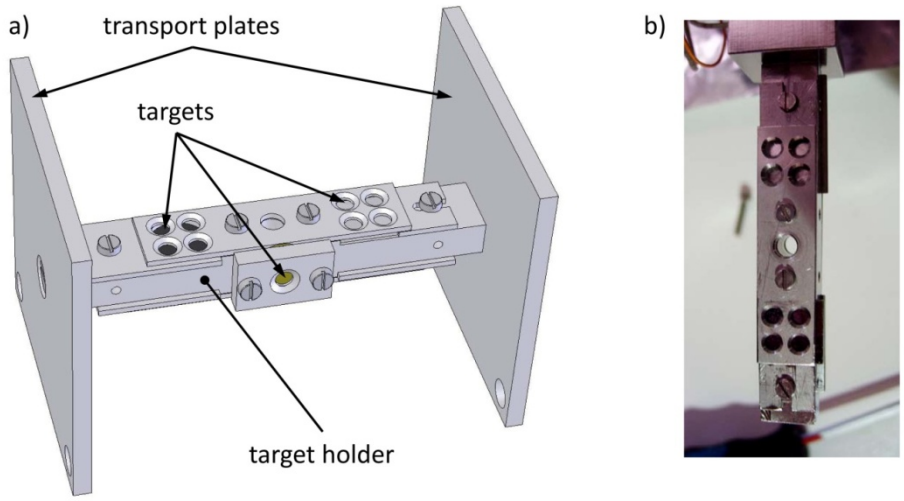

Fig 3.1-1: View of the irradiation target holder. a) With mounted transport plates, it can be transported without damage to the targets. b) Photo of target holder with four targets mounted for irradiation (two in the back).

The HEBIT facility delivers a beam of only 2mm diameter to our experimental chamber. This size was originally chosen for electron emission experiments, where small beams are necessary. For target irradiation under normal incidence, the small beam size creates a problem, however: after the irradiation, which does not leave any visible trace on the targets, it can be very hard to find the relatively small irradiation spot on the target using the AFM. For this reason a precise positioning of

the beam onto the targets was crucial. The FZD facility delivers a much broader beam of approximately 5 mm diameter, which can also be scanned over the target surface. That way, a precise positioning system was not needed and the targets were simply transferred via commercially available Omicron target plates. As the FZD facility also hosts its own AFM instrument, transportation to and from Vienna were not necessary. Targets irradiated in Heidelberg had to be brought back to Vienna for examination and the damage to the targets during the transportation was a problem to be solved.

Fig 3.1-1 a) shows the final design of the irradiation target holder for the HEBIT facility with the transport plates attached. With those plates attached, the target holder can be fixed into an exsiccator of 10cm diameter, which is still a suitable size for transportation by mail service. Fig 3.1-1 b) shows the target holder after removal of the transport plates with mounted targets, ready for irradiation. A central hole through the target holder, as can be seen in Fig 3.1-2, allows a first position calibration of the beam with respect to the target holder. For this means, the target is moved with respect to the beam, while an electron detector (see chapter 4.1.1) measures the number of emitted electrons per ion. If the beam hits the steel mask of the target holder, the measured yield is much higher than when the beam passes through the hole and hits the downstream chamber walls. With the position calibrated this way, the target holder can be moved to one of the irradiation spots, which are represented by the 3 mm diameter holes in the irradiation mask. Since the mask has a drastically different electron yield than the targets (which may also charge up if they are insulators, see chapter 4.2.2), the same positioning technique can be used once more to make sure the beam hits the very center of the hole in the mask. Since the position of the mask with respect to the targets is well known, the irradiation spot can be found easily afterwards.

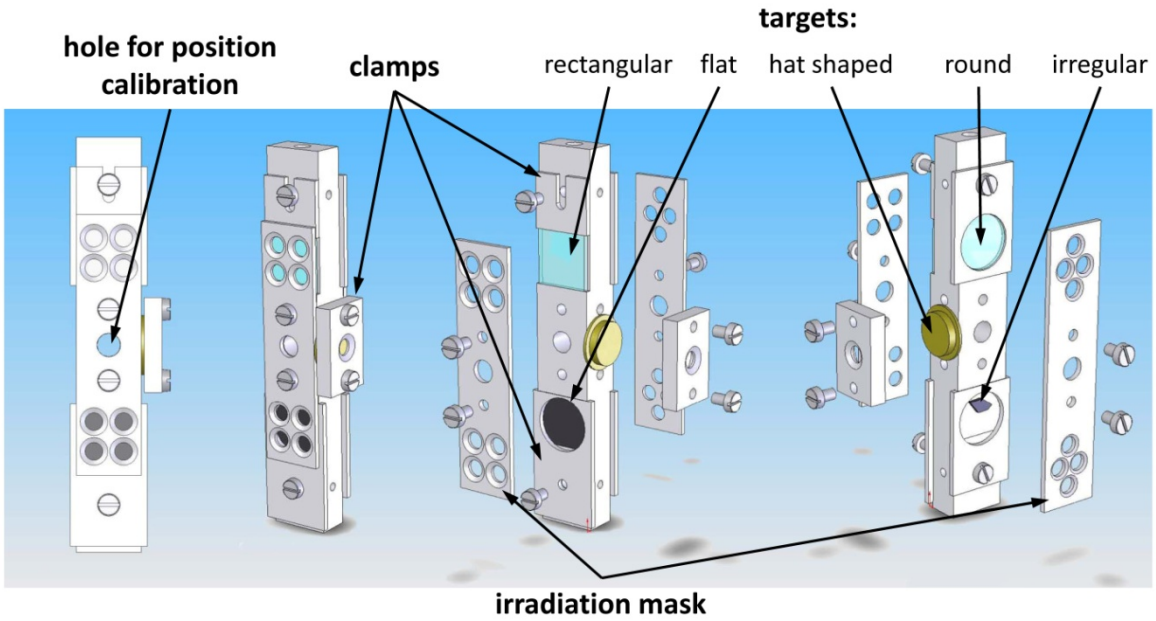

Fig 3.1-2: Explosion view of the irradiation target holder. Multiple targets in different shapes can be mounted for irradiation under normal incidence. The irradiation masks allow a precise definition of the irradiation spot on the target.

The targets themselves are fixed to the holder with clamps. Different clamps can house targets of almost any shape, provided they are small enough to fit onto the holder. Rectangular targets like

the CaF_2 crystals frequently used during this work can be fixed from one side with a slider clamp. Flat targets can be pressed down on the target holder with a suitable clamp, while round targets are held in place by a very similar device. Irregularly shaped targets like shards of yttrium iron garnet can be glued onto a thin foil of stainless steel and are then mounted just like flat targets. The irradiation masks have holes that either fit a 1 cm^2 square target and allow four spots to be made on a single target (left in Fig 3.1-2, or 3 holes that fit a 1 cm diameter round target. Hat shaped targets like commercially available gold single crystals can be mounted to the side of the target holder by a suitable clamp. A hole in the center of the clamp then represents the irradiation mask.

After a few irradiations, it was observed that an undesirably high amount of dirt is found on insulating targets. This was attributed to a charge patch that builds on the surface during irradiation and attracts dust from the air when the vacuum is broken. To counter these effects, a new target holder was designed (see Fig. 3.1-3) with a central cavity that can house a heating coil. This way, targets can be heated to moderate temperatures during irradiation. It is known from swift heavy ion irradiation that heating of CaF_2 to 60° C does not influence the formation of nanostructures, while electron emission experiments have shown that this temperature is sufficient to counter significant charge-up of the sample (c.f. chapter 4.2.2). The improved target holder with heating coils has been designed in the very last months of this work, and has successfully tested in an experiment not encompassed by this work.

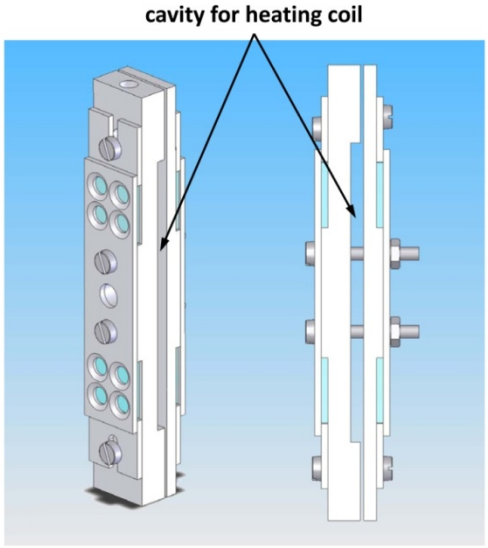

Fig. 3.1-3: New design for an irradiation target holder with a cavity for a heating coil. Moderate heating during irradiation is supposed to counter charge-up and undesirable attraction of dust after irradiation.

3.1.2 Atomic Force Microscopy

The invention of the scanning tunneling microscope (STM) in 1981 by Binning and Rohrer [121] was the first example of a scanning probe microscope (SPM). It can scan surfaces with atomic resolution by measuring the tunneling current between an ideally mono-atomic tip and the sample surface while rastering the tip across the sample via a piezoelectric mechanism (see Fig. 3.1-4). Many different manifestations of SPMs have joined the STM since then, which all share the same general concept.

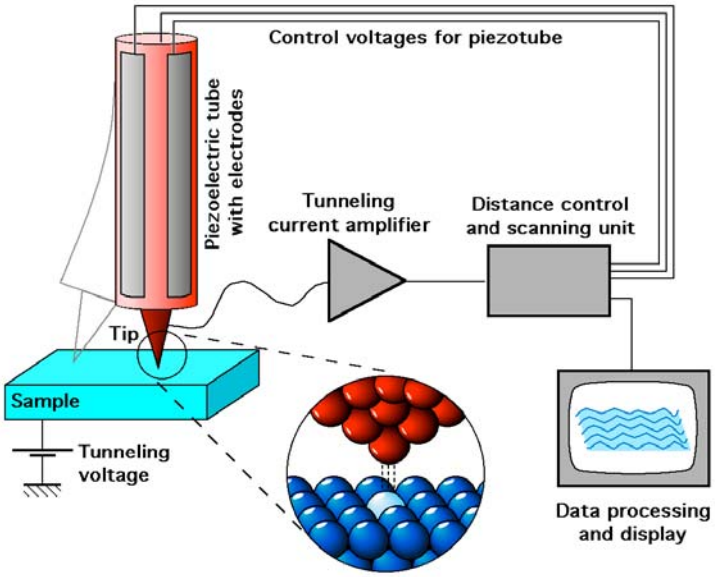

Fig. 3.1-4: Principle of a scanning tunneling microscope (STM) (courtesy of Michael Schmid, Vienna UT).

A sharp probe is raster-scanned across a sample by means of piezoelectric translators, while a certain signal (current, force, torsion, electromagnetic radiation, etc.) is recorded by the probe for every single image point [122]. The most important aspect of this concept is to use this local signal to monitor the probe-sample separation and hence obtain topographical information in real space. In order to accomplish this task, one can identify the following components as common features of SPMs [122]:

- Sharp probe.
- Piezoelectric translator to move the probe relative to the sample.
- Detection system for the signal delivered by the probe.
- Feedback system to keep the signal constant by height readjustment of the probe.
- Imaging system to convert the single data points to an image.

In the following, only the Atomic Force Microscope (AFM) will be discussed, as only this instrument was used for the present study. The basic idea of the AFM is the measurement and interpretation of the ultra-small forces (< 1 nN) which occur between the AFM tip and the sample surface at very small distances or in contact [81]. A cantilever with a sharp AFM tip is scanned over the sample. A laser beam is aligned and with the back of the cantilever, reflected from it and subsequently measured by a position sensitive four-quadrant photodiode. Changes in the bending of the cantilever (due to topography of the sample surface) are thus detected (see Fig. 3.1-5). The piezoelectric positioning system can then adjust the position of the cantilever to maintain a constant bending of the cantilever and thereby also constant loading force (contact mode).

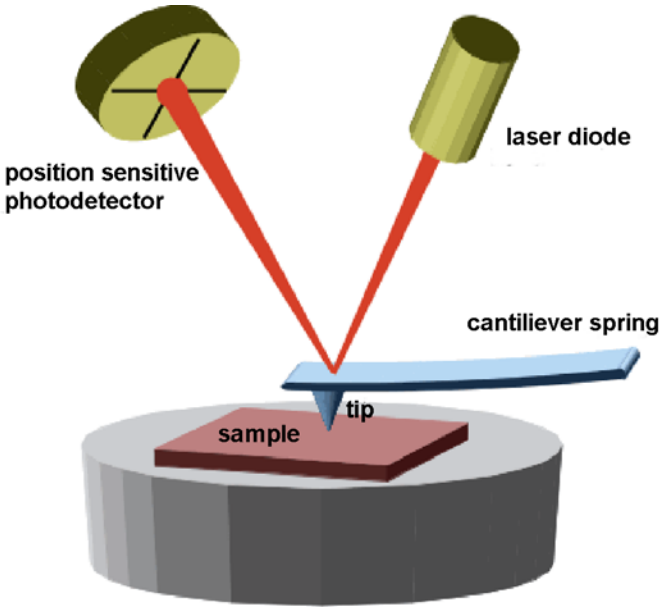

Fig. 3.1-5: Basic principle of an atomic force microscope: A sharp tip on a flexible cantilever is scanned over the sample surface. The laser beam reflected from the top of the cantilever is measured on a position sensitive photo-detector. Image courtesy of Greifswald University.

In contact mode, which was exclusively used for this study, the tip scans the sample in close contact with the surface. The repulsive force on the tip-atoms is caused by electronic orbital overlap with the surface atoms. The cantilever is pushed against the sample surface with a mean value of 10^{-9} N with a piezoelectric positioning element. During the scanning process, the deflection of the cantilever is permanently probed and compared in a DC feedback amplifier to a preset value of deflection (setpoint). The higher the chosen value of the setpoint, the stronger the tip pushes into the surface. Therefore one practically starts with small deflections and increases the setpoint slowly. If the measured deflection is different from the desired value, the feedback amplifier applies a voltage to the piezo to raise or lower the sample relative to the cantilever in order to restore the preset value of deflection. The voltage applied to the piezo is directly correlated to the piezo movement and therefore to the height of features on the sample surface. It is displayed as a function of the lateral position of the sample. Excessive imaging forces applied by the probe to the sample cause the most distinct problems in contact mode AFM. The effects can be reduced by minimizing imaging force of the probe on the sample, but there are practical limits to the magnitude of the force that can be controlled in ambient environment: Under ambient conditions, sample surfaces are contaminated by water molecules. When the probe makes contact with this layer, a meniscus forms and the cantilever is pulled toward the sample surface by surface tension. During this study, using CaF_2 as samples, the measurements were often performed in this attractive regime of the force curve. After the first contact of the tip and the sample, the cantilever is pulled back slightly so that it bends towards the surface. Then the tip is scanned over the sample to obtain the topographic images. It has to be mentioned here that the correct choice of cantilever (force constant), loading force and scanning frequency depends strongly on the type of sample material. The settings used throughout this study were found empirically with the ambient AFM at the Institut für Allgemeine Physik in Vienna [2].

The instrument used for the present study is an MFP-3D scanning force microscope (Asylum Research, Santa Barbara, US) operated under ambient conditions. Ambient AFMs as opposed to

ultra-high-vacuum (UHV) instruments have the benefit of fast sample change and positioning. The system used for this study is equipped with closed-loop nano-positioning system sensors for the correction of piezo hysteresis and creep. Furthermore it allows for simultaneous AFM and optical measurements of transparent and opaque samples due to top-view optics and an inverted microscope base. All measurements have been performed in contact mode at constant loading force of less than 10 nN, using non-conductive Si_3N_4 sensors (Veeco Instruments, France) with cantilevers of force constants of about 0.1 N/m.

3.2 Results and Discussion

3.2.1 Hillocks

This chapter presents first results on the generation of surface nanostructures by slow HCI on cleaved CaF_2 (111) surfaces. The CaF_2 single crystals were irradiated with slow (v < 1 a.u.) Xe^{44+} HCI from the Heidelberg-EBIT. Like for other ionic fluoride single crystals, ion-induced surface structures in CaF_2 are known to be stable in atmospheric conditions at room temperature. After irradiation the crystals were investigated by atomic force microscopy (AFM, c.f. previous chapter). Topographic images reveal the generation of nanometric hillocks protruding from the surface. The number of hillocks per unit area is in agreement with the applied ion fluence. A discussion of the role of the potential energy as well as a comparison with observations for swift heavy ion irradiations of CaF_2 single crystals are presented [11].

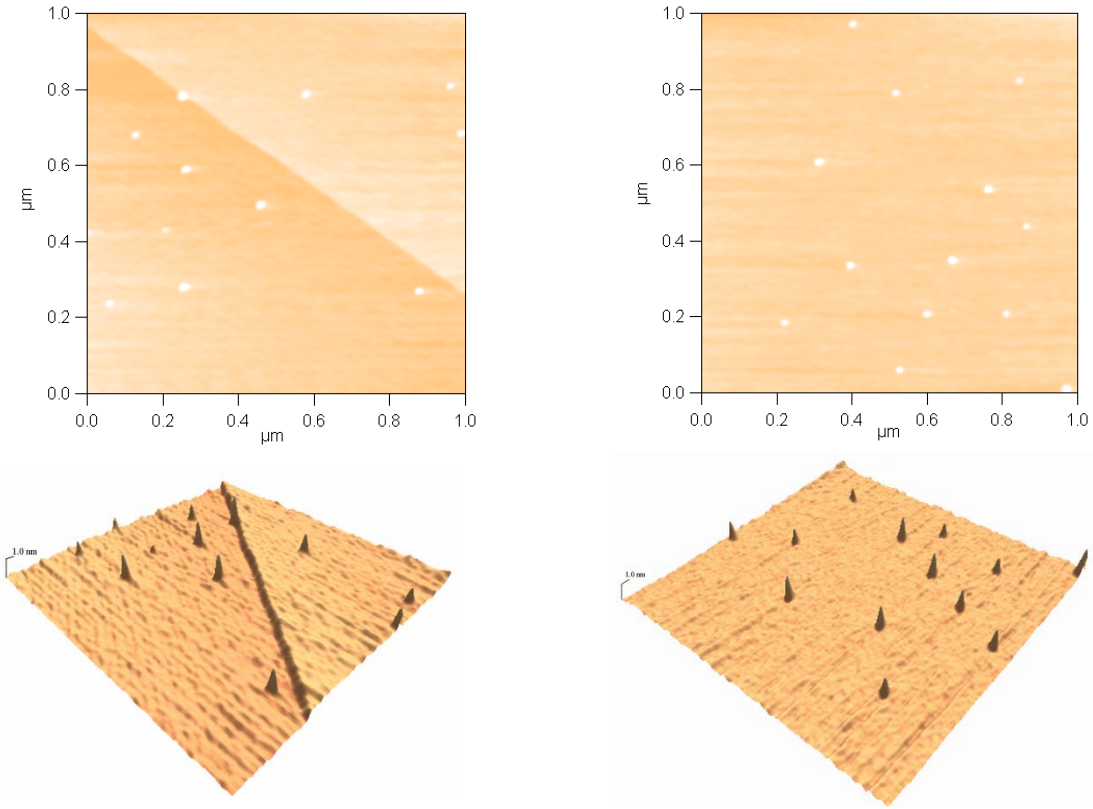

Fig. 3.2-1: Topographic AFM images of a CaF_2 single crystal irradiated with Xe^{44+} (E_k = 2.2 keV/amu - left) and Xe^{44+} (E_k = 3.3 keV/amu - right) ions [11].

The experiments were performed on CaF_2(111) surfaces freshly cleaved in air. Cleavage is known to result in a fluorine-terminated surface. Contact mode ambient atomic force microscopy (AFM) on this surface has been performed and revealed large atomically flat terraces with occasional cleavage steps separating individual terraces. Several freshly cleaved samples were mounted on a special target holder and transferred into the vacuum chamber which was evacuated to a base pressure in the 10^{-10} mbar range. The CaF_2 (111) single crystal targets were then irradiated at room temperature with $^{129}Xe^{44+}$ ions from the Heidelberg-EBIT [67] using two different ion impact energies (2.2 and 3.3 keV/amu). Typical ion fluxes of 10^4 ions/s (measured via electron emission statistics detection [13, 123], see chapter 4.1.1) and an irradiation time of several hours resulted in a total ion fluence of $2 \cdot 10^9$ ions/cm^2.

Fig. 3.2-1 shows examples of typical AFM topographic images of CaF_2(111) after irradiation with Xe^{44+} ions of 2.2 keV/amu and 3.3 keV/amu impact energy per atomic mass unit, respectively. Hillock-like nanostructures protruding from the surface are observed despite the fact that the electronic energy loss of the projectile ions in CaF_2 is well below the kinetic threshold for hillock production of 5 keV/nm (see Table 3.2-1) known from swift heavy ion irradiation (see chapter 2.2.1). The AFM images were evaluated with respect to hillock height and width distributions (see Fig. 3.2-2) as well as hillock number. The number of hillocks per unit area was found to be in good agreement with the applied ion fluence. This means that basically each observed hillock results from an individual ion impact. The shape of the hillocks is almost circular. Due to the low surface roughness of the non-irradiated samples, the dimensional analysis was easy to perform. The diameter of the hillocks is defined by two opposite points marking the intersections of a vertical line profile through the hillock maximum with the undisturbed CaF_2 surface [79]. A slight change of the set point (loading force) did not lead to an observable change of the measured features. A possible systematic error of the order of few nanometers for the hillock diameter is caused by the finite tip curvature radius. In contrast to the diameter, the height should not be affected by the finite AFM tip radius but mainly by the roughness of the sample. The mean hillock diameter and height were determined by fitting a Gaussian function to the hillock frequency-versus-diameter /- height histograms (see Fig. 3.2-2).

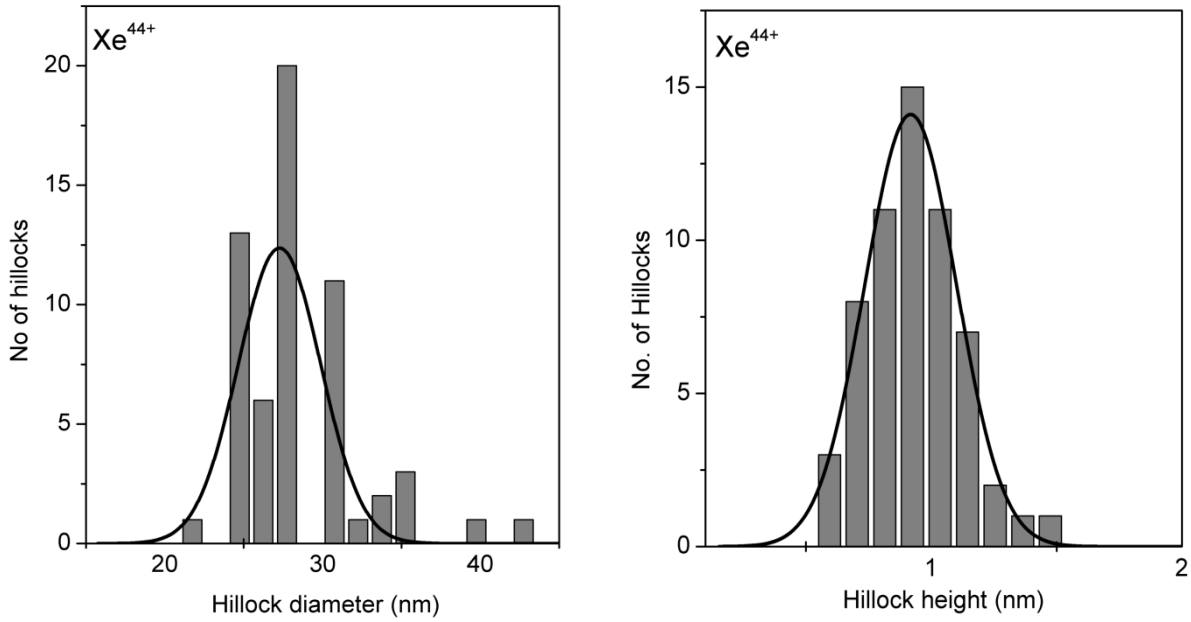

Fig. 3.2-2: Frequency distribution of hillock diameter (left) and hillock height (right) for CaF_2 single crystal irradiated with Xe^{44+} (E_k = 3.3 keV/amu) ions. The mean values are obtained by fitting a Gaussian curve to the data [11].

In Table 3.2-1, the ion-irradiation parameters (some of them estimated by using TRIM [72]) as well as the measured mean hillock diameters and height values are given. No significant difference in hillock size was found for the two different Xe^{44+} impact energies of 2.2 and 3.3 keV/amu. This independence on impact energy together with the fact that the experiments have been conducted for S_e values well below the kinetic threshold for hillock production leads to the early conclusion that the potential energy stored in Xe^{44+} ions (i.e. the sum of ionization potentials) of about 51 keV, and not the kinetic energy, is responsible for the hillock production.

Table 3.2-1: Ion-beam parameters and measured hillocks sizes

	Slow Xe^{44+}	Slow Xe^{44+}	Swift Xe [77]
Kinetic energy (keV/amu)	2.2	3.3	6400
Ion range (nm) [72]	84	117	46000
Electronic energy loss (keV/nm) [72]	1.09	1.31	19.5
Nuclear energy loss (keV/nm) [72]	2.85	2.56	0.02
Mean hillock diameter (nm)	28.1 ± 0.4	28.3 ± 0.5	23.5 ± 0.4
Mean hillock height (nm)	0.9 ± 0.1	0.9 ± 0.1	3.8 ± 0.2

Table 3.2-1 also compares the results of the present measurements to the hillock dimensions observed for swift Xe ion impact from [77]. The mean diameter of the hillocks in case of low energy Xe^{44+} bombardment is comparable to (even slightly larger than) the diameters observed after irradiation with Xe ions of more than 800 MeV kinetic energy, while the hillock height is about a factor of 4 smaller. The similarity between the two cases is probably a result of the fact that both swift heavy ions and slow HCI initially transfer their energy to the electronic system of the target, leading to a region of strong electronic excitation (see Fig. 2.2-10).

This early results therefore showed for the first time that nano-sized hillocks on a CaF_2 (111) surface can be produced by impact of slow HCI, but also demonstrate the relevance of the potential energy of the projectiles for creation of these nanostructure.

3.2.2 Potential Energy Threshold

After the first finding of hillocks on CaF_2 irradiated by slow HCI, a systematic variation of projectile charge states was conducted. Moderately slow ($v_p \approx 0.3$ a.u.) Ar^{q+} and Xe^{q+} highly charged ions with charge states between q = 11 and 48 were used for target irradiation. Atomic force microscopy of the irradiated CaF_2 crystals revealed a surprisingly sharp and well-defined threshold for hillock formation in the potential energy carried into the collision. Estimates of the energy density deposited suggested that the threshold is linked to a solid-liquid phase transition ("melting") on the nano-scale. With increasing potential energy, both the basal diameter and the height of the hillocks increase [10].

3.2.2.1 Experimental Evidence

The experiments were again performed on air-cleaved CaF_2(111) surfaces, which are known to show a fluorine-terminated surface. The irradiation was performed at the Heidelberg electron beam ion trap [67] using $^{40}Ar^{q+}$ (q = 11, 12, 14, 16, 17, and 18) as well as $^{129}Xe^{q+}$ (q = 22, 26, 28, 30, 33, 36, 40, 44, 46, and 48) projectiles during several runs. The extraction voltage was 10 kV (for Xe^{44+} also 6.4 kV) equivalent to a kinetic energy of 10 keV (6.4 keV) per charge state q. This resulted in a projected range between 90 and 140 nm in CaF_2, assuming that stopping power and range are unaffected by the high charge state (see below) [72]. The beam flux varied between 10^3 and several 10^4 ions/s, and was measured via electron emission statistics (see chapter 4.1.1) with close to 100% detection efficiency [13, 23]. After exposure to fluences up to $(0.5 - 5) \times 10^9$ ions/cm^2, the surfaces of the crystals were inspected in ambient air by contact-mode AFM.

Fig. 3.2-3 shows examples of AFM topographic images of CaF_2(111) after irradiation with Xe^{28+} (2.2 keV/amu), Xe^{30+} (2.3 keV/amu), Xe^{40+}(3.1 keV/amu), and Xe^{46+} (3.6 keV/amu) ions. Hillock-like nanostructures protruding from the surface are observed for highly charged Xe^{q+} ($q \geq 30$) and fully stripped Ar^{18+} ions whereas targets irradiated with Xe^{q+} ($q \leq 28$) and Ar^{q+} ($q \leq 17$) projectiles did not exhibit any hillocks. The sharp transition between q = 17 and 18 of argon cannot be associated with irradiation parameters in an obvious way. As reported in the previous chapter, results from irradiation with 6.4 keV/q (2.2 keV/amu) Xe^{44+} differ by less than 5% from the data of 10 keV/q (i.e. 3.4 keV/amu) Xe^{44+} ions. It appears that the kinetic energy plays no decisive role for the size of the observed nanostructures.

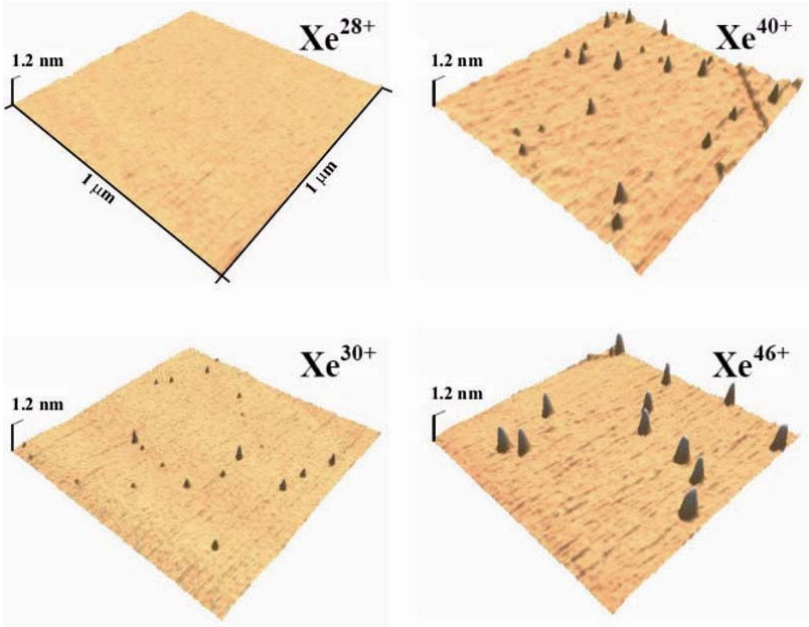

Fig. 3.2-3: Topographic contact-mode AFM images of a CaF_2(111) surface irradiated by 10 keV/q Xe^{q+} ions of charge state q = 28, 30, 40, 46. In each frame an area of 1µm ×1µm is displayed. Hillock-like nanostructures protruding from the surface are only observed for Xe projectiles with charge state q ≥ 30. Above this threshold, the height and diameter of the hillocks increase with ion charge state [10].

The AFM images were evaluated with respect to number density, height and width distributions of the hillocks. The number of the hillocks per unit area was found to be in good agreement with the applied ion fluence, i.e., above the threshold, a large majority of projectiles (70% - 100%) produces an individual hillock. Their height ranges between 0.5 and 1 nm and their diameter between ≈ 20 and 60 nm. Due to the finite curvature radius of the AFM tip (nominally 4-5 nm), the diameter (but not the height) of the hillocks is subject to a systematic error. The protrusions are rather flat with a diameter to height ratio between 40 and 60. In contrast to hillocks induced by swift heavy ions [78], only a weak correlation between the diameter and height value of a given hillock is observed. Furthermore, the size data were found to be strongly dependent on the potential energy which the projectile carries into the HCI-surface collision (see Fig. 3.2-4).

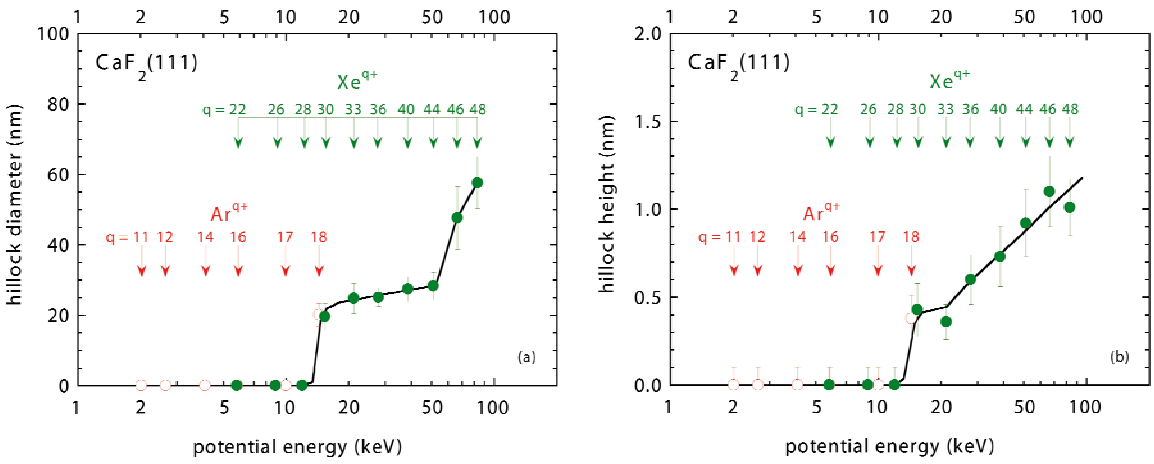

Fig. 3.2-4: Mean diameter (left) and height (right) of hillock-like nanostructures as a function of the potential energy of Ar^{q+} (open symbols) and Xe^{q+} (full symbols) projectiles. Hillocks are found only above a potential energy threshold of about 14 keV. The error bars correspond to the standard deviation of the diameter and height distributions; the solid lines are drawn to guide the eye [10].

The potential (i.e. internal) energy E_{pot} of HCI is equal to the total ionization energy required for producing the high charge state from its neutral ground state. E_{pot} is known to have a strong influence on surface interaction processes such as electron emission, sputtering, and secondary ion emission [23]. For both Xe and Ar ions a remarkably well-defined sharp threshold in potential energy (between $E_{pot} \approx 12$ keV for Xe^{28+} and $E_{pot} \approx 14.4$ keV for Ar^{18+}) for hillock formation emerges. Above this threshold, an increase of the potential energy leads to an increase of both the basal diameter and the height of the hillocks. Another steep increase of the mean hillock diameter potentially indicating a second threshold is found between Xe^{44+} and Xe^{46+} (left of Fig. 3.2-4).

3.2.2.2 Discussion

A convenient starting point for an analysis of the observed hillock formation is the interaction of the HCI above the surface involving a series of complex processes on different time and energy scales. When the ion approaches the surface, neutralization starts by electron transfer from the target into highly excited states of the projectile [35, 114, 124]. Deexcitation of the projectile proceeds via Auger-type processes producing primarily low energy electrons. Only for very highly charged heavy ions with open K and L shells electron energies up to several keV can be expected. For these states, however, radiative decay becomes important as a competing deexcitation mechanism with fluorescence yields of typically ≈ 12% [125]. An increasing amount of potential energy is therefore dissipated by X-ray emission. The critical distance R_c from the surface for electron transfer to the HCI can be estimated as [126]

$$R_c \approx \frac{\sqrt{2q\varepsilon(8i+\varepsilon-1)}}{(\varepsilon+1)W} \qquad (8)$$

where i is the amount of charge left behind (for the first electron capture i = 1), and W and ε are the work function and the dielectric constant of the material, respectively. For CaF_2 and i=1, $R_c \approx 0.16 \cdot \sqrt{q}$ nm applies, which sets an upper limit for the time available for the above-surface neutralization sequence. As an example, for an ion of q = 40, R_c is about 1 nm and the neutralization time is of the order of 1 fs. As the projectile velocity is also proportional to $\sqrt{q}$ in the present

experiment, the above-surface interaction time is the same for all projectiles with equal acceleration voltage. The transfer of electrons to the projectile leaves unbalanced holes in the surface which store part of the potential energy of the HCI. A number of unbalanced holes is created in the solid that diffuse only slowly into the material (hole velocity in the valence band derived from tight-binding calculations is smaller than 0.33 nm/fs [127]). Furthermore, two holes (F^0 atoms) in adjacent sites recombine to volatile fluorine gas molecules leaving behind a Ca-enriched metallic surface. Upon impact of the projectile the target is structurally weakened and features fluorine depleted, defect-enriched areas.

For an analysis and interpretation of this data, aspects of the inelastic thermal spike model developed for swift ions [128] were adapted. The underlying assumption is that the initial deposition of projectile energy involves the electronic subsystem of the target and proceeds on a (sub-) femtosecond scale while the energy transfer to the lattice and the concomitant lattice deformation and defect production occurs on a (sub-) picosecond scale. The present case of slow HCI differs, however, substantially in two aspects. The primary energy distribution of "hot" electrons results from a relaxation process of a hollow atom rather than from a Bethe-Born type ionization spectrum. A significant fraction of the potential energy is emitted by energetic (≈ keV) inner-shell Auger electrons. Moreover, slow HCI deposit their potential energy in a shallow surface region, whereas swift ions deposit kinetic energy along the full length of their trajectory within a cylindrical volume.

The following is an estimation of the amount of energy and the target volume in which HCI deposit their potential energy. From calorimetric measurements [129] it is known that only part of the potential energy is transferred to the target. Let us suppose that this fraction is around 50% with an uncertainty of 20%. The excited target electrons spread their energy within ≈ 100 fs by diffusion into a hemispherical volume around the impact site with a radius large compared to the source volume determined by the hollow-atom relaxation ($R_c \approx 1$ nm). In turn, the diffusing hot electron distribution transfers energy to the lattice by inelastic electron-phonon scattering with a characteristic time constant τ_e of a few hundred fs. Phonon-mediated energy transport leads to further spread and thermalization.

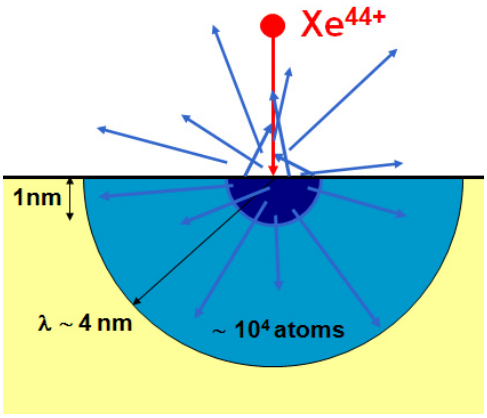

Fig. 3.2-5: The approaching highly charged ion leads to the emission of a number of electrons into vacuum as well as into the solid. Although the neutralization of the projectile in the solid is finished within the first nanometer of the surface, the inelastic mean free path of the electrons of 4nm leads to the heating of a hemisphere containing about 10^4 atoms.

Assuming, for simplicity, the same overall thermal diffusion length $\lambda_D \approx 4$ nm as observed for swift ions in CaF_2 [128], the fraction of internal energy E_D is deposited in a hemisphere of radius λ_D comprising about $N \approx 8.5 \cdot 10^3$ atoms (see Fig. 3.2-5). If the energy deposition per atom, E_D/N, within this locally heated volume exceeds the melting energy of $E_M = 0.55$ eV/atom [130] a solid-liquid phase transition is expected. Likewise, for $E_D/N > E_S = 1.55$ eV/atom [130], sublimation should set in. In order to have these energies available at the impact site, the HCI needs a potential energy above $E_{th,M} = 14$ keV and $E_{th,S} = 40$ keV, respectively. Such a crude estimate carries a large error bar of about ±50% due to the uncertainty in the effective λ_D and the fraction of deposited energy. The estimates are remarkably close to the observed threshold for hillock formation ($E_{th,M}$) and for the second drastic, almost step-like size increase ($E_{th,S}$) (see Fig. 3.2-6).

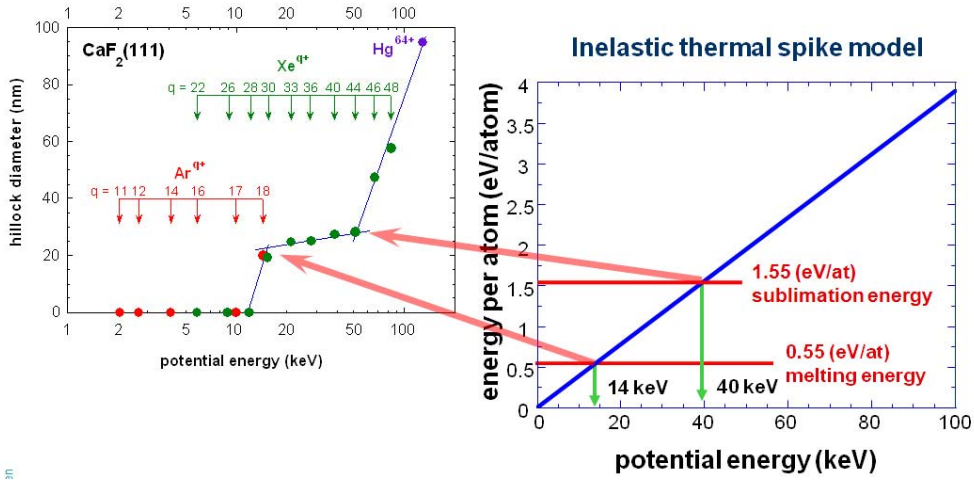

Fig. 3.2-6: Within the inelastic thermal spike model, the thresholds in the hillock size vs. potential energy of the projectile curve are explained as phase transitions in the target material.

Taking into account all the experimental data gained in the present experiments, the following scenario emerges: hillock formation is the result of local melting and swelling when the energy deposition by HCI near the surface exceeds the melting energy $E_M = 0.55$ eV/atom. If the energy deposition exceeds the critical value for sublimation $E_S = 1.55$ eV/atom, evaporation should lead to the formation of blisters of enhanced size. Moreover, one should expect the transition from blister to crater formation when the evaporation is further enhanced. This scenario, however, suggests that crater formation should be more likely for even higher q and at near-grazing impact angles when the energy deposition concentrates near the topmost atomic layer, and direct evaporation into vacuum becomes possible.

In conclusion, the bombardment of a CaF_2 surface with moderately slow ($v_p = 0.3$ a.u.) highly charged Ar and Xe ions produces hillock-like surface nanostructures. The formation of these protrusions requires a critical potential energy of 14 keV (Ar^{18+} and Xe^{30+}). A second threshold characterized by a steep increase of hillock diameter appears at 50 keV (Xe^{44+}). In analogy to hillock formation by swift heavy ions, the two thresholds are associated with phase transitions of melting and sublimation caused by the deposition of the potential energy within the electronic subsystem.

3.2.3 Dependence on the Ion's Impact Velocity

This chapter presents experiments with *very slow* (down to $v_p \approx 0.03$ a.u. or 30 eV/amu) highly charged ions (HCI) creating hillock-like topographic nanostructures on the surface of CaF_2 single crystals which are stable in air and non erasable by AFM scanning. As seen with moderately slow projectile (c.f. the previous chapter) a strong dependence of the formation of hillocks on the potential energy rather than on the kinetic energy is found, exhibiting a sharp and well-defined threshold of potential energy required for the onset of nano-hillock formation. Simulations of the dissipation of potential energy into the target material on the basis of an extended classical over-the-barrier model have been performed to facilitate the interpretation of the experimental findings [4].

3.2.3.1 Experimental Evidence

The experimental conditions were very similar to the experiments described in the previous chapters, but the irradiation of CaF_2 samples took place at the ion beam center of Forschungszentrum Dresden-Rossendorf (FZD). Isotope-pure $^{129}Xe^{q+}$ ions (q = 24 - 36) were extracted from a (commercially available) Dresden EBIT II source [69] (see chapter 2.1.3.2) and decelerated by a two-stage deceleration system to the desired final impact energy before impinging onto the single crystal CaF_2 surface under normal angle of incidence. Deceleration to a final potential difference between source and target down to 150 V resulted in the lowest impact energies of 150 eV/q (150 eV per projectile charge state), i.e. an impact energy of only 28 – 42 eV per atomic mass unit. The time-averaged beam flux varied between 10^4 and 10^6 ions/s. After exposure to fluences of about 10^{10} ions/cm^2 the crystal was transferred to an UHV-AFM/STM (Omicron) and inspected by contact-mode AFM.

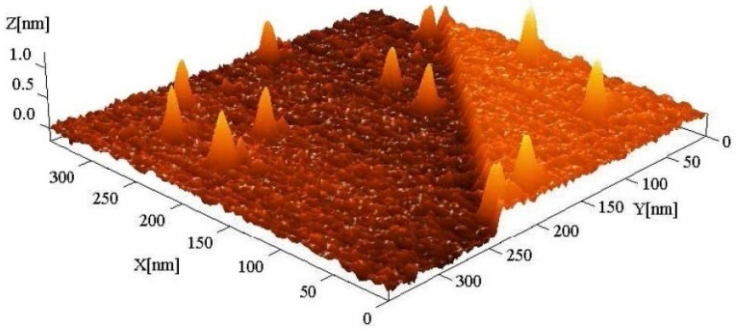

Fig. 3.2-7: Topographic contact mode AFM image of a CaF_2(111) surface irradiated by 66 keV Xe^{33+} ions showing hillock-like nanostructures protruding from the surface [4].

A typical AFM topographic image of a CaF_2(111) surface (Fig. 3.2-7) after irradiation with 66 keV Xe^{33+} ions (≈ 500 eV/amu) displays hillock-like nanostructures protruding from the surface. The AFM images were evaluated in terms of their areal density, height, and width distributions of the hillocks. The hillocks in Fig. 3.2-7 are typically 20 nm in diameter and 0.8 nm in height. Due to the finite radius of curvature of the AFM tip (nominally 7 – 10 nm), the diameter of the hillocks is subject to a systematic error [78]. Measurements of heights of structures, however, are known to be reasonably accurate. From the number of hillocks per unit area and the applied ion fluence, we determine that a vast majority of projectiles (about 80% $\pm$ 10%) produces one hillock each.

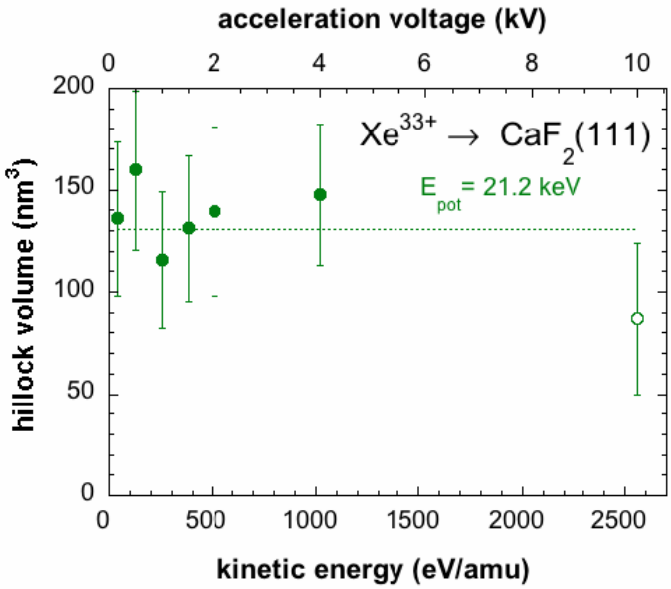

Fig. 3.2-8: Mean volume of hillock-like nanostructures on CaF_2 produced by the impact of Xe^{33+} projectile ions as a function of their kinetic energy. Full symbols: results from the Dresden EBIT [4], open symbol: results from the Heidelberg EBIT [10].

To demonstrate that the hillocks are solely due to the deposition of potential rather than kinetic energy (in the form of nuclear or electronic stopping) of the projectiles, the Xe^{33+} ions were decelerated to final impact energies as low as 38 eV/amu (150 eV/q). Fig. 3.2-8 shows the measured mean volume of the hillock-like nanostructures on CaF_2 produced by the impact of Xe^{33+} projectile ions as a function of their kinetic energy together with results for much more energetic (10 keV/q) Xe^{33+} ions [10] from the previous chapter. Despite the reduction of the kinetic energy by almost two orders of magnitude the measured hillock volume is essentially unaffected and stays almost constant. The data even indicate a slight increase with decreasing kinetic energy, a trend that was also found for other charge states (c.f. Fig. 3.2-9).

Hillock volume in this respect is defined as the volume of a spherical cap with the diameter and height as measured by AFM. The volume of a sphere cap is known to be

$$V = \frac{h^2\pi}{3}(3R - h) = \frac{h\pi}{3}(3Rh - h^2) \qquad (9)$$

where R is the radius of the sphere and h is the height of the cap. Since the diameter d of the cap basis is measured by AFM, and not the radius R of the sphere, one can use Pythagoras to evaluate:

$$R^2 = \frac{d^2}{4} + (R - h)^2 \Leftrightarrow 2Rh = \frac{d^2}{4} + h^2 \qquad (10)$$

Substituting the term $R \cdot h$ in formula (9) by using formula (10) finally yields the hillock volume as a function of hillock height h and hillock diameter d:

$$V = \frac{h\pi}{6}\left(\frac{3d^2}{4} + h^2\right) \qquad (11)$$

In order to explore the dependence on the potential energy of the projectiles Xe^{q+} ions were employed with charge states ranging from q = 24 to q = 36, while leaving the potential difference

between ion source and target surface at a constant value of 150 V. The hillock volume was found to be strongly dependent on the potential energy of the projectiles (Fig. 3.2-9). A well-defined sharp threshold in potential energy (between 10.4 keV for Xe^{27+} and 12.0 keV for Xe^{28+}) for hillock formation emerges. Above this threshold, an increase of the potential energy leads to a strong increase of hillock volume. The hillock volume seems to increase slightly for decreasing kinetic energy and the threshold shifts by about 2 keV. Repeated measurements confirmed that hillocks are produced by slow (150 eV/q) Xe^{28+} but not by fast (10 keV/q) Xe^{28+} projectiles. While above the threshold the hillock volume increases linearly with potential energy the shape of the hillocks does not depend on beam parameters, also the base diameter shows only a small dependence on the potential energy of the projectile.

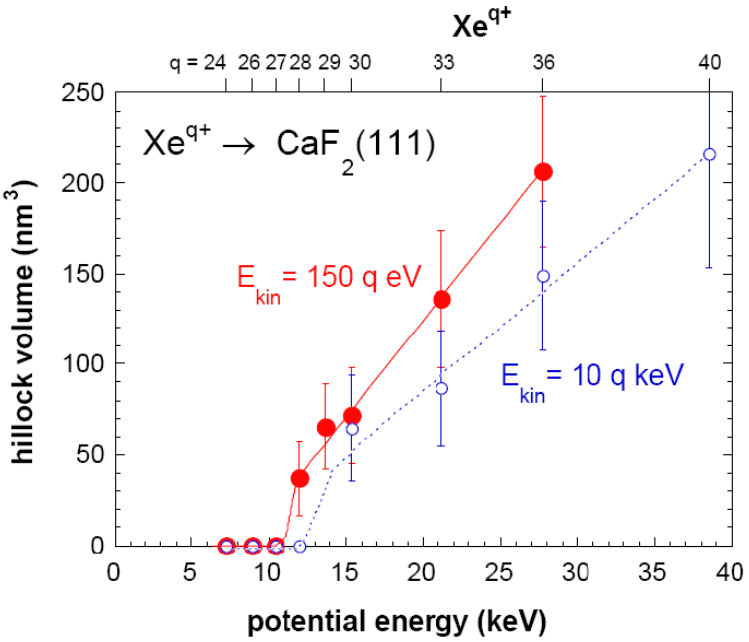

Fig. 3.2-9: Mean volume of hillock-like nanostructures as a function of the potential energy of Xe^{q+} projectiles. Full symbols correspond to measurements taken at 150 eV/q impact energies while open symbols show the results taken for 10 keV/q. Hillocks are found only above a potential energy threshold which slightly shifts with kinetic energy. Lines are drawn to guide the eye. The error bars represent the statistical variation of the actual hillock volume and are not due to the limited resolution of our AFM [4].

3.2.3.2 Discussion

In the following, results from simulations of the energy transfer from the HCI to the lattice of the CaF_2 target are presented that combine above and below surface electron emission processes along the projectile trajectory [50] with electron transport within the target material including the generation of secondary electrons and heating of the crystal lattice [7]. This sequence involves a two-fold conversion of energy: first, potential energy is converted into kinetic energy of emitted primary electrons. In turn, electrons deposit their energy in the crystal as heat, eventually leading to melting of the material. The presented simulations go to a much higher level of detail than the qualitative description of the inelastic thermal spike model presented in the previous chapter.

Highly charged ions approaching solid surfaces undergo a large number of neutralization and deexcitation processes which are well described within the classical-over-barrier model developed for metal surfaces [35] and its extension for insulator targets [50]. Electrons from the target are

transferred into highly excited states of the projectile which may decay by collisional, radiative, and Auger processes. Transfer of electrons to the projectile leaves unbalanced holes (F^0 atoms) in the surface which store part of the potential energy carried into the collision. Upon impact of the projectile the target is structurally weakened.

Projectiles reach the surface far from ground state as the time spent in front of the surface is not sufficient for a complete relaxation. At this stage, electrons are captured into moderately excited states either by resonant charge transfer from the valence band or Auger neutralization processes followed by an Auger deexcitation sequence. Along this sequence electrons with low to intermediate energies up to a few hundred eV are emitted. If inner shell holes are to be filled (e.g. in the cases of Ar^{17+}, Ar^{18+} [10]) electrons with keV kinetic energies are released. The potential energy stored in the incoming HCI will be deposited along the first few nm of its trajectory below the target surface. The kinetic energy of the projectile determines the depth within which the neutralization is completed (≈ 1 nm for 150 eV/q, ≈ 4 nm for 10 keV/q projectiles; see Fig. 3.2-10). It is much smaller than the total range of the ion in the solid (≈ 6 nm for 150 eV/q, ≈ 90 nm for 10 keV/q projectiles [72]).

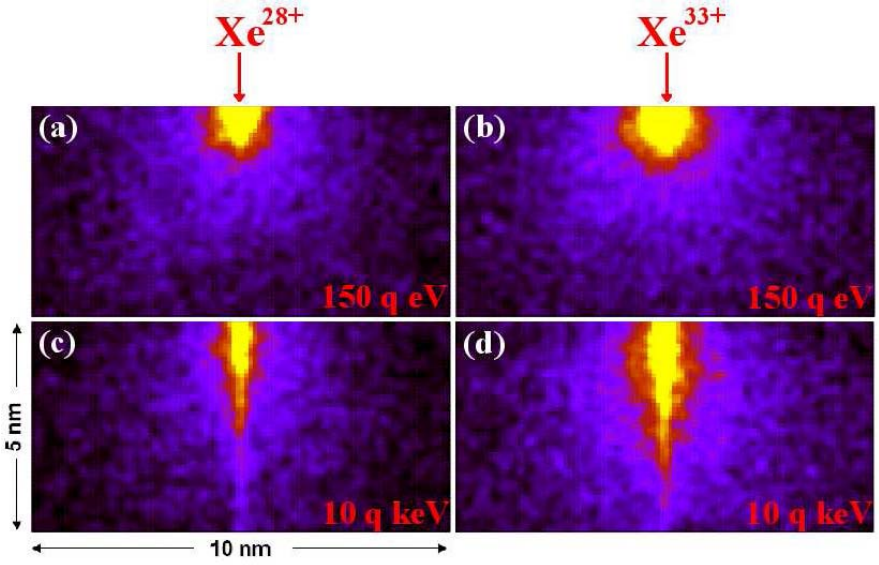

Fig. 3.2-10: Energy density deposited by Xe^{28+} (a,c) and Xe^{33+} (b,d) projectile ions in a CaF_2 crystal. Calculations were performed for impact energies of 150 eV/q (a,b) and 10 keV/q (c,d). Yellow regions represent the area in the target where the energy per target atom exceeds the melting energy. For details c.f. text [4].

For an HCI with q = 40 a number of 250 unbalanced holes is estimated to be created in the course of the interaction of a single ion affecting the crystal structure of the target. This figure is based on measurements of electrons emitted into vacuum [5] performed in the course of this thesis (see chapter 4.2.3.2) and includes an approximation of the electron emission into the solid. In the electron-transport simulation, elastic and inelastic scattering processes are taken into account leading to the creation of secondary electrons (whose trajectories are followed as well) and to excitations of phonons in the interaction with the crystal atom. Energy transfer to the lattice will eventually lead to heating and melting of the crystal. As a consequence of the high energy density required for melting of a CaF_2 crystal (≈ 0.55 eV/atom), low-energy electrons contribute more efficiently to the melting process than high-energy electrons which distribute their energy over a much larger volume because of their larger inelastic and elastic mean free paths (see Fig. 3.2-11). Contrary to naive expectations and quite surprisingly, the decisive difference between below and

above threshold charge states is not the additional fast Auger electron but the many additional slow electrons emitted along the deexcitation sequence resulting from the filling of the additional inner-shell hole.

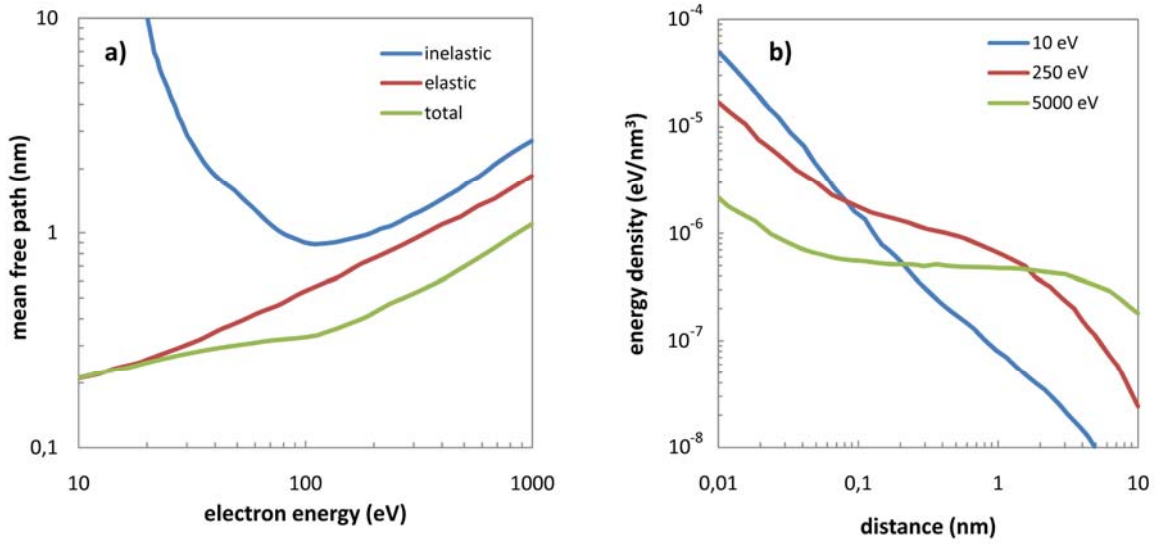

Fig. 3.2-11: Electrons travelling through a CaF_2 crystal are scattered elastically and inelastically. a) Inelastic, elastic, and total mean free paths calculated from optical data [7]. b) Average energy deposition to the CaF_2 crystal of electrons with 10, 250, and 5000 eV kinetic energy above the vacuum level as a function of distance from the point of emission. Note that slower electrons lead to a higher energy density in the immediate vicinity of their origin [7].

The average energy density deposited in the target along the trajectory as a function of the distance from the projectile track features a "hot" core (bright yellow region in Fig. 3.2-10) in which the critical energy density required for melting is reached. The shape of this volume strongly depends on the velocity of the projectile. While for slow projectiles the volume is almost hemispherical, fast projectiles create an elongated volume resembling the shape of a candle flame. If either the velocity is increased or the potential energy is reduced (smaller initial charge states) the diameter of the heated volume shrinks. While the present electron transport simulation assuming a structure less medium cannot account for effects of the crystalline structure, important information on the spatial distribution of energy deposition into the electronic degrees of freedom preceding structure modification and melting can be inferred: A minimum volume heated above the threshold energy of 0.55 eV/atom is needed for restructuring and hillock formation. The core volume in Fig. 3.2-10 a) is found to be about 2.5 nm^3 or, equivalently, about 15 unit cells of CaF_2 (lattice constant of a = 5.462 Å) containing about 102 atoms. Equally important is the linear dimension of the hot core. Only if the diameter of the core exceeds the size of the unit cell, the above-critical energy density can be retained for a sufficiently long time such that the relatively slow processes of restructuring and melting occur before cooling sets in. Hillock formation was experimentally observed for all cases displayed in Fig. 3.2-10 except for the case of fast Xe^{28+} (10 keV/q) in which the diameter of the core region is reduced to about the lattice constant. In this case the deposited energy is apparently dissipated too quickly and the melting process is suppressed.

3.3 Comparison

The present results showed for the first time that the potential energy of highly charged ions can be exclusively responsible for the production of permanent nano-sized hillocks on insulating CaF_2 single crystals. Accompanying simulations of the energy density deposited on the target atoms suggest a link of observable surface modifications to a solid-liquid phase transition. They are also able to qualitatively explain the existence and shift of the threshold charge state for hillock formation observed for projectiles with different kinetic energies.

Combining the findings of the present study with results from previous studies of nanostructuring by slow HCI impact on different materials (see chapter 2.2.2) the following picture arises [6]:

a) Under certain conditions (see below) the impact of individual slow HCI is able to produce nano-structures on surfaces very similar to the case of swift heavy ions.
b) These nanostructures have been observed not only on insulator surfaces (CaF_2, Mica, LiF) and oxides (TiO_2) but also on semiconductors (Si) and even conducting substrates (HOPG, Au).
c) Depending on the type of material, the amount of (potential) energy pumped into the topmost layers of the surface and maybe other factors like the scanning probe method used (STM or AFM) these nanostructures appear either as *hillocks* (CaF_2, LiF, Mica, HOPG, Au), *craters* (Si), *caldera like structures* (i.e. craters with rims, TiO_2, Au) or simply as *vacancy or interstitial defects* or clusters of such defects (HOPG).
d) In those cases where this was investigated (HOPG, Mica, CaF_2, Si) the size (e.g. volume, diameter, height/depth) of the generated nanostructures is nearly independent of the kinetic energy of the impinging HCI but usually strongly depends on the potential energy deposited by the HCI into the surface.
e) In the case of CaF_2 the onset of nanostructure formation is only found above a clear and well-defined threshold in potential energy (Fig. 3.2-9). Such a threshold also seems to exist for LiF and Mica (see Fig. 2.2-3 on page 17). In cases where even singly charged ions can produce defects which are visible in STM (HOPG, Si), a more pronounced increase of the feature size with increasing potential energy above a certain potential energy value indicates a threshold-like behavior or at least a second mechanism which only comes into play above a certain minimum potential energy (Fig. 2.2-5 on page 19). The occurrence of potential energy threshold(s) therefore seems to be a general feature for HCI-induced surface-nanostructures.

The decisive role of the potential energy for the formation of nanostructures can be explained taking into account the fact that damage creation in ion-surface collisions is strongly correlated to the form of energy deposition in the solid. For slow singly charged or neutral atoms, nuclear stopping dominates the energy loss. This energy transfer to target cores leads to atomic displacements and lattice vibrations in the target (phonons). For swift ions or atoms, however, scattering from the target nuclei becomes negligible, but the now dominant electronic energy loss (electronic stopping) leads to a high ionization density around the (practically straight) ion tracks [73, 74]. In addition, inner shell ionization processes produce fast electrons, which can considerably enlarge the region where electronic excitation/ionization of the target takes place. Slow highly charged ions transfer their potential energy via a series of Auger processes and the consecutive emission of energetic

electrons into a shallow region close to the HCI impact zone ([23, 28]). Although the starting point is fundamentally different to the case of swift ions, the final outcome - a strong electronic excitation of a nanometer size region around the impact site (or ion trajectory in case of swift ions) - is very similar. This explains, e.g. why surface nanostructures on HOPG produced by slow HCI and swift heavy ions look very similar (Fig. 2.2-4 on page 18) or why hillocks on CaF_2 can be produced by slow HCI above a certain potential energy threshold only [10], while a certain minimum electronic energy loss (typically 5 keV/nm) is necessary to induce hillocks on CaF_2 in the case of swift heavy ions [77, 79]. Above these thresholds the hillock size increases with potential energy [10] or electronic stopping power [79].

It is thus very plausible that also the mechanisms by which the electronic excitation of the surface is transferred to the lattice and finally leads to nanostructure formation in slow HCI surface collisions are closely related or even identical to the ones at work for swift heavy ions [92, 131]. Consequently, a modified inelastic thermal spike model [92, 128] considering the excitation of the electronic subsystem by the potential energy of the HCI and the subsequent heating of the crystal by electron-phonon coupling was successfully applied to link the two thresholds in potential energy observed for slow HCI impact on CaF_2 to phase transitions (melting and sublimation) induced by the HCI impact on the surface [10]. Simulations [7] show that the potential energy of the slow HCI is deposited in the first few layers of the target (typ. 1 - 3 nm) almost independently of the HCIs impact energy in the range 10 eV/amu < E/m < 5 keV/amu, which explains why the observed feature sizes are in first order independent on the kinetic energy of the impinging ions.

Considering this modified inelastic thermal spike model, thresholds in potential energy (see (e) above) will of course depend on material properties like free-electron density and electron transport parameters (elastic and inelastic mean free path). More systematic investigations will be needed to identify the exact mechanisms at work, which will certainly differ for the various materials.

Many questions remain to be answered like: What are the hillocks consisting of? (e.g. Fluorine depleted Ca colloids in the case of CaF_2 ?). Are slow HCI able to induce structural changes (e.g. amorphization, crystallization) like swift heavy ions? Do the thresholds (slightly) change with kinetic energy of the HCIs (and if yes, will they increase or decrease with increasing kinetic energy)?

New materials like DLC, YIG (Yttrium Iron Garnet), Al_2O_3, SiO_2, $LiNbO_3$ and many others remain to be investigated. The results will allow testing predictions based on the inelastic thermal spike model or other models (Coulomb Explosion, ...?). In lamellar material with large anisotropies, like HOPG or Mica, the energy of the electrons will preferentially be transported along the planes instead of perpendicularly, imposing an additional challenge onto modeling calculations. In materials with high free-electron density (metals), the efficient dissipation of the HCI's potential energy might prohibit the formation of nanostructures or at least enlarge the threshold energies required for their production.

And finally possible applications like HCIs as gentle tools for surface nanostructuring [38], HCI ion lithography and surface patterning [132], or tunnel barriers with HCI tailored resistance-area product [133] should be explored. Compared to the field of swift heavy ion -induced modifications of materials this new field has just started but due to the striking analogies could very much profit from the available knowledge and expertise.

Fry: "I have an idea!"
Leela: "I have a better one"
from futurama

4 Electron Emission

4.1 Experimental Methods

4.1.1 Electron Number Statistics

The electron number statistics method is well established and has been used for the last 20 years to determine electron yields and number statistics for various experiments [46, 108, 123, 134, 135]. The main principle of measurement is the application of an energy sensitive detector to measure the number of simultaneously arriving electrons on an event-to-event basis. The detector, in the present case a passivated implanted planar silicon (PIPS) detector commonly used for Rutherford back-scattering (RBS) measurements (see Fig. 4.1-1), is biased to between +25 and +30 kV, so that all of the arriving electrons, whose initial energy is usually well below 1 kV, have the same final energy. The detector electronics work with a time resolution of about 0.5 µs, and all electrons arriving within this time window are counted in one pulse where the pulse height corresponds to the total energy of the event. Thus, *n* electrons emitted due to a particular ion impact (which is finished within less than a ps) will be registered like *one* event of *n*.25 keV rather than *n* individual 25 keV events. The number of electrons emitted in a particular ion-impact event can therefore be deduced from the detectors pulse height distribution.

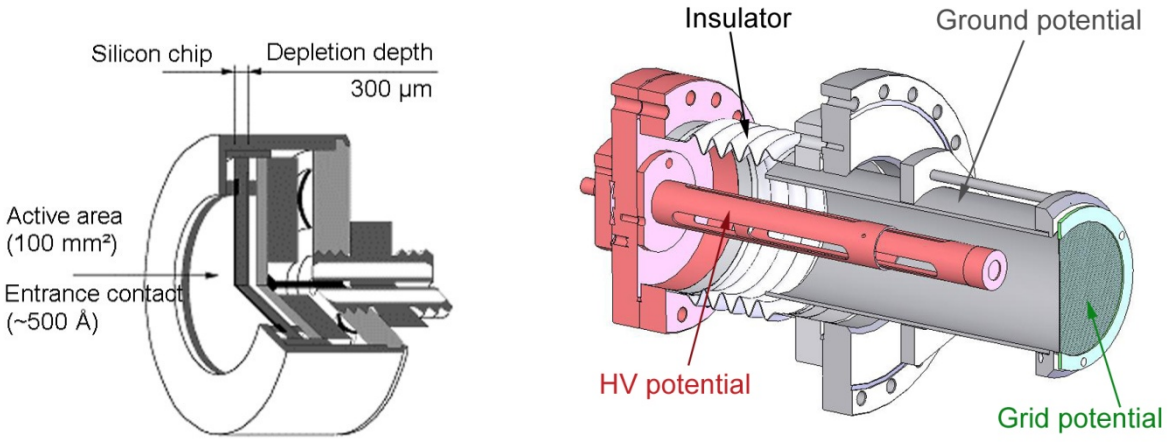

Fig. 4.1-1 left: A passivated implanted planar silicon (PIPS) detector as used for electron statistics measurements. The outer diameter of the housing is 2 cm. Courtesy of Canberra. right: The detector mounted on the UHV setup. [3]

This method counts the number of emitted electrons for every ion impact, which provides two significant advantages over any current measurement techniques [15] for electron yield measurements:

- The statistics of electron emission can be measured as well, not just the mean number of emitted electrons
- Primary ion flux can be as low as a few particles per second, as virtually no background signal is present

The second point is especially important for electron yield measurements with insulating materials, as they charge up during irradiation, which can only be successfully cancelled for very low primary ion fluxes, below the sensitivity of the best pico-amperemeters available.

The electronics for signal amplification have to be kept on high voltage together with the detector. Fig. 4.1-2 shows an overview of the electronics used throughout this work. The signal from the detector is amplified by a preamplifier and the main spectroscopy amplifier before it is passed along to a multi-channel buffer for pulse height analysis. The multi-channel buffer was realized as a standard NIM electronics device and was also kept on high voltage. This represents an improvement to previous setups, where the signal was transformed to ground potential and analyzed by a computer with an analog-to-digital-converter (ADC) card. As the signal transformer introduces a slight deterioration of the detector pulses, the present setup is thought to have an improved resolution. The NIM multi-channel buffer was read out and controlled by a computer via an optical link. A detailed description of the setup and electronics is given by Winklehner in his thesis [3].

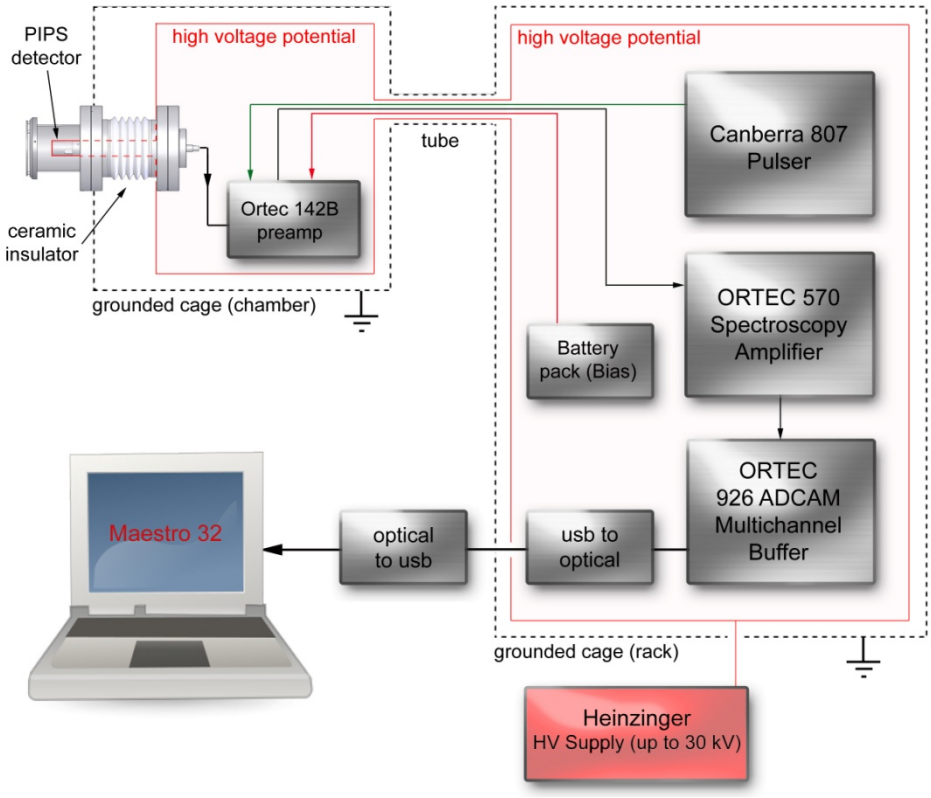

Fig. 4.1-2: Electronics for measuring electron emission statistics with a PIPS detector [3].

A typical pulse-height spectrum obtained for moderately highly charged ion impact on a gold surface is shown in Fig. 4.1-3 a). The non-negligible probability for backscattering of electrons inside the detector and the resulting partial deposition of the electron's energy leads to the smearing out of the peaks at higher electron numbers. This can be accounted for using a simple mathematical model

for the backscattering process to create appropriate fit functions for evaluation of the raw spectra [134]. Fig. 4.1-3 b) shows the results of this fit procedure, where for an appropriate choice of backscattering parameters the χ^2 of the fit can be as low as 1.1. The relevant parameters of the backscattering process are:

- The probability P_b of backscattering for an electron hitting the active detector surface
- The mean fraction E_b of the electrons original energy still deposited in the detector when the electron is backscattered

Both parameters can be determined by a careful fit of experimental spectra. The shaded areas in Fig. 4.1-3 b) correspond to the probability W_n for impact of n electrons at a time. The electron yield γ can simply be determined from

$$\gamma = \sum_n n \cdot W_n \qquad (12)$$

when the probability W_0 for emission of zero electrons can be neglected, as in this case. This method of electron yield evaluation has been described in detail in Aumayr [123, 136], as well as the diploma thesis of Simon [1].

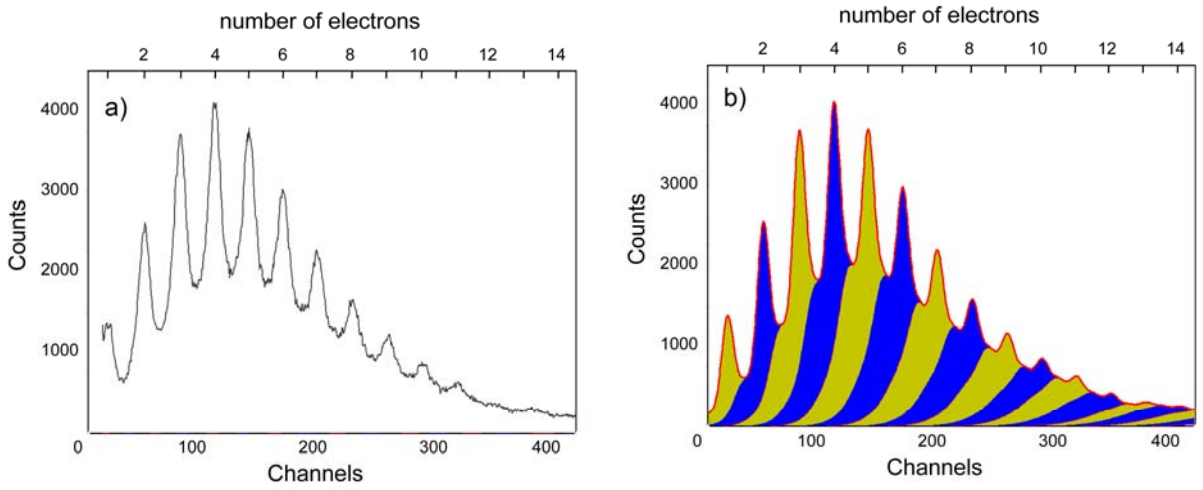

Fig. 4.1-3 a): A raw electron statistics spectrum for O^{6+} impact on gold
b) Fit (solid red line) to the experimental spectrum accounting for electron backscattering (c.f. text). The area under the nth peak corresponds to the probability for emission of n electrons per ion impact

The present setup represents a slightly modified version of the electron detection scheme described by Lemell et al. [136]. Electrons emitted from the ion-surface interaction region are extracted by a weak electric field through a highly transparent grid before they are accelerated onto the surface barrier type detector. Electron collection efficiency is a crucial point in electron statistics measurement, as it represents the largest contribution to the total experimental error. The next chapters will cover the different geometries of electrodes used to collect the emitted electrons by the grid.

4.1.2 Improved Data Analysis

Electron yields from HCI with charge states greater than 10+, as used for this study, are usually too large for individual peaks to be visible in the electron statistics spectra due to the backscattering energy losses. Fig. 4.1-4 shows a typical spectrum for such a case. The axis for the number of electrons is calibrated using the individual electron peaks seen in the previous chapter, usually obtained from high-statistics spectra of field emission events or HCI impact of contaminant species like Oxygen. The Xe^{15+} contribution in Fig. 4.1-4, however, must be treated as one single peak. Previously, these contributions were fitted by a Gaussian distribution where the center of the peak was used as the preliminary electron yield. This method, however, fails to produce correct results when the electron statistics distribution is not a perfect Gaussian, as is often the case for insulating targets. During this work, an alternative method was established by defining a region of interest for the relevant ion's contribution and evaluating its first momentum.

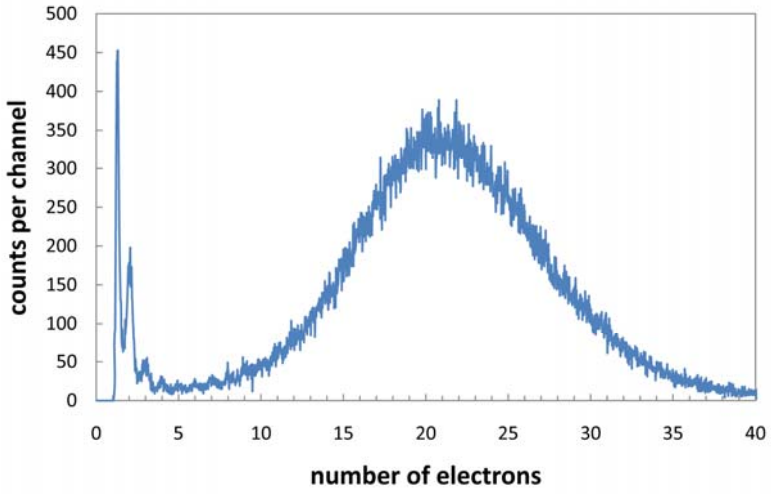

Fig. 4.1-4: Electron statistics spectrum for impact of a Xe^{15+} on a gold surface. While no individual peaks for electron multiplicities above 10 are visible, the spectrum can still be calibrated using background counts with low multiplicities (e.g. from field emission)

When the first momentum γ_{prel} of the relevant electron emission contribution is known, the actual electron yield can be determined from

$$\gamma = \frac{\gamma_{prel}}{1-P_b(1-E_B)} \qquad (13)$$

using the probability for backscattering P_B and the fraction of energy E_B deposited by backscattered electrons introduced in the previous chapter. For more details refer to the thesis of Simon [1], who has done a thorough treatment of this new evaluation method.

4.1.3 Electron Collection Geometries

The reliability of electron yields measured by means of the election statistics method depend crucially on the electron collection efficiency of the setup. It can be shown that electrons below 1 keV energy that pass the grid are focused with close to 100% efficiency onto the active surface of the detector. The grid itself has a geometric transparency of 96%, which is even enhanced by the high positive potential of the detector, as this tends to bend electrons around the grid wires. It can therefore be safely assumed that all electrons which arrive at the grid are contributing to the electron statistics signal with only a small systematic error. How to get most of the electrons emitted at the target surface to be collected by the grid, however, is not a trivial task. Electron trajectories start at the point of ion impact with a certain angular and energy distribution. For electrons originating from below the surface, the angular emission distribution can be assumed to follow a cosine law with respect to the surface normal for geometrical reasons. Electrons emitted in front of the surface might be distributed more uniformly. Some assumptions have to be made for the electron's energy distribution, as reliable measurements for very highly charged projectiles are not available. For low charge states, Kost et al. [137] have shown in 2007 that most of the electrons have energies of less than 20 eV (see Fig. 4.1-5).

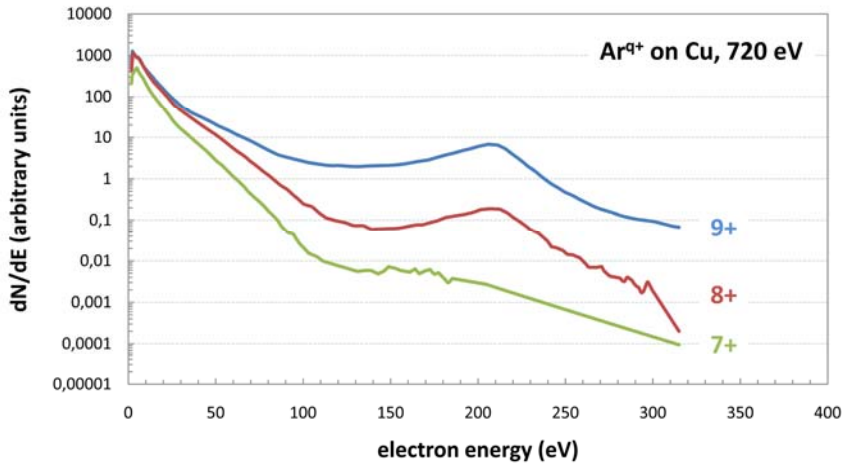

Fig. 4.1-5: Electron energy spectra for electrons emitted after Ar^{q+} impact on a copper surface show an increasing population of faster electrons at higher charge states. Primary ion energy was fixed to 720 eV. Note the logarithmic scale.

A careful analysis of the data (see Table 4.1-1) reveals that with the onset of L-shell vacancies in the primary ion (Ar^{9+}), the fraction of high energy electrons rises significantly. Clearly, for high Xe^{q+} charge states with numerous energetic L and M-shell vacancies, electrons of energies larger than 100 eV cannot be totally neglected for collection efficiency estimations.

Table 4.1-1: Evaluation of the electron energy spectra seen in Fig. 4.1-5. For Ar^{q+} (q = 7,8,9) impact on Cu, the relative fractions of emitted electrons with energies in the given intervals (from – to) are shown.

from (eV)	to (eV)	Ar^{7+}	Ar^{8+}	Ar^{9+}
0	20	88,3%	85,1%	79,3%
20	60	11,4%	14,1%	15,9%
60	350	0,3%	0,8%	4,8%

4.1.3.1 Simulations

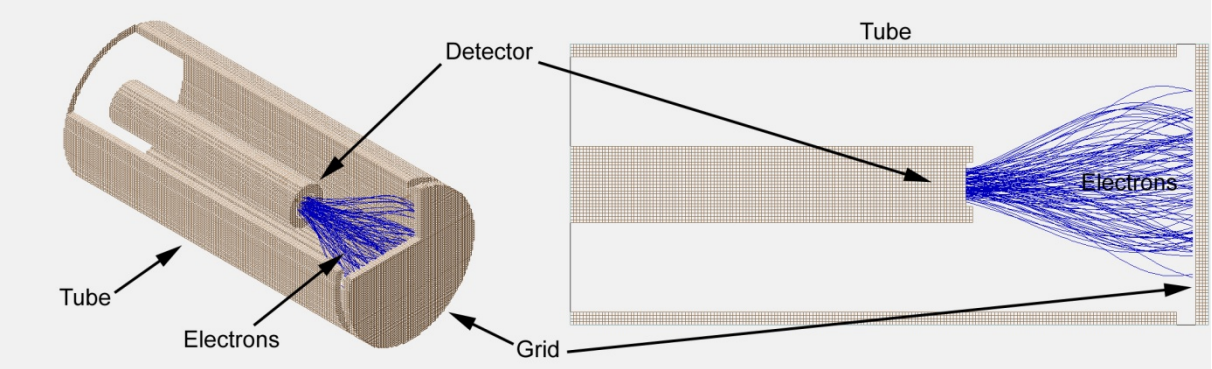

Fig. 4.1-6: SIMION simulation for the determination of the optimal distance between detector and grid. Since this distance does not influence the electron collection potential at the other side of the grid, only the part inside the tube was simulated, with electrons randomly produced at the grid [3].

In order to optimize a given setup for maximum electron collection efficiency, numerical simulations of the electron's trajectories are necessary. These simulations were performed with the SIMION 8.0 software package. This software solved the Laplace equation for a given setup and calculates the path of charged particles in its boundaries. User programs can be created to run a number of simulations for different applied potentials and particle start conditions. This way, parametric studies become possible to determine optimal values for any given setup type. The thesis of Winklehner [3] gives a detailed overview of the software and its user programming possibilities. As an example, Fig. 4.1-6 shows a simulation that proves the 100% efficiency of electron collection onto the active surface of the detector once the electrons have passed the grid. This "elephant trunk" form of putting the detector into a grounded tube that has a biased grid on its front end was used for the 90° and the fountain type geometries, as shown below. Fig. 4.1-7 shows an example of a parametric study using the SIMION package together with the LUA programming language.

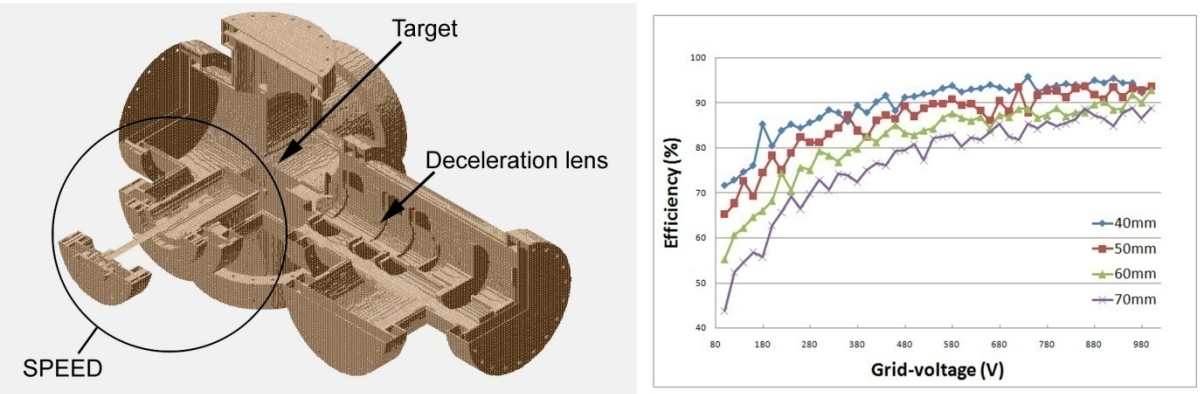

Fig. 4.1-7: Example for a 2-parameter study on the "curtain-type" geometry. The distance between the electron detector setup (including detector and grid) and the center of the chamber was varied to find the optimal value. As the optimal distance might vary with the applied grid potential, this too was varied between 100 and 1000 V. [3]

4.1.3.2 Fountain-type

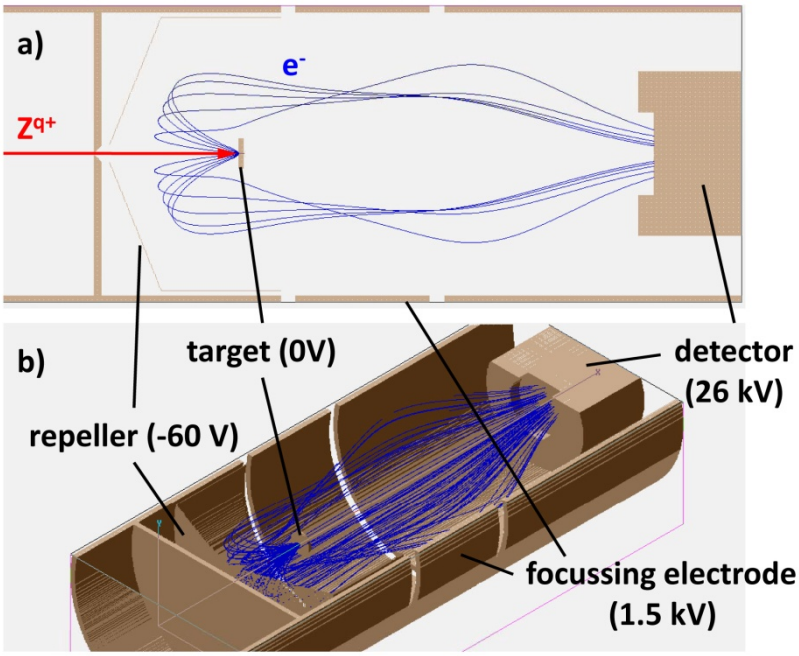

Fig. 4.1-8: 2D (a) and 3D view (b) of the principle for electron collection using the "fountain type" geometry. Calculated trajectories (blue) for 10 eV electrons emitted at between 15° and 75° with respect to the surface normal are illustrated.

First reliable measurements of electron yields for very slow HCI impact on a gold surface were performed by Aumayr et al. in 1993 [46] using the so called "fountain type" geometry. Highly charged projectiles up to Th^{80+} were obtained from the Super-EBIT at the Lawrence Livermore National Laboratory (LLNL) in the United States. Fig. 4.1-8 illustrates the principle for electron collection with this setup.

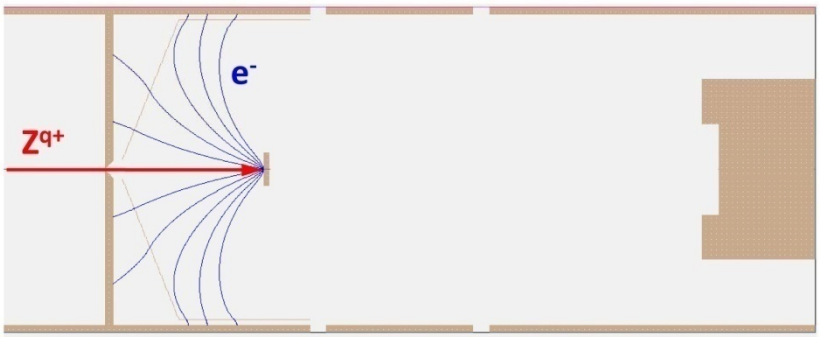

Fig. 4.1-9: Trajectories for 80 eV electrons emitted between 15° and 75° with respect to the surface normal pass the electron repeller grid and end on one of the lens elements.

The target is placed inside a three-stage Einzel-lens, and the ion beam hits the surface under normal incidence. Emitted electrons are repelled by a grid biased to -60 V, guided around the target (thus the pictorial name "fountain type") and focused and accelerated towards the active surface of the detector. As this setup is axially symmetric, the potentials can remain unchanged as the ion beam is decelerated towards very low energies, which is a huge advantage of this approach. At that time an assumption was made that the large majority of electrons is of 20 eV or less energies. Given the recent data shown in Fig. 4.1-5, this is certainly reasonable for low argon charge states, but seems to

break down for high Z HCI with numerous energetic inner shell holes. The “fountain type” geometry cannot collect electrons with energies considerably larger than the repeller potential, as they simple pass the repeller and are not turned back (see Fig. 4.1-9).

Apart from the apparent inefficiency for energetic electrons, slow electrons are also not collected with 100% efficiency. A 4 eV electron emitted in a direction close to the surface normal, for example, will be reflected back onto the target surface.

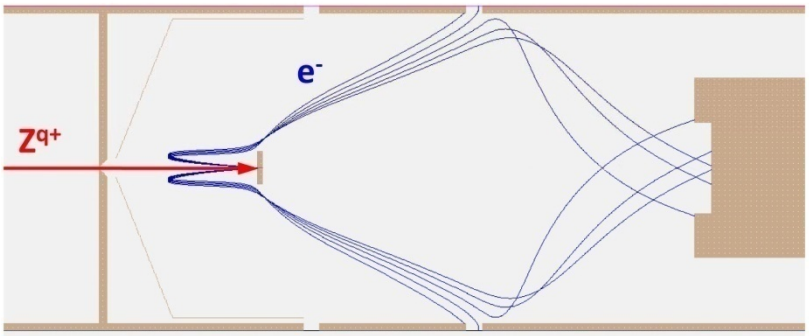

Fig. 4.1-10: Trajectories for 4 eV electrons emitted close to the loss-cone angle of 14° with respect to the surface normal. Electrons emitted under 12° - 14° either hit the lens elements or the detector housing. Electrons with larger emission angles (15° and 16° shown here) are successfully directed onto the active surface of the detector.

For any given electron energy, a loss-cone can be defined where electrons are either reflected onto the target or miss the active surface of the detector (see Fig. 4.1-10). Under the assumption that the electrons are created at the center of the target, and that the target is itself perfectly centered in the Einzel lens, the dependence of the loss-cone on the electrons energy was studied for the setup described by Kurz et al. (see Fig. 4.1-11).

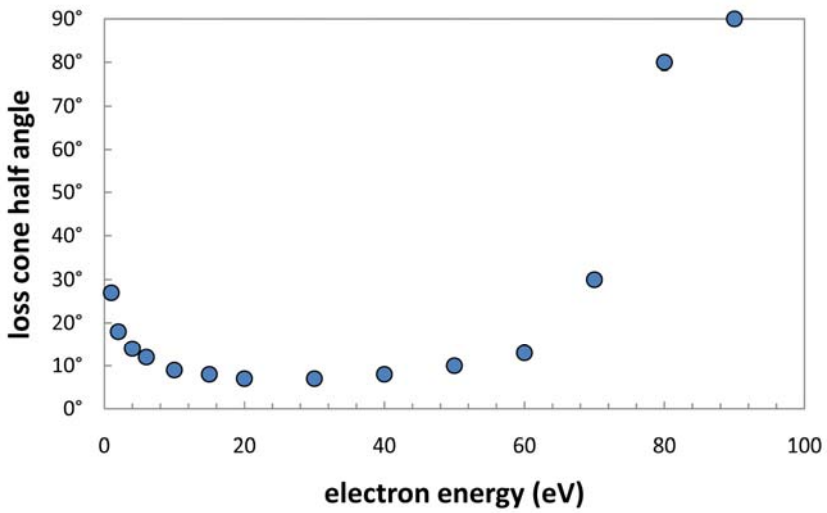

Fig. 4.1-11: The half-angle of the loss cone for electrons in the “fountain type” geometry is plotted as a function of their initial energy. Electrons emitted at angles inside the loss-cone are not collected successfully. As the electron energy surpasses the repeller bias (-60 V), the loss cone increases significantly, reaching 90° (total loss) for 90 eV electrons.

While the loss-cone is relatively large (half angle > 20°) for the lowest electron energies, it decreases to below 10° for 20 eV electrons, while it rises again towards more energetic electrons as

the repeller potential of -60 V becomes less efficient. A steep increase of the loss-cone is evident above 60 eV, until the loss-cone half angle finally reaches 90° (total loss) at 90 eV electron energy. To calculate the total collection efficiency of the setup, one needs to make some assumptions on the distribution of emission angles and energies. If the angular distribution follows a cosine-law, the loss-cone translates to a relative loss of electrons between 58% (28°) and 18% (8°) for electrons below 20 eV. For a uniform angular distribution, losses drop to between 31% and 9% for the same energy range. Since the "fountain-type" geometry cannot collect any electrons of energies above approximately 1.5 times the repeller potential (in eV), any contribution of fast Auger electrons in the velocity spectrum will also contribute significantly to electron loss.

The described evolution of the loss cone certainly depends on the actual choice of potentials and, more crucially, on the diameter of the target. Calculations shown here assume a target diameter of 4 mm. It should also be noted that the target was suspended on three metallic wires, which certainly (in a deteriorating way) influence the potentials inside the Einzel-lens, yet were not included in the simulation. It becomes apparent that using the fountain-type geometry, collection efficiencies close to 100% cannot be realized for impact of very highly charged ions on surfaces. The need for a very small target and thin suspension wires also poses a principal problem for the measurement of yields for HCI impact on insulating targets. To counter macroscopic charge-up of the insulating surface, the target has to be moderately heated to allow for ionic conductance to set in (c.f. chapter 4.2.2). How this can be achieved on a crystal of only a few mm diameter with minimal supporting wires and without contamination of the electron spectrum by thermionically emitted electrons from the heating element is a problem not easily solved.

4.1.3.3 90° type

The problems with collection efficiency and heating capacity associated with the "fountain type" geometry described in the previous chapter lead to the search for a different collection geometry. For moderately slow projectile ions in the range of a few tens up to a few hundreds of keV kinetic energy, the influence of the collection potentials on the ion's trajectories can be neglected. For this velocity regime, the setup developed by Lemell and Stöckl [136] for measurement of electron yields of HCI impact on insulating targets under grazing incidence in coincidence with projectile energy loss [107] was adapted. For the electron branch of their experiment, they used a "90°" geometry where the detector was put inside a tube and rotated 90° with respect to the ion beam axis. To allow for higher collection efficiencies at normal incidence of the projectile (which was the goal of the present study), an electron repeller electrode was introduced during this work to help bend the electrons towards the detector (see Fig. 4.1-12).

The thesis of Simon [1] gives a detailed description of this setup and the considerations for electron collection efficiencies. In summary, the collection efficiency for impact angles larger than 45°, where the target is facing the detector, is close to 100%, while for close to normal incidence it drops to about 80%. A set of correction factors for the collection efficiency was obtained empirically. This was achieved by measurement of electron yields from a gold surface, where theory predicts that potential emission only depends on the normal component of the impact velocity. By varying the ion beam energy and impact angles, a set of redundant data was collected, where the same normal component of the velocity was realized at different angles, thus allowing a good estimation of the collection efficiency (see Fig. 4.1-13).

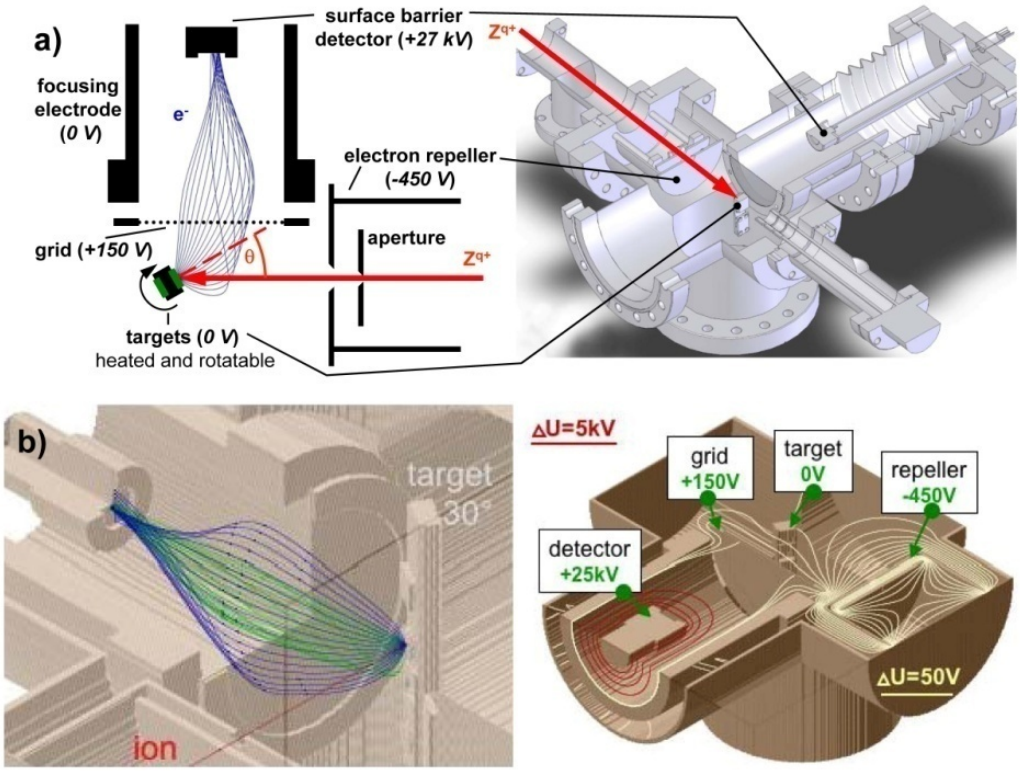

Fig. 4.1-12: a) Sketch of the 90° electron collection geometry. Electrons are collected by the negative potential of the repeller and the positive potential of the grid. The electron trajectories (blue) are the result of actual ray-tracing calculations with SIMION 8.0.
(b) SIMION calculations showing equipotential lines (red and yellow) in the chamber and simulated electron trajectories for 10 eV electrons starting in the horizontal plane (green) and in the target plane (blue) [5].

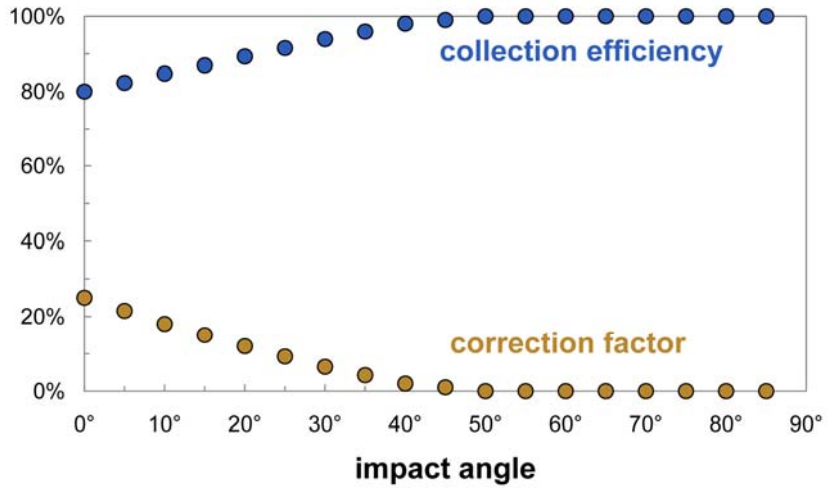

Fig. 4.1-13: The empirically obtained electron collection efficiency of the "90°" geometry reaches 100% for impact angles larger than 45°. Yields obtained at smaller impact angles have to be corrected for collection efficiency with the given set of factors.

This setup allows for a larger target holder than the "fountain type" geometry, thus heating of the insulating targets during measurements was easily possible. The target holder allowed for up to three different targets to be mounted at the same time, so that for every data point obtained for an

insulating target, a reference point for a gold target could be made as well. In retrospect, however, this approach creates severe problems for the surface preparation of the targets. As the insulating targets are kept around 200° C during measurements, outgassing leads to a severe deterioration of the gold surface (which increases measured yields). Reliable absolute yields from the gold surface were thus only obtained after thorough sputter cleaning of the surface without intermittent measurements on the insulator.

4.1.3.4 Curtain type

The "90°" collection geometry falls short of being able to measure yields for very slow primary ion beams. The positive grid potential exerts a lateral force on the incoming ion beam, which will therefore be severely deflected when the source potential of the beam becomes comparable to the grid voltage. As the Two-Source-Facility of the Forschungszentrum Dresden/Rossendorf (FZD) is able to provide beams of up to Xe^{44+} from source potentials down to less than 10 V, a significant adaptation of the setup became necessary. Since electron yields measured in the "90°" geometry were shown to be reliable, the basic concept of the setup was kept. In order to allow for very slow ion beams, the target was mounted off the main manipulator axis. Since the ion beam would surely be deflected by the grid potential, the target was to be moved into the tilted beam. This way, the target surface faces the detector also for normal incidence, a fact that was found to guarantee high collection efficiencies earlier. The first approach to realize this can be seen in Fig. 4.1-14. The target holder is mounted on a UHV compatible stepper motor, at about 20 mm out of the axis of the main manipulator. This way, the target can be moved into the beam while the impact angle cans still be chosen freely. The eccentricity of the target can be chosen appropriately.

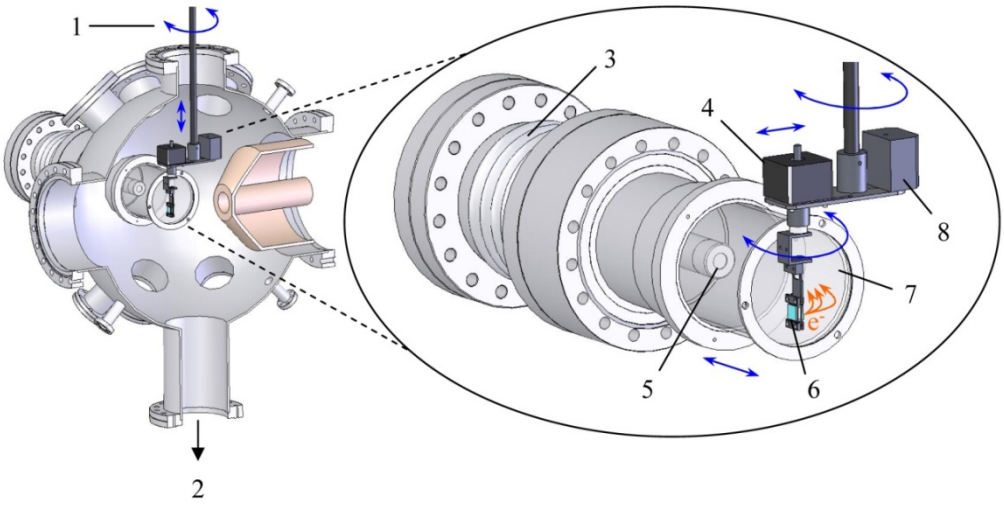

Fig. 4.1-14: The first realization of an out-of-axis target for very slow HCI beams delivered by the FZD facility. Parts as follows: 1) main manipulator axis 2) turbo pump 3) insulator 4) UHV compatible stepper motor 5) detector) 6 target holder 7) grid 8) counterweight. Image courtesy of R. Heller

This setup worked very well down to impact energies per charge state of about 300 eV/q, where the reference measurements on a conducting gold surface (c.f. chapter 4.1.3.3) showed significant deviations from the expected electron yields. In order to improve the insufficient collection efficiency, additional electrodes were introduced to allow full control of the extraction and ion guidance potentials. Two of these electrodes were realized as a sequence of hanging wires, thus the pictorial name "curtain type" was given to this setup (see Fig. 4.1-15).

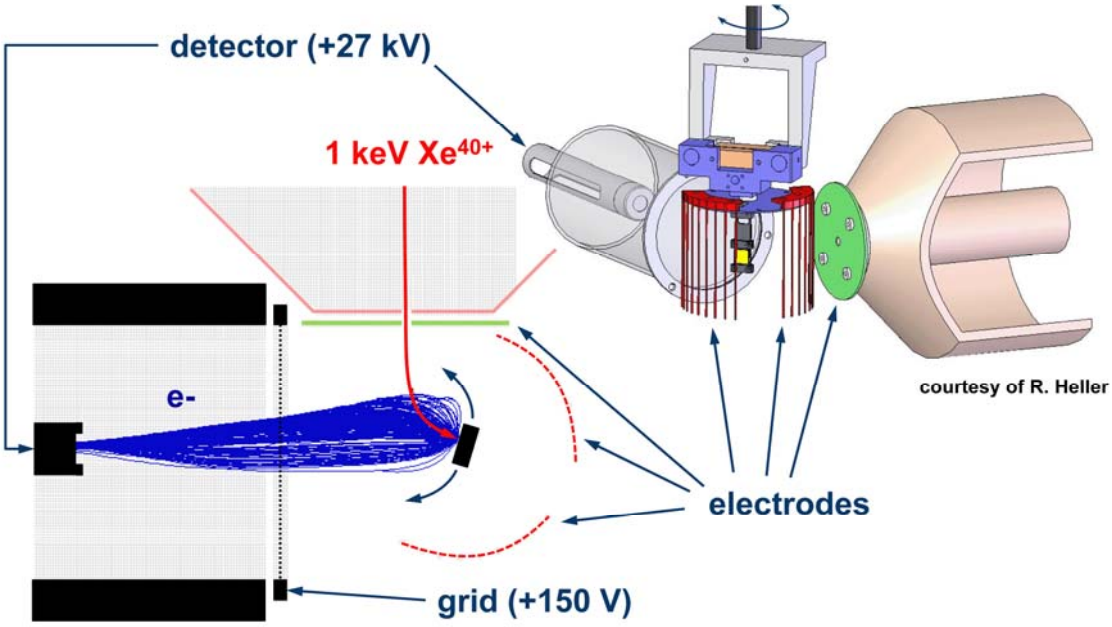

Fig. 4.1-15: For measuring electron yields for very slow HCI (red) impact on insulator surfaces using the "curtain type" geometry, the ion beam is bent by the positive grid potential to hit the tilted target at close to normal incidence. The extraction potential can be fine-tuned using the additional "curtain" (red) and repeller (green) electrodes to achieve high collection efficiency for emitted electrons (blue).

To allow a quick change of target holders via the lock-load system of the irradiation chamber at FZD without breaking the ultra-high-vacuum, the UHV stepper motor was removed from the setup, as it was simply too big to fit through the lock.

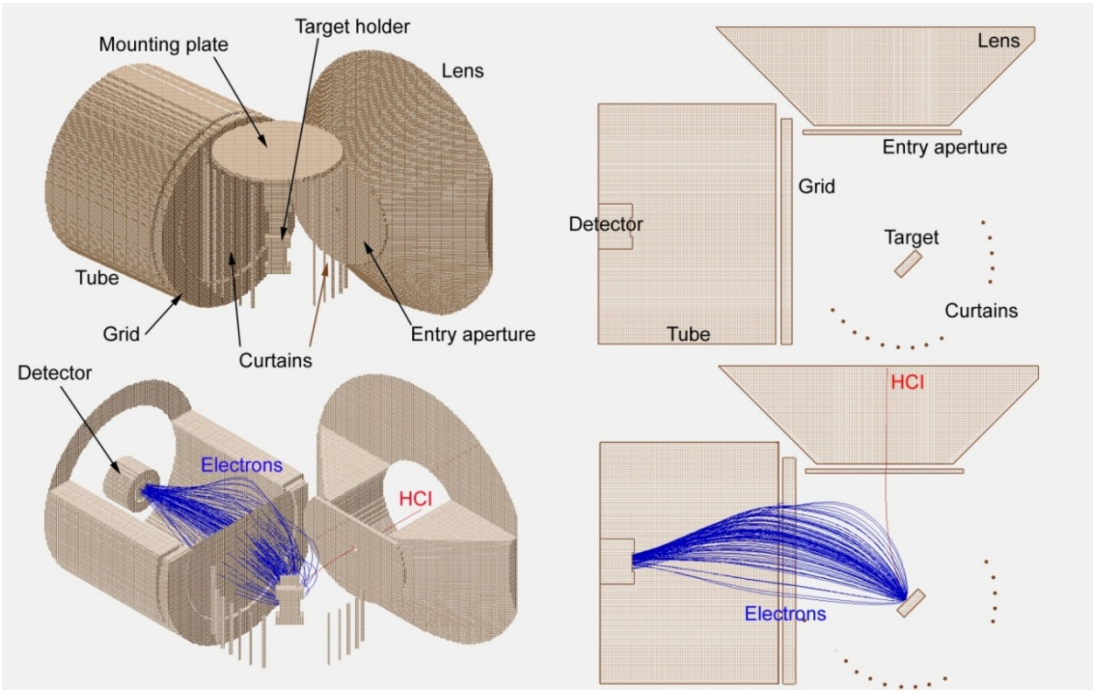

Fig. 4.1-16: To verify the feasibility of the curtain-type electron collection setup, both the ion beam and the emitted electrons had to be simulated. Varying the distance between detector setup and the center of the chamber as well as the eccentricity of the target, optimal conditions for HCI beams of different energies were obtained [3].

Apart from the two “curtain” electrodes, an electron repeller was mounted on the exit of the last deceleration lens element of the beamline. SIOMION simulations of the setup were performed extensively to find optimal conditions for electron collection over a wide range of impact energies (see Fig. 4.1-16). Assuming a cosine-law for the angular distribution of emitted electrons, the collection efficiency was calculated as a function of the electron energy (see Fig. 4.1-17). It is observed that up to 20 eV electrons are captured with close to 100% efficiency, while electrons with as much as 200 eV are still collected with at least 50% efficiency. The efficiencies drop to near total loss for electrons of more than 500 eV energy, as the collection potentials are too low to influence their trajectories significantly. For high energy electrons, the collection efficiency basically reflects those electrons which fortuitously start in the right direction anyway. The calculated collection efficiencies presented here by far surpass the relative efficiencies of the “90°” and the “fountain-type” geometries. Simon was able to reproduce the empirically found overall collection efficiencies of the 90° setup just by introducing a significant contribution of electrons in the range of 40 – 100 eV [1].

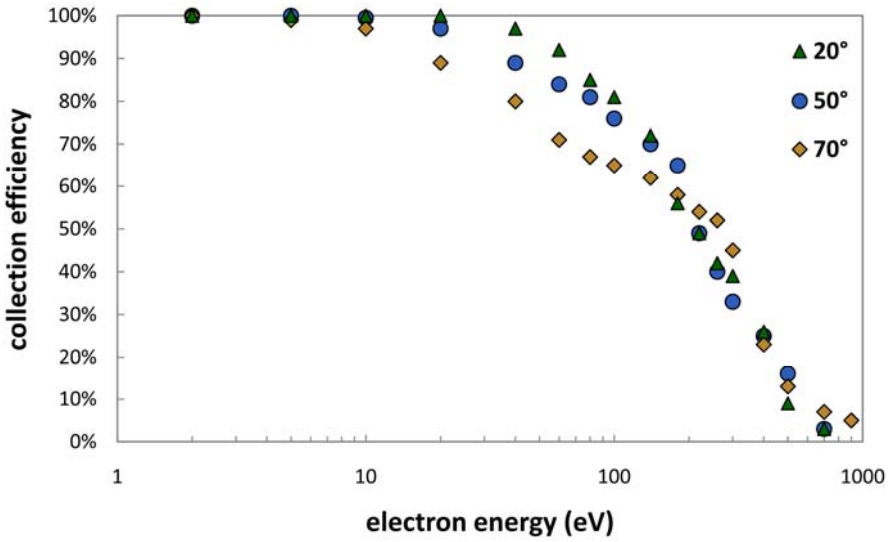

Fig. 4.1-17: Assuming the angular distribution of emitted electron follows a cosine-law, the collection efficiency of the curtain type setup was calculated as a function of the electron’s energy for three different target tilt angles: 20° (representative for ion beams of 500 eV/q or more), 50° (180 eV/q beam) and 70° (25 eV/q beam).

The conservation of overall problems (closely related to “Murphy’s law”) suggests that the high collection efficiencies achieved with the curtain type setup come at the expense of some drawbacks in other details. The biggest problem associated with the present setup is the necessity to adjust the collection geometry with decreasing beam energies. As the beam gets slower, it is bent more by the grid potential and the target has to be moved into the beam to counteract. This of course changes the collection geometry and the collection efficiencies, which is also demonstrated by Fig. 4.1-17. In order to reliably measure electron yields as a function of the projectile’s impact velocity, careful measurements with a reference target of known velocity dependence are required. As the “fountain-type” setup certainly yields the correct velocity dependence (no change in any parameters as the beam is decelerated), measurements with this setup for HCI impact on gold were used as a reference for the present setup. Chapter 4.2.4.1 compares yields measured with both setups and shows that the curtain-type setup is able to reproduce the known velocity dependence very well down to ion energies per charge state as low as 10 eV/q.

Another setback is the lack of knowledge with respect to the actual impact angle. The direction of the beam at the point of impact can only be obtained by computer simulations. Thus, for every set of parameters the impact angle has to be calculated to make sure it is close enough to normal incidence. Fig. 4.1-18 shows the results of such a simulation for a 150 eV/q beam at standard collection potentials applied to the available electrodes.

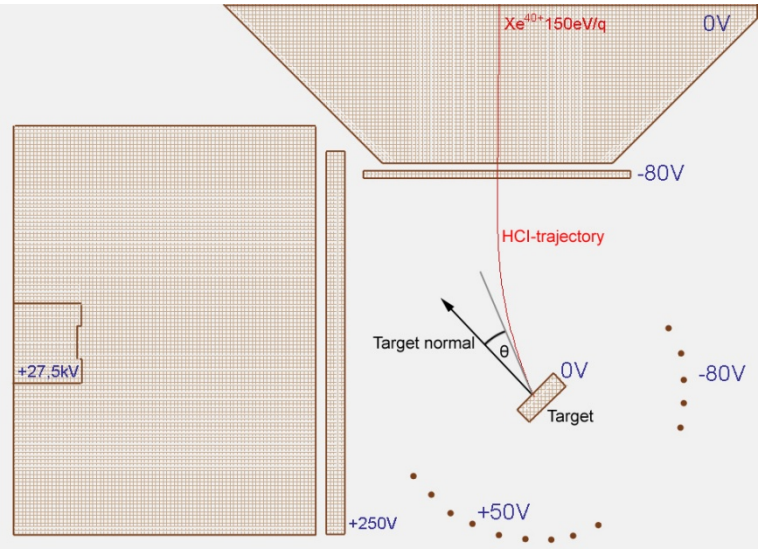

Fig. 4.1-18: For a reasonable evaluation of electron yields measured in the curtain type geometry, the angle of incidence θ of the ion beam on the target had to be determined by ray-tracing simulations, as this parameter cannot be determined experimentally.

The main manipulator of the FZD irradiation chamber allows for lateral movement of the target up to 12 mm in each direction. Using these additional degrees of freedom, the target can be rotated up to about 30° when the eccentricity of the target is 20 mm at a given location in the X,Y plane. This way, the impact angle of the ion beam was always kept below 20° with respect to the surface normal. The dependence of electron yields on impact angle is usually very weak for the first 30°, so the uncertainty in actual impact angle does not introduce a large error into the measurements. As the impact angle dependence of electron yields was of much less interest than the now available velocity dependence, the limitation to close-to-normal impact angles was not deemed a major disadvantage.

4.1.4 Ion Beam Scan Electronics

The concept of an electron beam ion trap (EBIT) has been explained in chapter 2.1.3. Most EBITs utilize superconducting magnets which not only provide the necessary compression of the electron beam but also allow for cryo-pumping of the trap region. The base pressure in an EBIT is therefore quite low (≤ 10^{-10} mbar). However, cryo-pumping also conserves a memory on previously used other working gases. Extracted ion beams therefore usually do not only contain ions of the desired working gas in different charge states but also a mixture of different ion species with comparable mass-to-charge ratios. Mass scans of ion beams extracted from an EBIT usually performed with an analyzing sector magnet can thus be quite complex, with the ions of interest not identifiable in a straight-forward manner.

This chapter will introduce the necessary electronics for a novel method to unambiguously identify highly charged ions extracted from an EBIT. It utilizes the potential emission of electrons as induced by ion impact on a metal surface. Results from this method are given in chapter 4.2.1.

The details of the Heidelberg EBIT [67] are given in chapter 2.1.3.1. In its continuous mode of operation, also referred to as leaky or dc mode, those ions with sufficient thermal energy can escape the trap by overcoming the electrostatic barrier at the confining drift tube held at constant potential. Extracted ions are replaced continuously by injected gas atoms. The extracted ion beam contains different ion species with various charge states. The ion beam is focused by an Einzel-lens and transported to the experimental chamber via a 90° analyzing magnet which is used to separate ions with desired mass-to-charge.

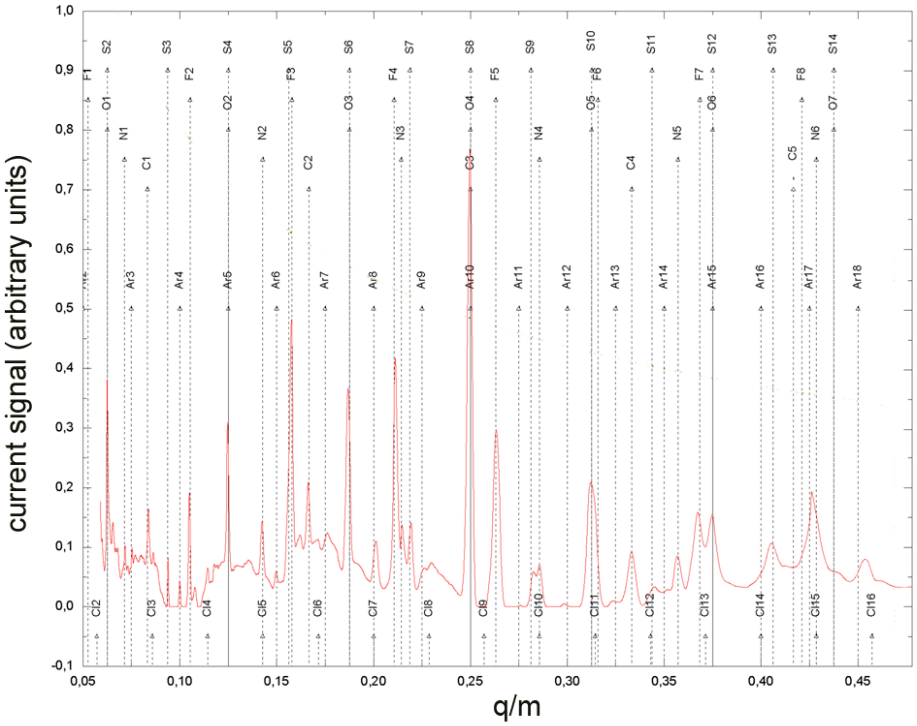

Fig. 4.1-19: Typical mass scan of ions continuously extracted from an EBIT obtained by a sweep with the analyzing magnet over a Faraday cup. The Faraday cup current is plotted vs. the inverse square of the field of the analyzing magnet (converted into a charge-to-mass ratio). Unambiguous ion identification can be very challenging under these circumstances.

For the present study the central drift tube of the EBIT is biased to +6.4 kV, with the trap potential set to +210 V. 360mA emission current from the electron gun leads to a space charge potential of -510 V. That determines the ion extraction energy of 6.1 kV. The electron gun itself was biased to -7.5 kV, which together with a cathode bias of another -1.5 kV yields an electron beam energy of 14.9 kV, sufficient to produce bare Ar^{18+}, He-like Xe^{52+} or Ne-like W^{64+}.

A typical mass over charge scan showing the number of transported ions versus the field of the analyzing magnet (already converted into a mass-to-charge ratio) for continuously extracted ions is shown in Fig. 4.1-19. For this scan ^{129}Xe has been used as working gas, but the ion beam is apparently strongly contaminated and even dominated by residual gas ions (mainly oxygen and carbon) as well as by still present ions from ^{40}Ar (used as working gas shortly before). There is no possibility to distinguish between ions with identical mass over charge ratio with a scan like this. In our simple EBIT diagnostic device the ion beam enters a differentially pumped UHV chamber before hitting a clean metal surface under close to 30° angle of incidence (see chapter 4.1.3.3). In our case we use a sputter-cleaned, single crystalline Au(111) target, but any other clean (polycrystalline) metal surface would do as well.

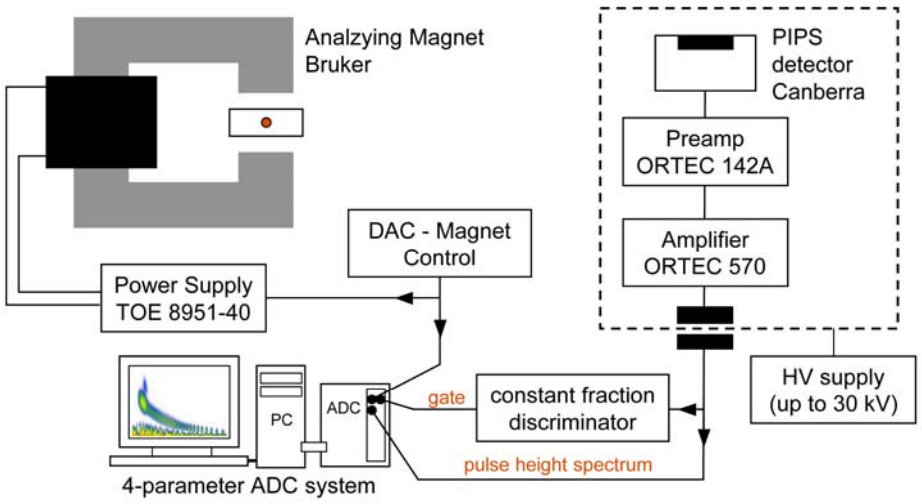

Fig. 4.1-20: Electronics for a charge state resolved ion beam scan incorporate the standard electronics of an electron statistics setup (in the high voltage cage). The pulses usually fed into a pulse height analysis system are then used to trigger the acquisition of the current sector magnet control voltage (determining the current m/q selection) and both values are recorded by a multi-parameter system to make up a 2 dimensional plot. [13]

A electron statistics detector setup as described in chapter 4.1.1 was used to detect the number of electrons emitted in every ion impact event. In general, if slow (impact velocity << 1a.u., corresponding to 25 keV/amu) HCIs collide with a metal surface, the majority of electrons is emitted by potential emission (PE), where the potential energy of the ion (i.e. the sum of all ionization potentials) rather then it's kinetic energy (giving rise to the so-called kinetic emission – KE) dominates the total electron emission process [23, 75] (see Chapter 2.3.1). PE from metal surfaces has been found to strongly increase with the ion potential energy and hence it's charge state [46, 75].

It is the information on the precise number of the emitted electrons which allows us to separate ions with identical or very similar mass-to-charge ratio (see chapter 4.2.1). To this purpose the

analyzing magnet is continuously scanned while for each individual ion impact event the number of emitted electrons is recorded in coincidence with the actual value of the magnetic field (Fig. 4.1-20). For this technique typical projectile fluxes at the target must not exceed a few ten-thousand ions per second in order to avoid pulse pile-up, but may be as low as a few ions per second, which in fact makes the present method ideally suited for use with an EBIT ion source. The diploma thesis of Martin Simon [1] provides a more detailed description of the beam line setup in Heidelberg and the electronics of the qRIBS setup.

4.1.5 Timing Electronics

During the course of this work, indications of a peculiar time structure of the raw pulses from the electron statistics detector were found. Apparently, there was an increased appearance of small pulses (corresponding to few electron events) shortly after a large pulse from a HCI impact on the insulator surfaces. This was first discovered for the KBr surface, where this material is known to form color centers (i.e. electrons trapped at a negative ion's lattice site) which may decay via electron emission after some time. To further investigate what seemed to be delayed emission of electrons after HCI impact, the measuring electronics were adapted to not only analyze the pulse height, but also the time passing between pulses of certain heights. For a more detailed description of the observations that led to this conclusion, refer to the thesis of Winklehner [3].

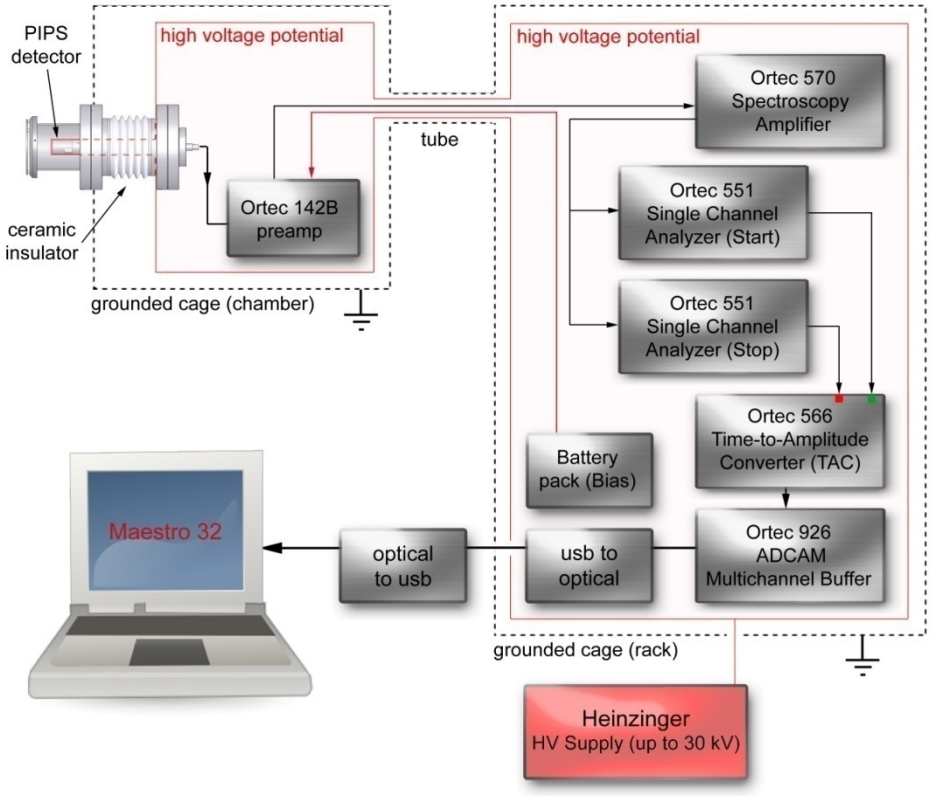

Fig. 4.1-21: Modified measurement electronics for time structure analysis. Two single channel analyzers which trigger on pulses of predefined height provide the start and stop signals for time measurement by means of a Time-to-Amplitude converter which is then fed into the multi-channel analyzer [3].

In large parts, the electronic setup for the time-structure measurements is the same as for regular electron statistics measurements (see Chapter 4.1.1). As seen in Fig. 4.1-21, the signal obtained from the PIPS surface barrier detector is amplified by the preamplifier *Ortec 142B* and the spectroscopy amplifier *Ortec 570*. It is then handed over to the timing branch, consisting of:

- *Two Ortec 551 Single Channel Analyzers (SCA).* Both operate in *window-mode*, i.e. they fire a logical output pulse when the input signal amplitude is within a predefined upper and lower limit (set by the user). Output can be both positive and negative NIM-standard. Negative NIM-standard is faster thus used in this application.

- *Ortec 566 Time-to-Amplitude Converter (TAC).* The TAC measures the time between a start- and a stop-signal (both fast negative NIM-standard) and converts it into an amplitude (0-10V). The time window can be set from 50ns to 2s.

Both SCAs get their input from the spectroscopy amplifier. Usually, the start-SCA is set to an energy window corresponding to HCI impact events, while the stop-SCA is set to an energy window corresponding to anything that is significantly smaller than the main event, but above white noise. The time between start-signal and stop-signal is then converted into a voltage (amplitude) by the TAC. As in electron statistics measurements, the Multi-Channel-Buffer (MCB) counts the amplitudes into corresponding channels by means of pulse-height-analysis.

When the energy windows of start and stop-SCA are set to overlap, as for example when measuring the time structure of the ion beam itself (both SCA windows set to main events), one has to be careful to adjust the signal path for the stop signal to arrive at the TAC up to a fraction of a microsecond earlier than the start signal. Otherwise, as both SCAs are fed by the same input signal, the same signal would first trigger the start of time measurement, as well as the stop shortly thereafter. Effectively, one would not measure the time relation of two different pulses, but simply the electronic delay in signal path for one and the same pulse.

"I am already sciencing as fast as I can!"
Prof. Hubert Farnsworth of futurama

4.2 Results and Discussion

4.2.1 qRIBS - A Novel Tool for Ion Beam Analysis

In Fig. 4.2-1 the number of emitted electrons has been added as a second dimension to the mass over q scan shown in Fig. 4.1-19. Each ion impact event is now characterized not only by the respective nominal charge to mass ratio (x-axis) but also by the amount of emitted electrons (y-axis). A series of distinct peaks are visible in this 2D-spectrum. While residual gas ions (O^{q+}, C^{q+}, etc.) are most prominent in intensity, their charge state (and potential energy) is comparably low, resulting in an electron emission yield of typically less than 10 e^-/ion. They can thus easily be discriminated from higher charged ions like the full series of Xe^{q+} ions (q = 13 - 51). The series of HCIs from ^{40}Ar is still visible and clearly separated from the Xe^{q+} HCIs in the 2D-scan of Fig. 4.2-1.

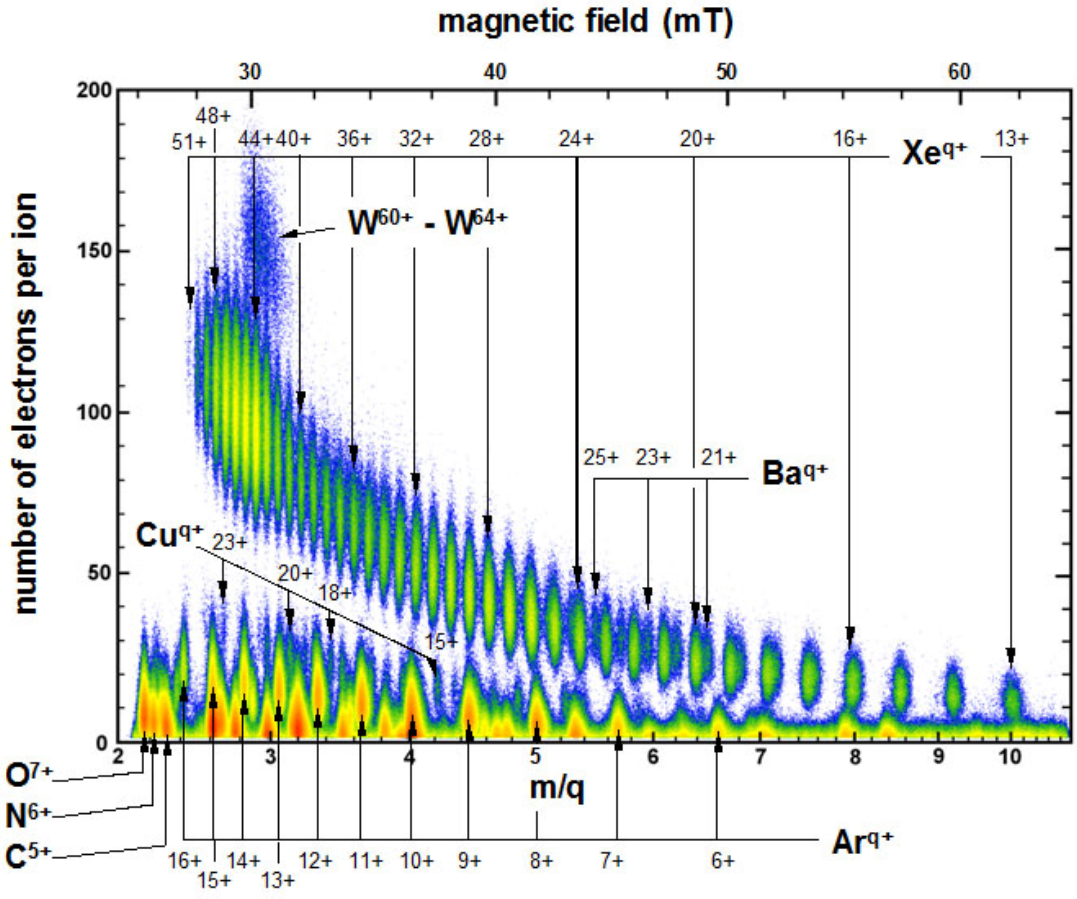

Fig. 4.2-1: For all ion impact events the number of emitted electrons is recorded together with the actual value of magnetic field of the analyzing magnet converted into ion charge-to-mass ratio for a two dimensional plot allowing the unambiguous analysis of a mixed ion beam. Total scanning time for this spectrum was 30 minutes. [13]

Fig. 4.2-2 shows a projection of all events in the 2-D plot onto the m/q axis. While the most prominent ions species could have been identified in a careful magnetic mass scan alone, the 2D scan

in addition allows identifying trace ion species in the spectrum as well. Ions ejecting more than 150 electrons per impact event carry a higher charge than all Xe projectiles used. These ions were identified as W^{q+} ($60 \leq q \leq 64$) HCIs from the cathode material of the EBITs electron gun, successively trapped and ionized in the EBIT itself. As three significant isotopes of tungsten are present (m = 182, 184 and 186), the individual charge states cannot be separated anymore. Small peaks between the Xe^{q+} peaks in the region $19 \leq q \leq 21$ point to ions with similar mass but slightly higher charge state than Xe (because of the slightly higher electron emission yield). They are identified as Ba^{q+} ($20 \leq q \leq 25$) ions (also originating from the e-gun). Cu^{q+} ($15 \leq q \leq 23$) ions (material of the EBIT drift tubes) and traces of sulfur and fluorine HCIs are visible in the vicinity of the Ar^{q+} peaks. Note that the Ba^{q+} series has a different spacing on the mass-over-charge axis between its individual peaks than the Xe^{q+} series. Due to this fact it is possible to distinguish even between two species which have similar mass and charge, which would be impossible using a 1D electron number spectrum alone, as their electron yields are very similar.

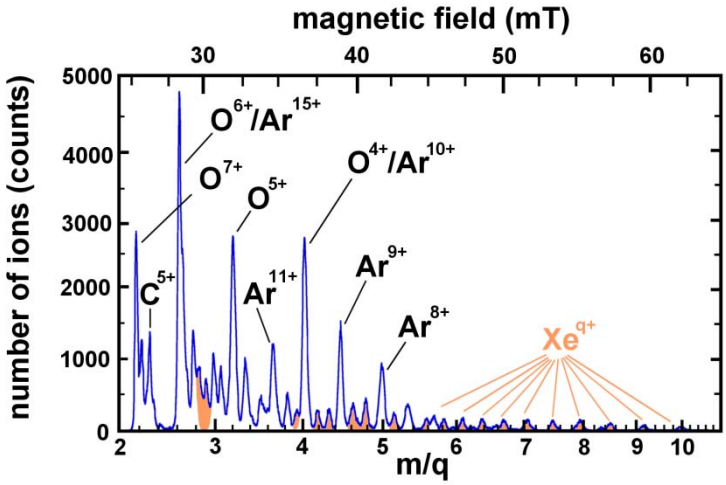

Fig. 4.2-2: Typical mass scan of ions continuously extracted from an EBIT showing the number of transported ions vs. the field of the analyzing magnet (converted into a mass-to-charge ratio). Unambiguously identified Xe^{q+} peaks are shaded. [13]

A "partial" Xe^{q+} mass spectrum can be obtained (Fig. 4.2-3) by properly selecting the region of interest as shown in the insert. Such a pure Xe spectrum is very convenient for an easy calibration of the relation between the field of the analyzing magnet and the mass-to-charge scale. The image also shows a distinct drop in rates for charge states higher than Xe^{44+}. Apart from the choice of extraction parameters, this is also explained by the high ionization energies of the L shell and the fact that the trapping force in an EBIT increases linearly with q. Hence, the higher charge states are always underrepresented in an extraction spectrum from an EBIT in leaky mode, as the trap preferentially expels ions with lower charge states in a process called evaporative cooling. This also explains the presence of a population of tungsten in charge states from 60 to 64 with ionization potentials from 6.1 keV to 7.1 keV, and the lack of its lower charge states. Tungsten is accumulated in the trap very slowly, in a time in the order of minutes and therefore, all tungsten ions reach a very similar charge state.

In case the target is mounted on a manipulator, the HCIs of choice selected in this way can subsequently be used for performing experiments further downstream by simply retracting the

target. In the case of a true mass-to-charge coincidence between two different ion species, the ratio between the two HCI-species can at least be quantified [138] (due to an almost 100% efficiency of HCI detection because of the high electron yields involved) and also optimized by tuning the ion source parameters.

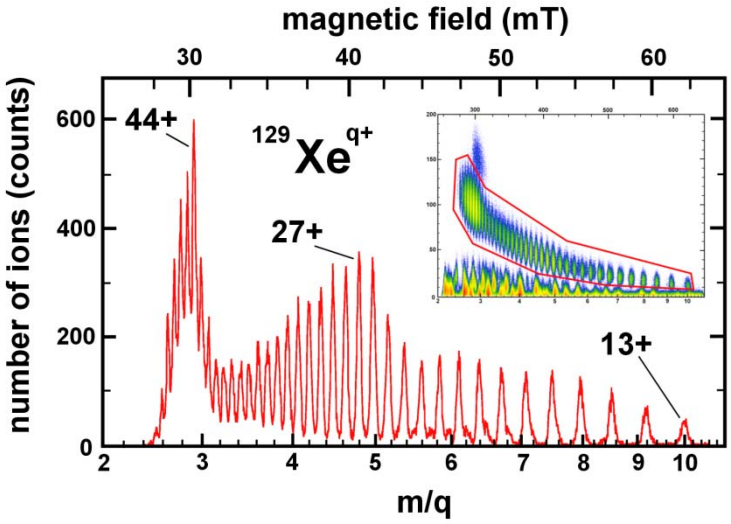

Fig. 4.2-3: A "partial" Xe^{q+} mass spectrum as obtained from Fig. 4.2-1 by properly selecting the region of interest as shown in the insert and projecting all events in this region onto the m/q axis. [13]

This novel beam scan technique not only provides a complete quantitative analysis of all ion beam fractions, it is also easily implemented, well suited to be incorporated into an existing beam-line and can be performed in a time comparable to that of a usual ion beam mass scan (typically 20 minutes).

4.2.2 Charging Effects

With an insulating target at room temperature, significant charging of the surface was observed during HCI irradiation even for the very small ion fluxes obtained from an EBIT (typically 10^3 – 10^4 ions/sec). Fig. 4.2-4 a) shows the reduction in electron yield over time due to a charging-up of the surface even at a primary ion current of less than 1 pA. This can be understood as a drastic reduction of the collection efficiency of the electron statistics setup due to a local charge patch forming on the insulating surface. Electrons with a kinetic energy of less than the local surface potential have a high chance of being reflected back onto the surface by the grounded apparatus walls, which then have a negative potential with respect to the electron's point of origin.

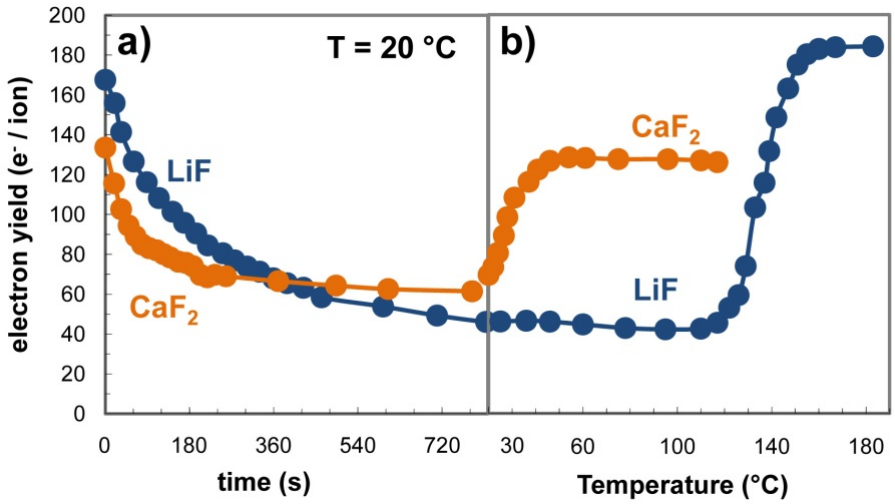

Fig. 4.2-4: (a) With the targets at room temperature, measured electron yields from insulating LiF and CaF_2 surfaces decrease over time during bombardment with 0.01 pA (electric) HCI. A global charging up of the surface is responsible for this effect, as it does not allow slower electrons to escape from the surface.
(b) The original electron yields can be restored by applying moderate temperatures to the targets. The onset of ionic conductance then cancels the charge-up between any two ion impacts. Above the necessary temperature, which depends on target thickness and primary ion current, electron yields are independent of the applied temperature. [5]

To counter this effect, targets were heated during experiments. As seen in Fig. 4.2-4b, a surface temperature of 180 °C in the case of LiF and 60°C in the case of CaF_2 is sufficient to eliminate any macroscopic charging-up by the onset of ionic conductance leading to the restoration of the "original" electron yield. Between any two ion impact events (typically every ms) the surface can relax to a discharged state while it still behaves like an insulator during the impact of one individual ion (timescale typically 10 – 100 fs). It has to be added that the temperature necessary for elimination of the charge-up effect can vary quite significantly even for the same material. It certainly depends on the thickness of the sample and the quality of the electric contact. It has been observed that a good physical contact of a grounded clamp to the irradiated target surface is very beneficial. But even under these conditions, the charging may vary considerably from experiment to experiment. At the FZD, no charge-up was observed at all for the CaF_2 surface even at room temperature, which might also be due to the overall improved collection efficiency of the electron statistics setup there. LiF showed no charge up effects when heated to only 100°C in FZD, even for very high primary ion fluxes of more than 10^6 ions/sec.

A crucial point on measuring any electron yields from insulators with the electron statistics method is the determination of the necessary temperature to cancel the charge up completely. Even at room-temperature, the electron yield from LiF and CaF_2 will not drop to extremely low values. An equilibrium state will develop (e.g. 60 e^-/ion instead of 130 e^-/ion for CaF_2 in Fig. 4.2-4), which depends somewhat on the primary ion current and collection geometry. Such conditions, if unnoticed, can make a collected set of data completely unusable. A more detailed analysis of the charge-up phenomena during HCI irradiation can be found in the diploma thesis of Martin Simon [1].

4.2.3 Electron Emission at Moderate Impact Velocities

Very highly charged ions at very low impact velocities are still a very rare species, as they are extremely hard to produce. Up to the present day (2008), no facility in Europe can routinely produce these extreme projectiles. There are a few sources for very highly charged ions like the Heidelberg-EBIT (H-EBIT) that can produce and deliver e.g. Xe^{52+}, but they lack a deceleration beamline and typically work with beams of 5 – 10 keV/q. The Two-Source-Facility at the FZD has such a beamline that can decelerate ions to below 10 eV/q, but the EBIT there is much less powerful than the H-EBIT, limiting the projectile charge state for Xe ions to $q \leq 44+$. For this reason, I have first started to work on very highly charged ions in the mentioned keV/q energy per charge state regime, which are also less demanding in terms of the collection geometry. This chapter will report on results gained from such "moderately slow" ions.

4.2.3.1 Conducting Targets

For ions with kinetic energies well above the respective KE threshold [15], the total electron yield will result both from PE and KE, but the relative importance of the two contributions is difficult to assess. An unambiguous measurement of the PE yield is however possible under certain well-defined circumstances.

(a) For ions with kinetic energies well below the KE threshold (exclusive PE) [46];

(b) for slow ions in such high charge states that the potential energy greatly exceeds the kinetic energy (dominant PE) [60];

(c) for grazing incidence of fast HCI under the assumption that only the ion velocity component normal to the target surface ("vertical impact velocity") is relevant for PE [139].

So far, the validity of assumption (c) could only be demonstrated for ions with relatively low charge states up to Ar^{8+} [109]. I will now demonstrate that also for highly charged ions like Xe^{50+} assumption (c) remains valid by discussing the angular dependence of the PE yield for a clean Au(111) surface bombarded by slow very highly charged ions.

Total electron yields γ for Ar^{q+} (q = 11, 17) and Xe^{q+} ($26 \leq q \leq 50$) ions impinging with constant velocity v of 7×10^5 m/s (2.5 keV/amu) on a clean single crystal Au(111) surface are plotted in Fig. 4.2-5 versus the ion impact angle θ with respect to the target surface normal. First of all, the electron yield strongly increases with the charge state q of the incident ions, as clearly expected for PE [108, 140]. Secondly, for a given charge state q the yield increases with the projectile impact angle θ. The experimental data for Ar^{q+} and Xe^{q+} projectiles follow quite well an inverse square root of cos(θ)-dependence of the form

$$\gamma(\theta)_{v=const} = c_1 + \frac{c_2}{\sqrt{\cos(\theta)}} \qquad (14)$$

with c_1 and c_2 as free fit parameters. In earlier investigations for normal incident (θ= 0°) HCI on a polycrystalline Au surface, an empirical relationship for the velocity dependence of electron yields exclusively caused by PE has been found [46, 108, 140]

$$\gamma(v)_{\theta=0^\circ} = \frac{c}{\sqrt{v}} + \gamma_\infty \qquad (15)$$

c and γ_∞ are free fit parameters. Relationship (15) is well supported by COB modeling calculations [108, 141] and reflects the fact that the interaction time above the surface available for auto-ionization and slow electron emitting processes decreases with increasing projectile speed. The interaction path length is the distance between the point where the first electrons are captured and the target surface. We mention that within this picture the velocity independent part of the PE yield c corresponds to emission processes taking place at and shortly after the projectile ion has hit the surface. Then electrons still residing in highly excited Rydberg states of the hollow atom will be peeled off [35, 48, 108], and empty inner shells will be rapidly filled in the first monolayers of the surface, leading to the emission of a correspondingly large number of electrons. The number of slow electrons can well exceed the original ion charge state q, because of repeated HA decay and recapturing of electrons from the surface [108, 140, 141].

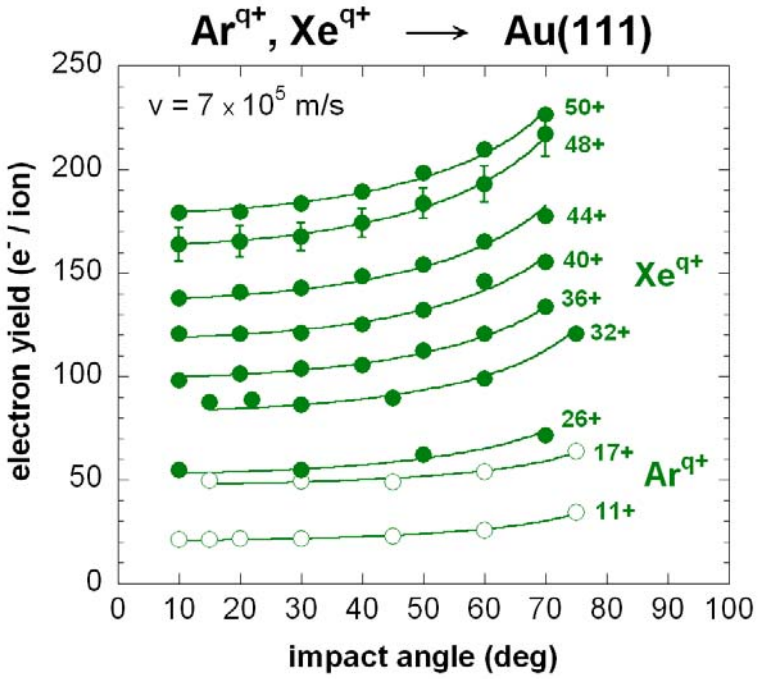

Fig. 4.2-5: Dependence of total electron yields γ (data points) vs. impact angle θ with respect to the surface normal for impact of highly charged Ar and Xe ions on a clean Au(111) surface. Impact velocity was fixed at $7 \cdot 10^5$ ms^{-1} for all charge states. The solid lines represent fits according to (14). Typical error bars are shown for q = 48. [13]

It is of interest to test whether the observed impact-angle dependence o-f the electron emission yields as shown in Fig. 4.2-5 is simply determined by the projectile velocity component normal to the surface:

$$v_\perp = v \cdot \cos(\theta) \qquad (16)$$

Impact-angle dependent measurements have therefore been performed as shown in Fig. 4.2-6 with Xe^{44+} projectile ions for 6 different impact energies varied from 2.2 keV/amu to 4.2 keV/amu. All measured Xe^{44+} data surprisingly well follow the relation

$$\gamma(v_\perp) = \frac{c}{\sqrt{v_\perp}} + \gamma_\infty \qquad (17)$$

which simply follows from Eqs. (14) - (16). They can be fitted with one single curve using a γ_∞ fit value of 79,5 e^-/ion. Results from all Xe^{44+} measurements are plotted together in Fig. 4.2-6 as a function of $v_\perp$, the projectile velocity component normal to the surface.

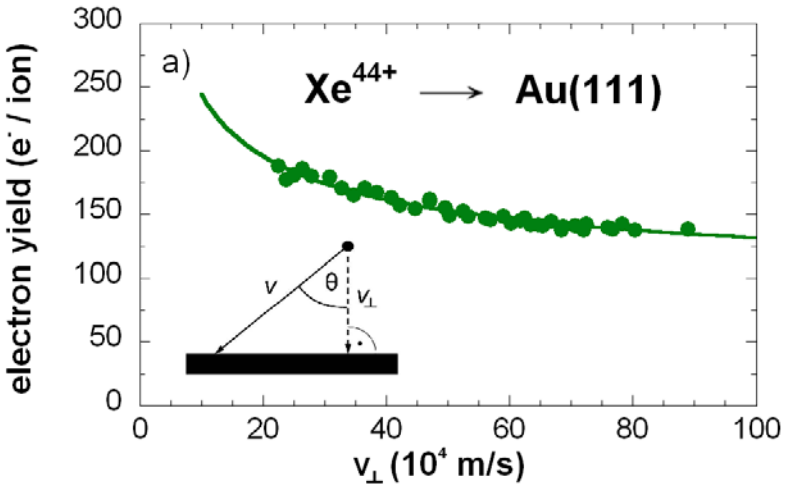

Fig. 4.2-6: Measured total electron yields ɣ (data points) vs. projectile velocity component normal to the surface $v_\perp$ for impact of Xe^{44+} on a clean Au(111) surface, measured at 6 different impact velocities (from 2.2 keV/amu to 4.2 keV/amu) and various impact angles in the range of 10° - 75°. The solid line represents a fit according to Equ. (17). [13]

KE has to be treated separately, since the present experiments have certainly been performed well above the respective KE thresholds of 6 x 10^4 m/s [111]. Unfortunately, no literature values for the KE yields for impact of neutral or singly charged Ar and Xe projectiles on Au are available for an impact velocity of 7 x 10^5 m/s. Eder et al. [111, 135] have measured KE yields for Ar^+ and Xe^+ at impact velocities of up to 4 x 10^5 m/s and 1.5 x 10^5 m/s, respectively, on polycrystalline Au. We extrapolated these KE yields according to data for Ar^+ and Xe^+ on polycrystalline Aluminum up to 8 x 10^5 m/s [142]. Based on this approximation, the relevant KE yields in the present experiments should remain well below 3 e^-/ion for both Ar and Xe ions. Since the measured total electron yields are much larger (50 – 200 e^-/ion), such relatively small KE contributions can be neglected and the electron yields presented here are definitely characteristic for potential electron emission. It is therefore proven that the here observed angular dependence of the PE yields directly reflects the variation of the velocity component normal to the target surface $v_\perp$ as predicted by formula (17). This implies that processes responsible for emission of slow (E_e < 50 eV) electrons are already completed in the first monolayers of the Au surface, whereas the number of electrons emitted after the penetration of the surface is almost independent of the projectile's velocity and impact angle, summarized into the contribution γ_∞ in (17). If there were a significant contribution to electron emission from deeper layers, their escape probability would depend on their depth of generation with respect to the mean free path of slow electrons in gold. One would then expect an inverse cosine dependence of this contribution on the impact angle of the ion, much like for the case of kinetic electron emission (see Chapter 2.3.1), but such a dependence was not observed in the

present experiments. So far, this had only been shown for charge states up to q = 8 [109], but now could be demonstrated also for much higher ion charge states up to q = 50.

4.2.3.2 Insulating Targets

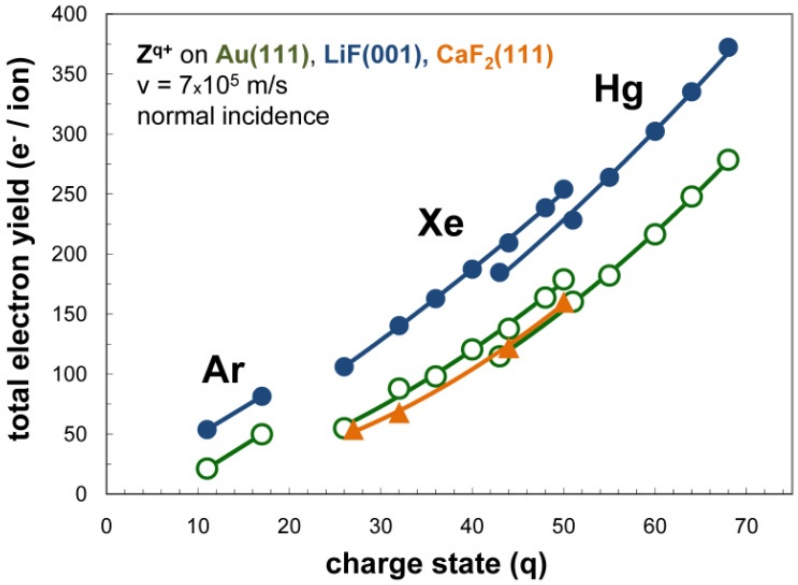

Fig. 4.2-7: Measured total electron emission yields for HCI impact on a conducting Au(111) (○) and on insulating LiF(001) (●) and CaF_2(111) (▲) single crystal surfaces. The projectiles' impact velocity was kept constant and impact angle was 0° (i.e. perpendicular to the surface). No saturation of the yields was observed for the insulators with increasing charge states. Fits (solid lines) are second order polynomials. [5]

Fig. 4.2-7 shows total electron yields from clean single crystalline LiF(001) and CaF_2(111) targets for normal incidence of highly charged Ar^{q+} ($q \leq 17$), Xe^{q+} ($q \leq 50$) and Hg^{q+} ($q \leq 68$) ions at a constant impact velocity of $7 \cdot 10^5$ ms^{-1}, compared to yields obtained for a clean conducting Au(111) surface. A clear dependence of the yield on the charge state of the incident ion is observed, as would be expected for the dominant potential emission process. Surprisingly, electron yields from the CaF_2 surface are comparable to that from the conducting gold surface, which has a considerably lower work function, while the total electron yields from the LiF surface are even higher than that. The yields show no saturation at higher charge states, which could be expected if one assumes that the impact zone is charged up microscopically. The extraction of electrons by the approaching HCI would then make the emission of additional electrons on a picosecond timescale more difficult.

Fig. 4.2-8 shows total electron yields from a freshly cleaved LiF surface for impact of highly charged Xe^{44+} ions as a function of the primary ion's impact angle and compares these results to electron yields from CaF_2 and Au targets. The dependence of electron yields from the insulators on the projectile impact angle cannot be fitted by eqn. (14), as do the yields from conducting target, but by an inverse cosine law:

$$\gamma(\theta) = \gamma_0 + \frac{\tilde{c}}{\cos(\theta)} \qquad (18)$$

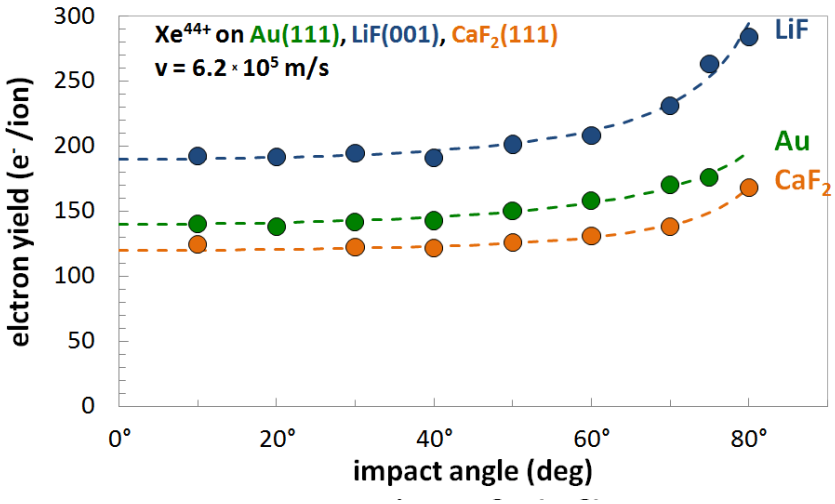

Fig. 4.2-8: Measured total electron yields for Xe^{44+} impact on Au, LiF and CaF_2 single crystals at a speed of $6.2 \cdot 10^5$ ms^{-1} under various impact angles. The slashed lines are fits to the data according to formula (14) for the conducting Au target and formula (18) for the insulating targets.

Total electron yields from insulating LiF surfaces have been measured for impact of Ar^{q+} ($q \leq 17$) and Xe^{q+} ($q \leq 50$) ions. While the impact velocity was kept constant for all charge states, impact angles were varied between 10° and 75° with respect to the surface normal. Kinetic electron emission (KE) yields for the present velocity regime of $7 \cdot 10^5$ ms^{-1} have been measured for normal impact of Ar^{q+} on LiF [113] as 25 electrons per ion, and should be somewhat higher for the heavier Xe ions. Still, this is up to an order of magnitude smaller than the total yields we have obtained. Kinetic emission yields are long known to vary with the incident ion's impact angle according to an inverse cosine law [143]. Indeed, the total electron yields obtained for the insulating targets can be well fitted by using eqn. (18) for all charge states, as seen in Fig. 4.2-9.

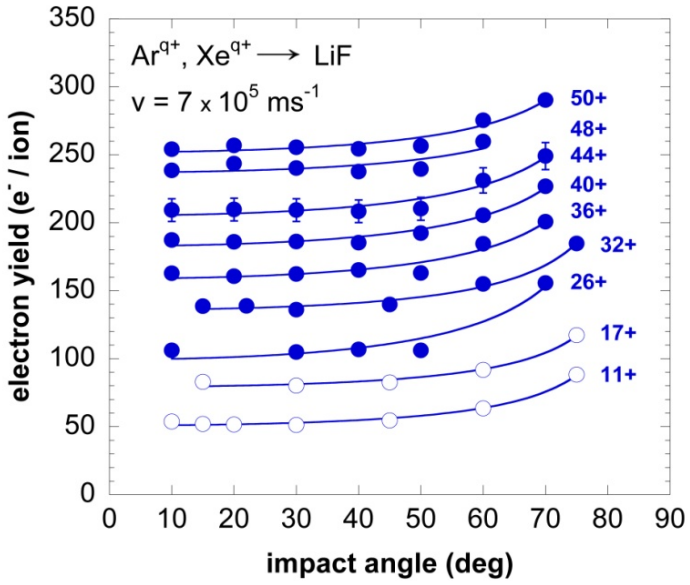

Fig. 4.2-9: Measured electron emission yields (data points) for impact of highly charged Ar^{q+} (○) and Xe^{q+} (●) ions on LiF(001) as a function of ion impact angle for constant impact velocity. Fits (solid lines) according to formula (18). Error bars are given for Xe^{44+} as an example. [5]

It is furthermore observed that the angular dependent part of the yield *c* is almost independent of the primary ionic charge state q, while the constant part γ_0 shows a very strong charge state dependence. On the other hand, the angular dependent part varies strongly with the projectile velocity. This lead to the conclusion that the angular dependence of the electron yields obtained for LiF is primarily due to KE. This conclusion is also supported by Fig. 4.2-10, which shows electron yields for Xe^{44+} impact at several impact velocities and under various impact angles as a function of the normal component of the impact velocity.

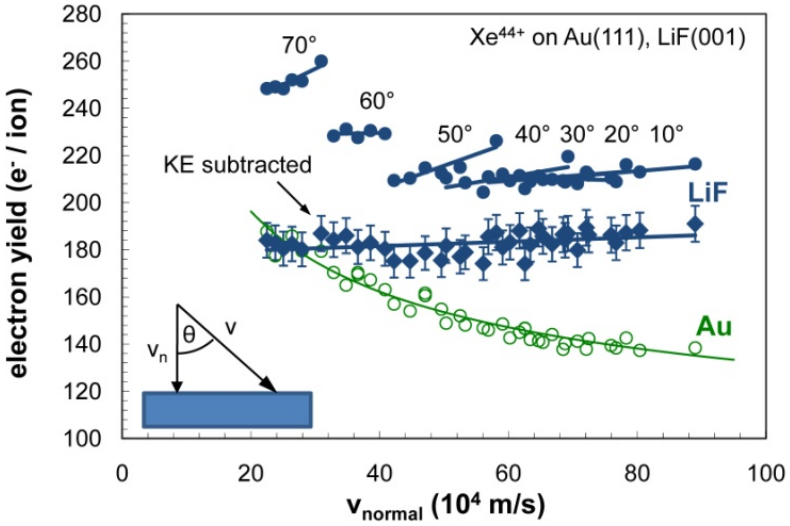

Fig. 4.2-10: All measured electron yields for Xe^{44+} impact on LiF for various impact angles (10° - 70°) and impact velocities (from 2.2 keV/amu to 4.2 keV/amu) as a function of the velocity component normal to the surface. Opposite to the case of a conducting Au surface (○) [18], the data points for LiF (●) are only aligned when measured at the same impact angle (connected by linear fits). After subtraction of the relevant kinetic electron emission contributions (c.f. text), all data points (♦) end up on a single curve, which shows a very weak dependence on the impact velocity. Due to the uncertainties in the subtraction procedure, error bars for the corrected yields are larger. [5]

The previous chapter showed that for a gold target and pure PE yields all data points obtained for a given charge state can be fitted with a single curve[12]. Yet for the insulating LiF target, this procedure does not work at all. If, however, we assume that the angular dependence is mostly due to KE and therefore dependent on the impact velocity *v*, the parameter $\tilde{c}$ in formula (18) can be fitted by a linear regression vs. *v*. We can then subtract this KE contribution from each of the total electron yields obtained according to an inverse cosine law. The remaining PE data points can then be fitted by a single curve (see Fig. 4.2-10) and are almost independent of the impact velocity. This is in strong contrast to the case of the conducting Au surface where a decrease of the PE yield with increasing velocity was found [12, 140]

$$\gamma_{PE}(v,\theta) = \gamma_{\infty} + \frac{c}{\sqrt{v\cos(\theta)}} \qquad (19)$$

A more direct way to eliminate any contribution of KE in our total yields is looking at the difference between yields obtained for two charge states at the same impact velocity. Fig. 4.2-11a shows results obtained for Xe^{51+} and Xe^{13+} at the same impact velocity of $4.5 \cdot 10^5$ ms^{-1}, and the difference between them. The subtraction of Xe^{13+} yields from the Xe^{51+} results undesirably

eliminates a part of the PE yield (although the potential energy of Xe^{13+} is only 1.6 keV, compared to 111 keV for Xe^{51+}), so the remaining yield is just the "excess" PE yield of Xe^{51+} as compared to Xe^{13+} on CaF_2. The contribution from KE, however, is fully eliminated as it only depends on the primary impact velocity of the ion. Image charge acceleration is negligible compared to the primary kinetic energy of more than 100 keV as it would amount to less than 500 eV even for Xe^{50+} impact on a conducting surface [46]. The remaining yield thereby qualitatively represents pure PE. As can be seen in Fig. 4.2-11b, these "excess" PE yields do not (or only very weakly) depend on the impact angle of the primary ion, both for LiF and for CaF_2 targets and for different projectile charge states. These results support the conclusions drawn from Xe^{44+} results (see Fig. 4.2-10) that the PE yields for these insulating targets do not strongly depend on the impact angle or on the component of the impact velocity normal to the surface, as in the case of a metal surface. For the CaF_2 surface, and also for the LiF surface at higher impact velocities, a slight decrease of the electron yield is observed with increasing impact angle.

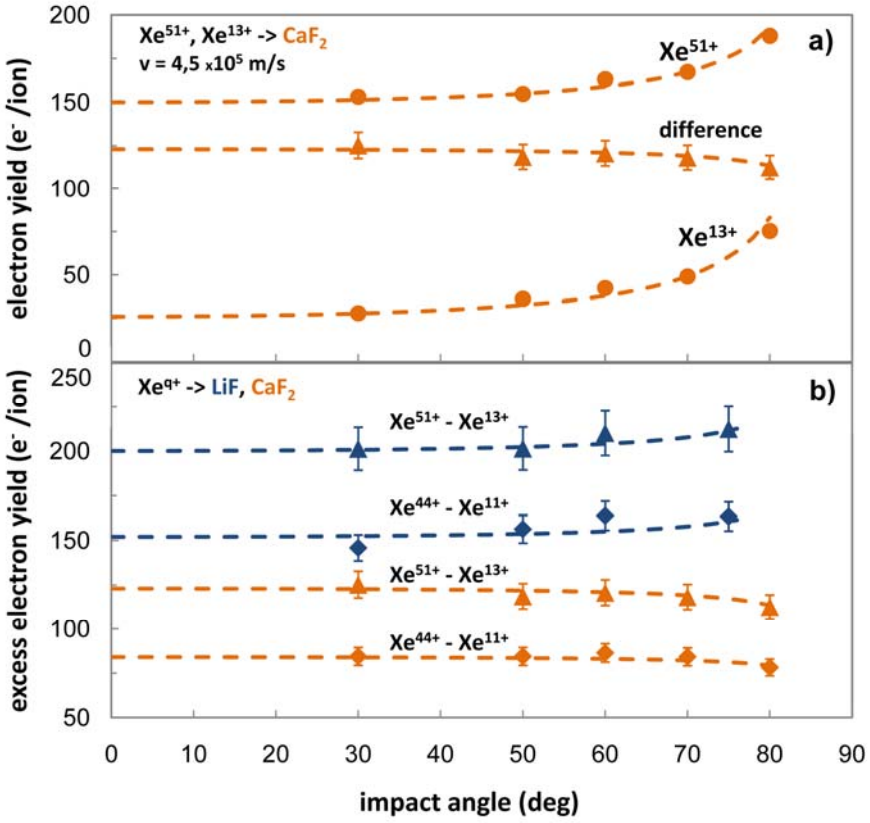

Fig. 4.2-11 (a): Subtraction of Xe^{13+} yields from Xe^{51+} yields measured at the same impact velocity cancels out any contribution of kinetic electron emission, showing the qualitative impact-angle dependence of pure potential emission from insulators.
(b) The remaining excess PE yields show a very weak dependence on the projectile angle of impact for both LiF and CaF_2 targets and various charge states. [5]

4.2.3.3 Above and Below Surface Electron Emission

The results presented in the previous chapter not only demonstrate the surprisingly large values of total and also purely potential electron emission yields for insulating targets, but also show drastic differences in the dependence of the PE yields on impact angle when compared to a conducting surface. To explore the reason behind these differences, Monte Carlo simulations based on the

classical-over-the-barrier (COB) model [35] modified for insulators [50] were performed to study potential electron emission during the approach of the ion to the surface. For insulating targets, the electron capture probabilities depend on the history of the impact process (local charges) and on the position of the HCI with respect to the lattice, so these simulations proved to be much more demanding than similar calculations for conducting surfaces. These simulations were hence performed only for the comparatively simple case of Ar^{11+} and Ar^{17+} colliding with a LiF and a Au surface. The calculations clearly show that the above surface part of the electron emission process, which is responsible for a large fraction of the total electron yield for conducting Au surfaces [12, 140], plays a much less important role for insulators. While the measurements yield a (potential) electron emission of 38 e^-/ion for Ar^{11+} and 66 e^-/ion for Ar^{17+} impact on LiF, the simulation of the above-surface part results only in 3.5 and 9.0 e^-/ion, respectively. Due to the increased binding energy of valence electrons in LiF (12 eV) compared to those of the conduction band in gold (5 eV), the hollow atom (HA) above a LiF surface is formed at a smaller distance and much less time is available for any deexcitation processes above the surface (see Fig. 4.2-12). Potential electron emission is therefore dominated by sub-surface emission processes, at least for the present velocity regime.

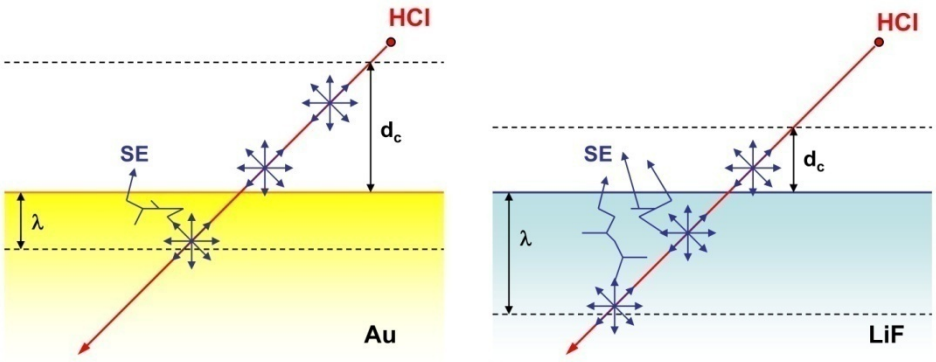

Fig. 4.2-12: Differences in potential electron emission between insulators (LiF and CaF_2) and metal surfaces (Au) arise from [5]
(i) different critical distances d_c for resonant neutralization of the HCI in front of the surface (different binding energy and dielectric response)
(ii) different escape depth λ for electrons emitted below the surface
(iii) different number of secondary electrons SE produced by primary Auger electrons

Every (Auger) electron produced inside the target undergoes elastic and inelastic scattering events, thereby initiating a secondary electron cascade. As a first step towards a quantitative understanding of the electron yield differences for LiF and Au targets, electron transport in LiF and Au were studied. The number of secondary electrons emitted into vacuum per primary electron created inside the solid at a certain depth were calculated using a Monte Carlo electron transport code [144]. Fig. 4.2-13 compares the secondary electron yields for Au and LiF surfaces and different primary electron energies as a function of the depth at which the primary electron is created. Due to a larger inelastic mean free path in LiF than in Au, a larger fraction of secondary electrons can escape from a LiF surface. With increasing depth z of the primary (Auger) electron, the ratio of the number of electrons emitted from LiF compared to Au increases reaching values larger than two. Although sub-surface potential emission is so far not included in the simulation of total electron yields, the number of Auger electrons generated by the deexitation of the hollow atom can be expected to be similar in both targets, while secondary electron emission is substantially more efficient for LiF

targets. For charge states q ≤ 17, this enhancement factor appears to account for most of the increased yield from LiF compared to Au (see Fig. 4.2-7)

The surprisingly high electron yields from the insulating LiF surface therefore are caused by (c.f. Fig. 4.2-12):

- The delayed electron capture and deexitation leaving more potential energy stored in the HA at the time of impact on the surface and
- the sub-surface decay via Auger emission leading to primary and secondary electrons which have a higher chance of escaping the surface due to the larger mean free path (much in the same way as kinetic energy deposited in insulators leads to higher KE yields as compared to the conducting targets).

Auger decay of the HA formed inside the solid after surface penetration will be completed within a few nanometers [7, 145], which in the case of LiF and CaF_2 is comparable to the mean escape depth λ of the produced electrons. This explains why the sub-surface PE yield for LiF does only slightly change with impact angle or impact velocity. For increasing impact angles (at constant impact velocity) the time spent by the projectile between the first electron capture and its impact increases and thus also the above surface part of the potential electron emission gets larger. This, however, leads to the emission of fewer (but more energetic) electrons with a reduced probability for electron multiplication below the surface (in about 50% of the cases their trajectories are completely outside of the solid). Together with an increased probability for projectile reflection, a reduction of the PE electron yield at grazing impact angles is therefore at least qualitatively plausible.

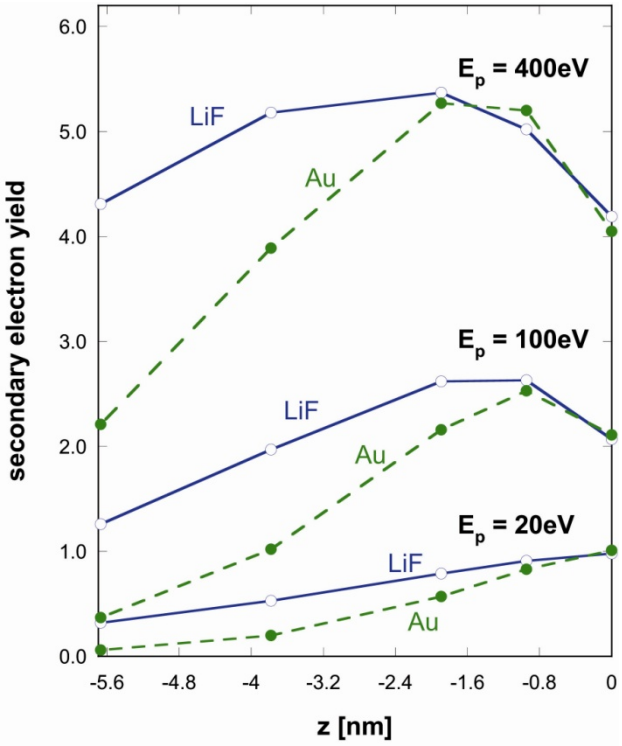

Fig. 4.2-13: Calculated secondary electron yields for primary electrons generated with different energies at a certain depth z beneath the surface (z = 0) of a conducting Au(111) and an insulating LiF(001) surface. Due to the increased inelastic mean free path especially for slow electrons in the insulator, secondary electrons have a much better chance to escape into vacuum. [5]

4.2.4 Electron Emission at Very Low Impact Velocity

One of the main goals of this work was to obtain electron emission yields for highly charged ion impact on insulators at very low impact velocities, approaching and even breaking the image charge acceleration barrier. This was done to test the predictions of Briand et al. [39] that the approaching highly charged ion can be reflected by the Coulomb repulsion of the positive charge patch forming on the surface during the interaction ("trampoline effect", see chapter 2.1.2).

This chapter presents electron yields for highly charged Xe^{q+} ions with charge states up to q = 44+ impinging with close to zero kinetic energy on an insulating LiF(001) surface and compares these results to yields obtained for a conducting gold surface. The electron yields obtained in this chapter were measured using an electron statistics setup (see chapter 4.1.1) of the "curtain type" electron collection geometry (see chapter 4.1.3.4). Since the geometry of the setup changes with decreasing projectile impact energies, a test of the reliability of the setup is presented prior to the main results. A brief discussion of the results and possible explanation for the observed velocity dependence of the yields follows.

4.2.4.1 Reliability of the Setup

As has been shown earlier, the "curtain type" electron collection geometry (see chapter 4.1.3.4) is superior in collection efficiency to the so called "fountain type". Another advantage of the present setup is that it allows for a bigger target holder, which allows heating of the target during measurements, which is necessary to cancel macroscopic charge-up of insulating targets during measurement (see chapter 4.2.2). A major drawback, on the other side, is that the collection geometry has to be changed when decelerating the beam, as the ion beam is deflected by the electron collector grid. As the amount of deviation of the beam depends on its kinetic energy with respect to the applied grid voltage, the target has to be moved for slower beams to ensure impact of the ions, thus probably changing the collection efficiency. Electron yields obtained by the cylindrically symmetric "fountain type" geometry do not have this problem and are therefore more reliable in giving the qualitative velocity dependence of the electron yield.

Fig. 4.2-14 a) compares electron yields obtained with the present setup for impact of Xe^{40+} on a gold surface to measurements using the "fountain type" geometry. As the collection efficiency of the present setup is higher, the previously measured yields had to be corrected using a global scaling factor *f = 1.3* to match our yields in the high velocity regime, where the electron collection efficiency of the present setup is known to be close to 100%. A fit according to the classical over-the-barrier-model including image charge acceleration and kinetic electron emission is plotted through the Kurz et al. [140] data according to

$$\gamma(v) = \frac{c_{vel}}{\sqrt{v_{eff}}} + \gamma_{\infty} + c_{KE} \cdot \left(v_{eff} - v_{th}\right) \cdot \Theta\left(v_{eff} - v_{th}\right) \qquad (20)$$

with the effective velocity

$$v_{eff} = \sqrt{\frac{2q}{m}\left(U_{source} + U_{image}\right)} \qquad (21)$$

derived from the source potential and the image charge potential.

Fit parameters c_{KE} and the threshold velocity v_{th} for kinetic emission in the fit presented in Fig. 4.2-14 using formula (20) are taken from Xe^{+} impact on gold [111]. Fig. 4.2-14 b) compares the present yields to the fit in a). Down to $3.4 \cdot 10^4$ ms^{-1} or 10 eV/q, no systematic deviation is found, whereas below this energy a correction of the present yields of up to 10% becomes necessary. All subsequently presented electron yields below 10 eV/q are corrected using the dashed line fit to the data points in Fig. 4.2-14 b).

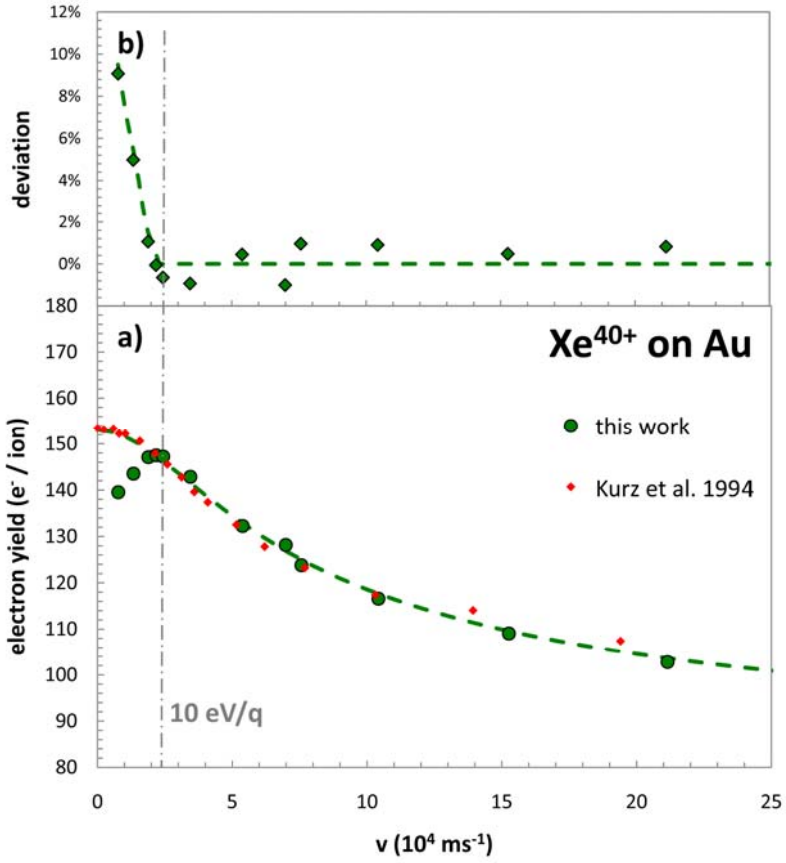

Fig. 4.2-14: a) Electron yields of Xe^{40+} ions impinging on a gold surface as a function of the ion's impact velocity obtained with the new ‚curtain type' setup are compared to previous results from Kurz et al. [140]. Those yields were scaled up by 30% to correct for their insufficient electron collection. The dashed line is a classical-over-the-barrier fit of the data.
b) The deviation of the present data points to the COB fit shows satisfactory collection for velocities down to 2.4 10^4 ms^{-1} (10 eV/q). The dashed line is a fit to the deviation which is then used as a general correction to all electron yields obtained by the new setup.

For the measurement of electron yields at very low velocities with the present setup, two methods of beam deceleration were used. Down to kinetic energies of 20 eV/q, the ion beam was slowed down from its original 4.5 keV/q using the deceleration lens of the beam line at FZD and entered the experimental chamber with its final velocity. Below these energies, the beam will either be too strongly deflected by the applied electron collection potentials (see also chapter 4.1.3.2), or the potentials have to be chosen too low to ensure sufficient collection efficiency. Therefore, the lowest impact energies were realized with a 20 eV/q beam entering the chamber where the beam was decelerated further to its final velocity directly at the target, which was biased up to 20 V or more. This deceleration with the biased target is responsible for the non-perfect collection efficiency below 10 eV/q that can be seen in Fig. 4.2-14 b).

To make sure the collection efficiency correction is accurate, a test was performed where the target was biased decelerating a 30 eV/q beam, and the results were compared to those from the 20 eV/q beam in Fig. 4.2-15 a). The two curves do not match, confirming the need of correction factors for extremely low velocities. The process of biasing the target to decelerate the beam is thought to be responsible for the non-perfect collection efficiency, as this process changes all electron collection potentials relative to the target. Thus, yields obtained from the decelerated 30 eV/q beam have to be corrected by taking into account the bias voltage of the target, not the final energy of the beam. Applied correction factors taken from Fig. 4.2-14 b) are shown in Table 4.2-1. No significant difference between the two curves in Fig. 4.2-15 b) can be observed after the relevant correction factors have been applied.

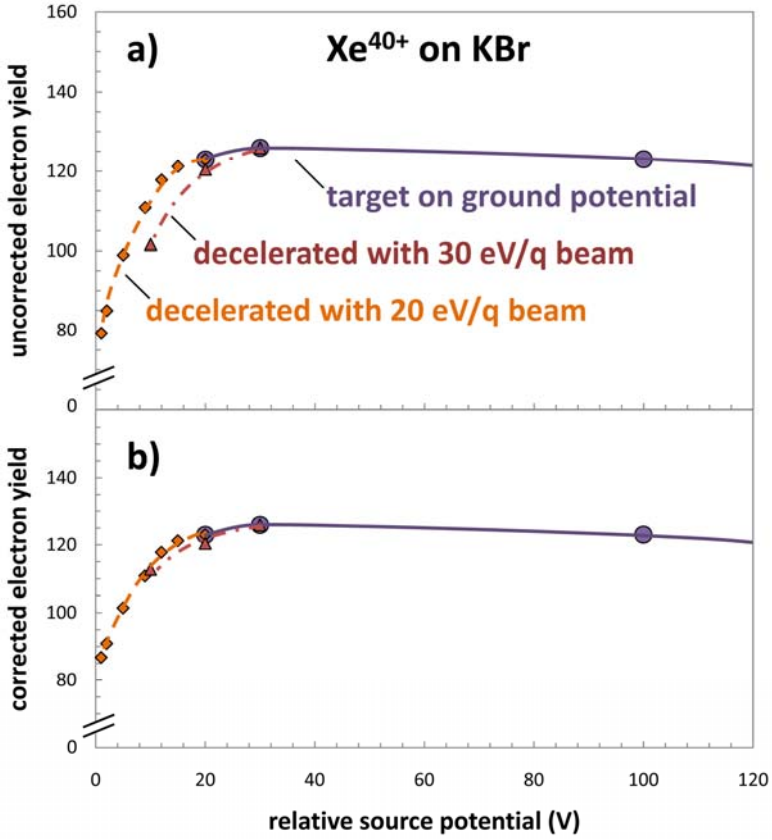

Fig. 4.2-15: Electron yields for Xe^{40+} impact on a KBr surface without any correction for collection efficiency are presented in a) as a function of the relative potential between target surface and the ion source. For beam potentials of above 20 V, the target was kept on ground potential (circles). Below 20 V, the target was biased to decelerate the beam further (diamonds). To verify the influence of target biasing on electron collection efficiency, electron yields were also measured for target biasing starting at 30 V (triangles). b) After application of the relevant correction factors from Table 4.2-1, the two curves coincide within tolerance of experimental errors.

Apart from the necessary electron collection efficiency correction presented above, it is important to correctly determine the true source potential of the beam. As yields were measured for impact energies as low as virtually 0 eV/q, any error of even a few Volts in the nominal source potential creates a large error on the velocity axis. Fig. 4.2-16 shows how at very low nominal source potential, a part of the beam is reflected and does not hit the target anymore. Due to the non-zero energy spread of the beam, those ions do not have enough energy to reach the biased target anymore. This fraction is plotted in Fig. 4.2-17 vs. the nominal source potential to derive the true

source potential and the energy spread of the beam for the three targets used in this study. When the target is exactly at source potential, 50% of the beam is reflected, while the standard deviation of the energy spread can be gathered from the fitted curves. As the targets were measured subsequently on different days, the ion source parameters were not always exactly the same and lead to the different observed values.

Table 4.2-1: Correction factors for a given target bias as determined in Fig. 4.2-14. The relative source potentials as seen in Fig. 4.2-15 are shown for the 20 and 30 eV/q beam respectively.

target bias (V)	20 eV/q beam, rel. source pot. (V)	30 eV/q beam, rel. source pot. (V)	correction factor
0	20	30	0%
10	10	20	0%
12	8		0,5%
14	6		1,5%
16	4		4%
18	2		7%
20	0	10	11%

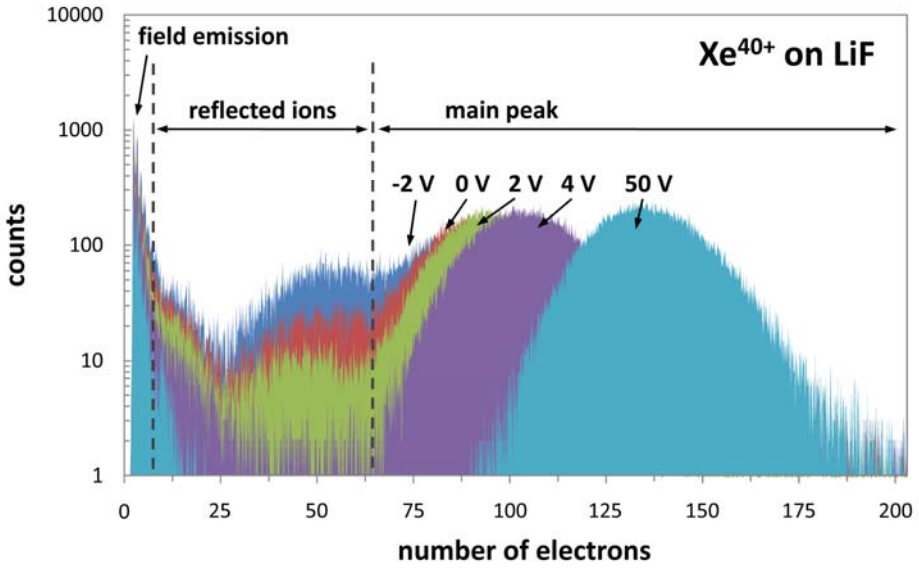

Fig. 4.2-16: Raw electron statistics spectra taken for Xe^{40+} impact on LiF(001) for various nominal source potentials. Ions hitting the target contribute to the 'main peak' region. With decreasing potential difference, some of the ions are reflected in front of the target due to the non-zero energy spread of the beam. These ions then hit some other part of the target chamber where the collection efficiency is low, thus contributing to the region left of the main peak. The region on the very left side of the spectrum contains mostly events of field emission and electrons from the beam line.

Thus it has been shown that

- the "curtain type" electron collection geometry can provide reliable yields down to impact energies as low as 10 eV/q and that a correction function can be applied to yields measured at lower energies
- the true source potential of the ion beam as well as the energy spread was determined during the experiments.

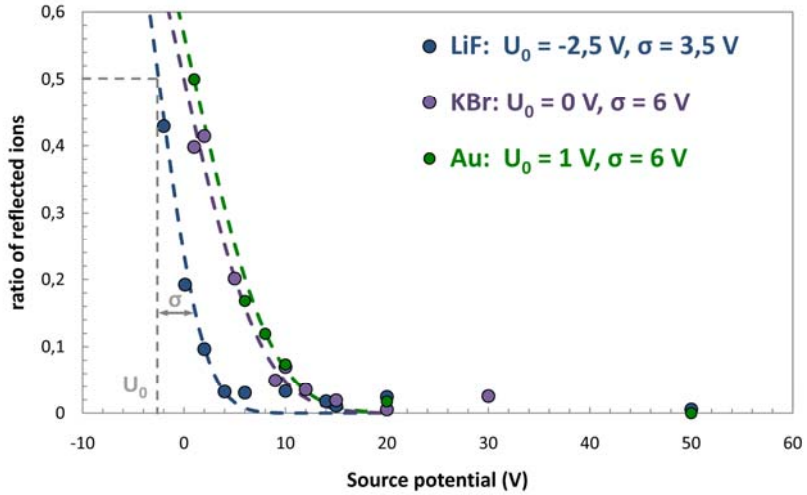

Fig. 4.2-17: For Xe^{40+} impact on gold, LiF and KBr single crystals the rate of reflected ions with respect to the total beam is plotted vs. the nominal potential difference between ion source and target (data points). The dashed lines are integral Gauss function fits to the data. The data have been evaluated with respect to the true potential difference between source and target and the energy spread of the beam (given by its standard deviation σ)

4.2.4.2 Electron yields

Fig. 4.2-18 shows electron emission yields measured for Xe^{40+} impact on insulating LiF and KBr single crystals compared to a conducting gold surface. The impact velocities range from an almost totally stopped beam (E_{kin} < 1 eV/q) up to $7.4 \cdot 10^5$ ms^{-1} (9.3 keV/q). The results from the gold surface can be nicely fitted by formula (20), as shown in the previous chapter.

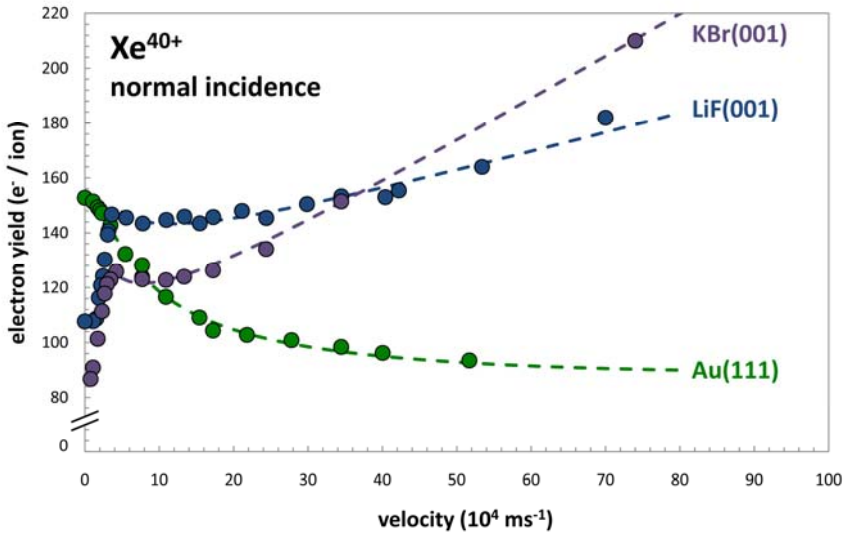

Fig. 4.2-18: Total electron yields for impact of Xe^{40+} ions on gold, LiF and KBr single crystals under close to normal incidence (data points). The dashed lines represent fits according to formula (20).

Surprisingly, yields above 10 eV/q (3.4 ms^{-1}) from the insulating surface can be fitted using the same formula, although then the kinetic emission and the velocity independent part of potential emission γ_∞ become dominant. KBr shows the smallest electron yields in the low velocity regime,

but the highest yields above $4 \cdot 10^5$ ms^{-1}, which is attributed to a large contribution from kinetic electron emission. The data shown in this plot originate from different measuring campaigns at both the EBIT at FZD (up to $4 \cdot 10^5$ ms^{-1}) and the Heidelberg EBIT (higher velocities). Note that the drastic drop of electron yield at very low impact velocities cannot be attributed to collection efficiency loss due to the biased target, as has been shown in Fig. 4.2-15.

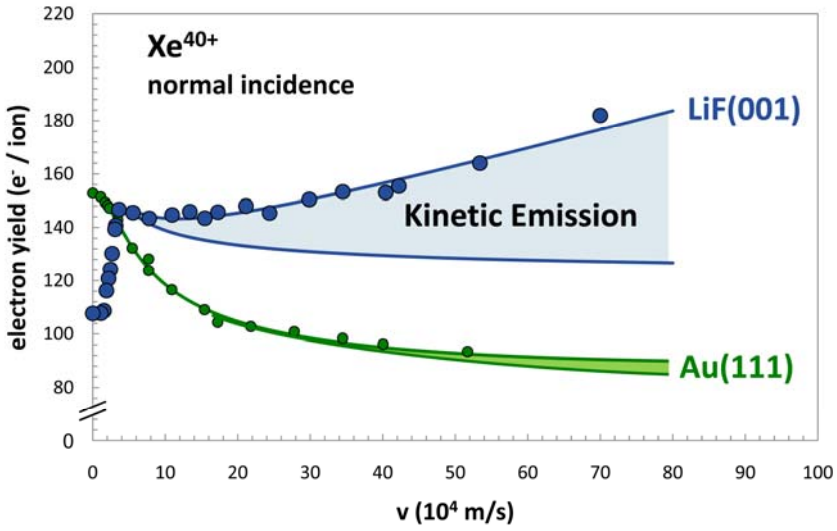

Fig. 4.2-19: The influence of kinetic electron emission on the measured total electron yields (circles) in Fig. 4.2-18 has been estimated using data from Vana [113]. The resulting potential electron emission yields for insulating LiF target (diamonds) are well fitted by the COB model above $4 \cdot 10^4$ ms^{-1}. Below this velocity, a rapid drop of the yield is observed.

To analyze potential electron emission on insulating targets, it is necessary to estimate the influence of kinetic electron emission on the measured total electron yields. Unfortunately, there is no available data on kinetic electron emission yields for Xe on LiF, but data from Ar^{q+} impact on LiF [113] can be used as a lower limit estimate [1]. Fig. 4.2-19 shows the velocity dependence of electron yields for Xe^{40+} impact on LiF after subtraction of the kinetic emission contribution. Starting at the highest measured velocities, potential electron yields on the insulating material increase with decreasing velocity; similar to conducting targets. However, the increase is much less pronounced and stops at approximately $3.5 \cdot 10^4$ ms^{-1}. It should be mentioned that kinetic electron emission from Ar, although similar to Xe at the same velocity, is just a lower bound to real KE yields from the heavier Xe species. Therefore, the observed increase of PE with decreasing velocity might be somewhat steeper than shown, but cannot be less steep or even a decrease. Below $3.5 \cdot 10^4$ ms^{-1}, a sharp drop in the electron yield of LiF with decreasing projectile velocity is observed.

To further explore the lowest velocity regime, the data from the previous figure (after subtraction of kinetic electron emission for LiF) have been plotted vs. the inverse velocity in Fig. 4.2-20. As suggested by Kurz et al. [140], the image charge acceleration for gold is determined by the crossing point of a COB theory fit (see eqn. (15) on page 70) for higher velocities and a constant "saturation" value for lowest velocities. Since no physically reasonable fit for the velocity dependence of electron yields on LiF can be made at this point, the image charge acceleration for the insulating material is estimated as the first distinct kink from the flat line at very low velocities (high inverse velocities). This estimation of 160 eV seems reasonable compared to the conducting target at first glance, since image charge acceleration should scale with

$$U_{image} \propto \frac{\varepsilon - 1}{\varepsilon + 1} \qquad (22)$$

for the permittivity ε. As even at the image charge acceleration limit the highly charged ion is approaching the surface with relatively high velocity (and thereby frequencies of the electrical field), the dynamic and not the static permittivity value has to be taken into account. The "optical limit" of ε is considered a reasonable value for the approach of slow HCI towards a surface. For LiF it amounts to about 1.9 [114], leading to an expected U_{image} of 143 V. This coincidence might nevertheless be fortuitous, as a small error in the energy resolution of our system or even in the measured electron yields will have a considerable impact on this value.

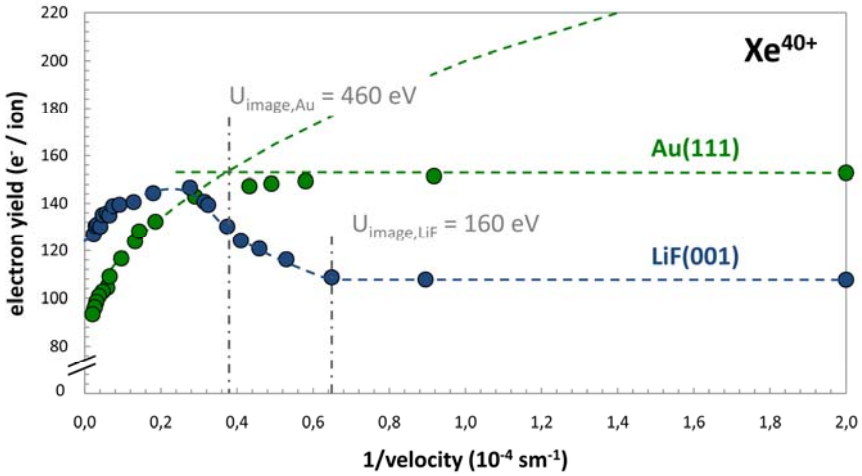

Fig. 4.2-20: Data from Fig. 4.2-19 (where kinetic emission has been subtracted from the LiF yields) are plotted versus the inverse velocity to evaluate the influence of image charge acceleration as suggested by Kurz et al. [140] (c.f. text). For the LiF target, the first deviation from the saturation region at low velocities (high inverse velocities) is used to estimate image charge acceleration to 160 eV.

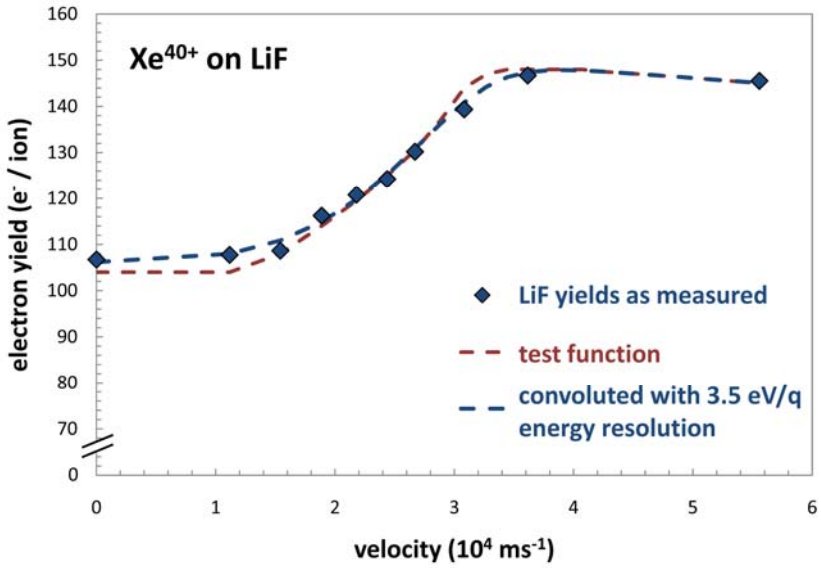

Fig. 4.2-21: To estimate the effect of the non-zero energy spread of the beam on the measured yields, a test function has been convoluted with a Gaussian energy spread of 3.5 eV, as extracted from Fig. 4.2-17.

Since the energy distribution of the incident beam that was used for the LiF irradiation has been measured to be 3.5 eV/q and electron yields were measured down to 1 eV/q, the energy spread of the beam cannot be neglected for the lowest impact energies. An attempt to deconvolve the energy spread from the present results was made. An analytical approach is difficult to pursue, since the part of the beam which has nominally negative impact energies is reflected before it interacts with the target and does not contribute to electron yields at all. Fig. 4.2-21 shows the result of an "empirical" deconvolution of the measured yields, by convoluting an arbitrary test function with the measured energy spread and trying to get the best overlap of the convoluted function with the measured yields. As can be expected, the slope of the electron yield drop in the low velocity regime of the test function is steeper than the measured yields suggest, albeit not very dramatically. Both kinks (at around $1.5 \cdot 10^4$ ms^{-1} and $3.5 \cdot 10^4$ ms^{-1}) in the test function are shifted to lower velocities, adding to the uncertainty in the observed image charge acceleration for LiF.

The electron statistics detector is a unique tool for electron emission analysis, as it is not only capable of measuring the mean electron yield, but also the statistical distribution of electrons emitted for every ion impact (see Chapter 4.1.1). Thus, the standard deviation of the emission statistics becomes accessible, which is not possible using any current measurement techniques. Standard deviations of measured electron statistics spectra are shown in Fig. 4.2-22 for Xe^{40+} impact on Au and LiF as a function of the impact velocity. The standard deviation was normalized to the square root of measured yields γ according to

$$\sigma' = \frac{\sigma}{\sqrt{\gamma}} \qquad (23)$$

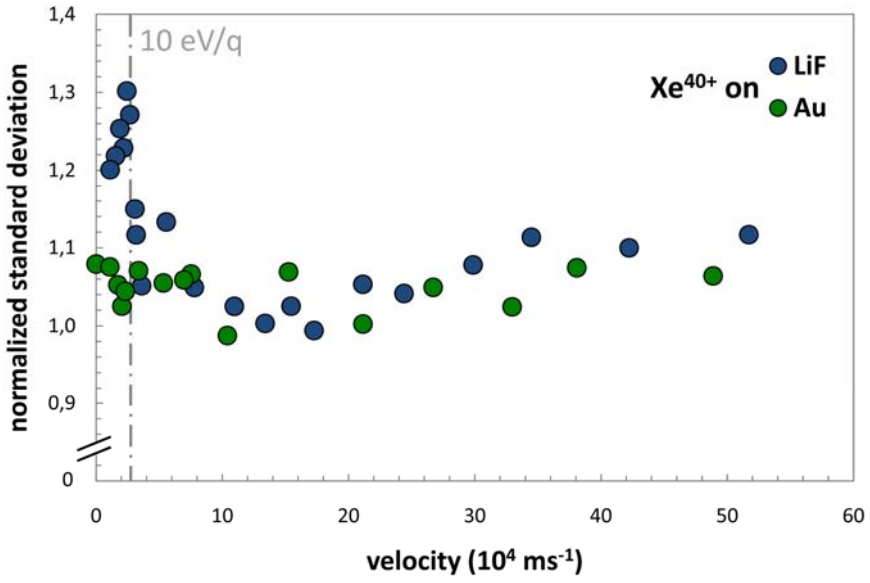

Fig. 4.2-22: The standard deviation of measured electron emission statistics spectra normalized to the square root of respective electron yield (see eqn. (23)) is plotted vs. the impact velocity of the approaching Xe^{40+} ion for impact on gold and LiF. The normalized standard deviation of the two targets is very similar at higher velocities, but a distinct structure is visible for the insulating target at around 10 eV/q.

Although the data points do scatter considerably, both targets show very similar normalized standard deviations of about $\sigma' = 1.05$ in the velocity regime above $7 \cdot 10^4$ ms^{-1}. Below this value,

peaking at around $2.4 \cdot 10^4$ ms^{-1} (10 eV/q), a distinct increase in the standard deviation of LiF clearly deviated from the behavior found for the Au target. Interestingly, this is the velocity region where the sharp drop of electron yields for the insulators was observed.

In addition to Xe^{40+}, charge states q = 20+ and 30+ were investigated in terms of velocity dependence. In fact, in the beginning of the investigations a number of charge state and velocity series between 15+ and 44+ as well as from 1 keV up to 60 keV kinetic energy were measured. However, as reliable measurement conditions for the very low velocity regime have only been found relatively late during the course of this work, only the three mentioned charge states can be considered for a detailed analysis.

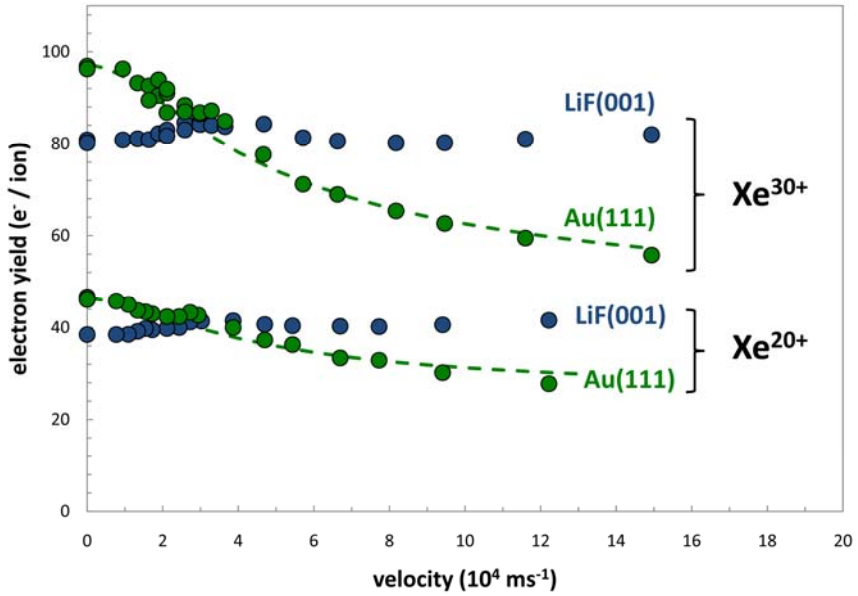

Fig. 4.2-23: Electron yields from Xe^{20+} and Xe^{30+} impact on single crystalline gold and LiF targets as a function of the impact velocity. Note the different scale on the velocity axis when comparing these results to Fig. 4.2-19.

Fig. 4.2-23 shows the velocity dependence of Xe^{20+} and Xe^{30+} impact on Au and LiF surfaces up to $15 \cdot 10^4$ ms^{-1}. Qualitatively, a similar behavior to the case of Xe^{40+} impact is observed. The electron yields of the insulator are larger than those from the conducting gold target in the high velocity regime. Between 2 and $4 \cdot 10^4$ ms^{-1}, a drop of the electron yields below those from gold is observed. Quantitatively, however, this drop is by far less pronounced as for the higher charge state, as it amounts to less than 10% of the maximum yields, while a drop of more than 25% was observed for q = 40+.

To better compare the magnitude of the electron yield drop at very low velocities, Fig. 4.2-24 shows electron yields for different charge states measured at constant impact velocity. At $5 \cdot 10^4$ ms^{-1}, just above the velocity of the yield drop, the charge state dependence of electron yields shows no qualitative difference between the conducting and the insulating target. Yields from both targets increase steadily with the charge state of the projectile ion. This is very similar to the behavior found for moderately slow projectile ions of up to a few hundred keV kinetic energy (c.f. Chapter 4.2.3.2), where it was interpreted as a significant contribution of below surface electron emission for the case of the insulator. At an extremely low velocity of $1 \cdot 10^4$ ms^{-1}, however, yields from the insulating LiF surface differ significantly from the conducting Au target. Both curves run parallel between charge

states 20+ and 30+, while a clear indication is found for a saturation of the yields from the insulator at the highest charge state of 40+. It becomes evident that a significant drop of the electron yield from the LiF target with respect to the yields from the conducting gold target is only found for high charge states and extremely low velocities.

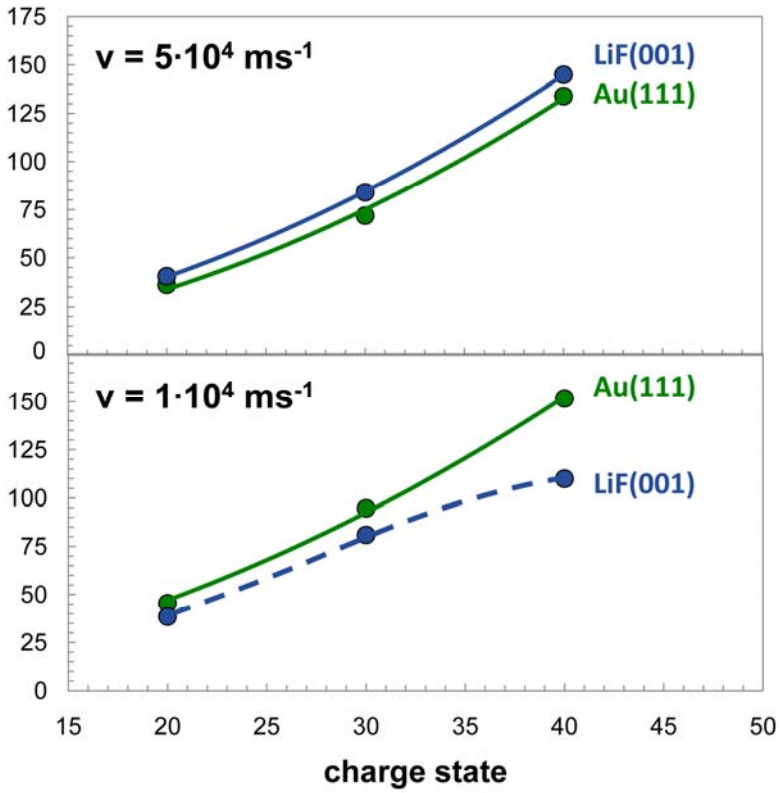

Fig. 4.2-24: Total electron yields for Xe^{q+} impact on Au and LiF targets are plotted as a function of the incident ion's charge state for two different velocities. At $1 \cdot 10^4$ ms^{-1}, the electron yields from the insulator saturate at charge states higher than 30+.

4.2.4.3 Interpretation

The previous chapter showed two main results from the experiments with very slow HCI impact on insulator surfaces:

- The electron yields for HCI impact on insulator surfaces drops significantly at very low impact velocities as compared to a conducting surface
- The magnitude of the drop in electron yields is strongly dependent on the charge state of the ion

While it was not possible during this work to provide a conclusive answer as to the physical reasons for this behavior, this chapter discusses possible explanations and an outlook for future work on this topic.

When considering the drop in electron yields, it has to be considered that the yields from the insulator at higher velocities are in fact surprisingly high taking into account the high binding energy of electrons in this material. Using the COB model to estimate electron yields, one would expect much lower yields from the LiF surface where the binding energy is more than 14 eV as compared to

a gold surface whose electrons can be extracted at an expense of ca. 5 eV. Chapter 4.2.3.3 introduced a strong sub-surface electron emission contribution for the insulating materials to explain these findings (see Fig. 4.2-25), as sub-surface electron emission is not covered by the conventional COB model.

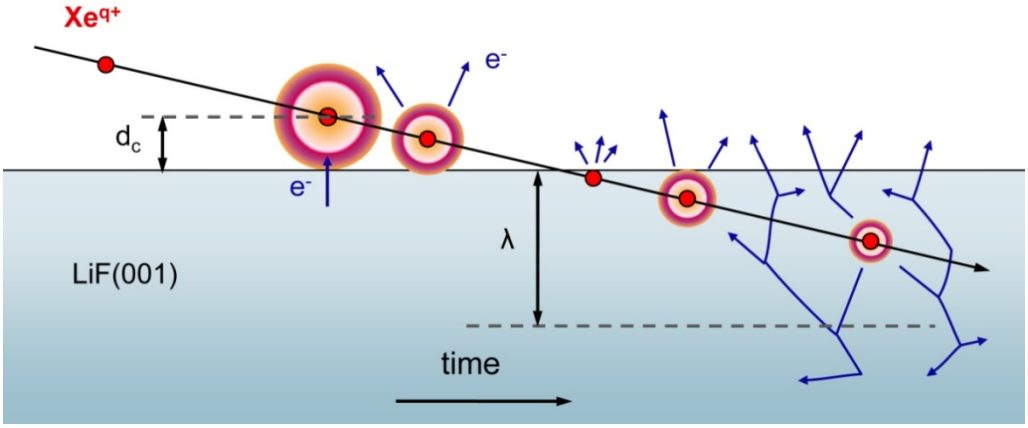

Fig. 4.2-25: High electron yields from insulators upon HCI impact at normal incidence are explained by a large sub-surface electron emission contribution. While there is insufficient time for a significant number of Auger-decays in front of the surface due to the small critical distance for first electron capture from the surface, the large mean free path λ of slow electrons in the solid together with a high chance for secondary electron production leads to many electrons emitted during the decay of the second generation hollow atom formed at the impact of the HCI on the surface.

The drop in electron yields found at very low impact velocities could then simply be interpreted as a shift from dominating sub-surface electron emission to the less efficient (due to the lack of secondary electron production) above-surface emission process. COB clearly predicts lower above-surface electron emission yields for the LiF surface compared to the gold surface. As more potential energy is already converted into emitted electrons in front of the surface at very low impact velocities due to the longer interaction time, the second generation hollow atom has less power to produce sub-surface electrons and the total yield drops (see Fig. 4.2-26).

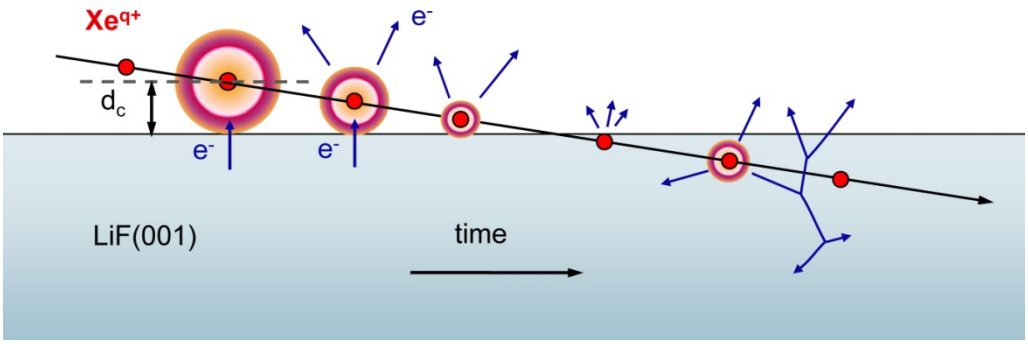

Fig. 4.2-26: At very low impact velocities, more time is available for the above surface electron emission process. This leaves the second generation hollow atom with less potential energy for the more efficient sub-surface emission process, leading to an overall drop of the electron yield.

This approach, however, falls short of explaining the charge state dependence of the electron yield drop. If the shift from sub-surface to above-surface emission was responsible for the observed

drop of electron yields at very low velocities, it should be more pronounced for lower charge states, as they have less total potential energy, and therefore a larger fraction of this energy can be converted into electrons in front of the surface for a given interaction time. The drop is in fact more pronounced for the highest available charge state, while for q = 20+ and 30+ the yields increase with charge state in a very similar fashion than for the gold surface (see Fig. 4.2-24). Therefore, another property of the insulator must be responsible for the observed electron yields.

The defining property of an insulator is its limited charge mobility. While a conducting surface can replace electrons captured into the approaching HCI almost instantly, so that the electric properties of the surface remain unchanged during the interaction process, an insulator surface will charge up. This charge patch makes it more difficult to collect additional electrons, as these have to be caught from deeper shells of the same atom, or from neighboring atoms which are farther away, increasing the potential barrier between surface and ion. It was even proposed that the charge patch formed during the interaction of the approaching HCI with an insulator surface can become large enough to overcome the attractive image charge potential of the still ionized projectile, so that this is reflected without actually hitting the surface (see chapter 2.1.2). This “trampoline effect” [39] would in principle explain the observed drop of electron yields at very low velocities for the highest charge states (see Fig. 4.2-27), as the sub-surface electron emission contribution would be lost completely.

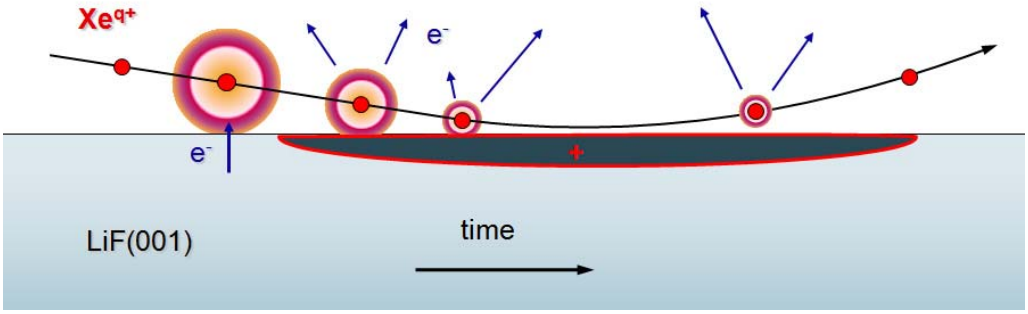

Fig. 4.2-27: The proposed trampoline effect predicts a charge patch formed on the insulator surface during the interaction with a very slowly approaching HCI. This charge patch would be strong enough to repel the projectile, therefore eliminating any sub-surface electron emission contributions.

Calculations by Solleder [146] have shown that even for the highest charge states used during this work, the repulsive potential from the charge patch formed on a LiF surface during HCI approach is not strong enough to overcome the (reduced) image charge attraction. Even when starting with no initial velocity, image charge acceleration is strong enough to accelerate the ion towards the surface, assuming realistic hole-hopping times for the charge mobility of the surface. Only with charge mobility completely neglected, the repulsive force gets into the right order of magnitude, but even then the “trampoline effect” would only show at higher charge states than those available experimentally during this work.

If the trampoline effect was responsible for the drop in yields, one would expect two distinct peaks in the statistics spectrum, as an individual ion cannot be partly reflected. One peak would stem from ions which are still fast enough to hit the surface and induce the below-surface cascade, as the relative energy distribution of the beam energy becomes very large at lowest velocities (c.f. Fig. 4.2-17 on page 82), and another (lower) contribution from successfully reflected “trampoline” ions. Such a splitting of the electron emission statistics has not been observed down to relative beam

energies per charge state of 4 eV/q (c.f. Fig. 4.2-16 on page 81), while the drop of electron yields starts already around 10 eV/q. Even if part of the population called “reflected ions” that is visible at lowest beam energies in Fig. 4.2-16 is due to the “trampoline effect”, that cannot explain the observed electron yield drop, as this part of the spectrum was not evaluated. The drop was observed considering only the shift of the main peak in the electron statistics spectrum.

One must therefore consider a third explanation, which also describes the drop in electron yield to the formation of a charge patch on the surface. But instead of the projectiles trajectory, the influence of this patch on the escaping electrons is thought to be responsible for the observed phenomena. The very strongly localized charge patch will have a significant influence on the electrical potential in the vicinity of the impact site. Calculations by Solleder have shown that even for high projectile charge states, surface charges are created mostly inside a cylindrical volume of 1 nm diameter and 1 nm depth [146]. Although the electrons are created at this positive potential and would still have enough energy to escape into infinity, the presence of the grounded target chamber will lead to a (relative to the origin of the electron) negative potential barrier between impact site and electron collection grid. Electrons with insufficient kinetic energy will be reflected onto the surface, thus reducing the measured electron yield. Electrons produced at the impact of the ion by promotion and peeling-off of previously captured and still highly excited electrons generally have very low energies and are especially prone for this effect (see Fig. 4.2-28). Electrons created via the sub-surface electron cascade are not necessarily produced very close to the charged region considering the high inelastic mean free path of slow electrons in LiF (see Fig. 4.2-29) and might therefore escape more easily.

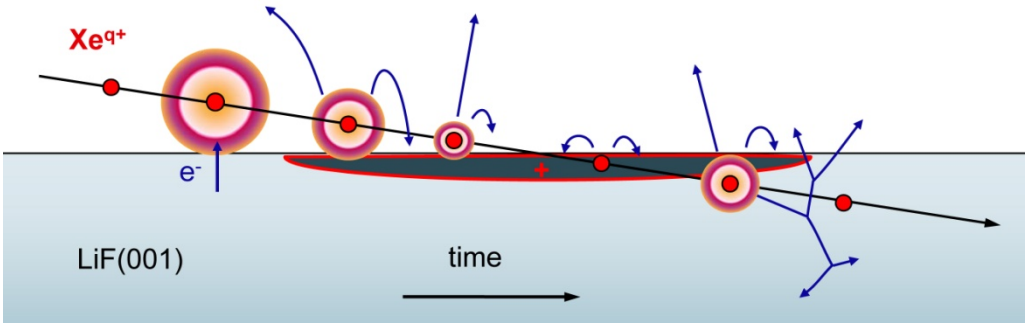

Fig. 4.2-28: A positive charge patch formed during the approach of a HCI on the insulting surface retains slow electrons otherwise emitted into vacuum. Secondary electrons from the sub-surface part of the interaction process are not necessarily produced very close to the impact site and might therefore still escape.

It has to be noted, that contrary to problems with insufficient electron collection geometry, this is not an apparatus effect, as the positive charge patch is formed by the HCI impact itself. Of course, in between any two ion impact events, the charges are replaced to prevent global charge-up of the surface.

Considering the available experimental evidence, only electron retention by a charge patch formed during impact can explain the appearance of the electron yield drop at very low velocities for the highest charge states. Extremely low velocity is required to allow ample time for the above-surface interaction process taking into account the very low critical distance for the LiF surface due to its high electron binding energy of 14 eV. Numerical simulations confirmed that for a highly charged ion like Ar^{17+} at intermediate velocities of a few tens of keV, only a small number of about 9 electrons

are emitted before the ion hits the surface, while the total measured electron yield for this case was over 80 [146]. At very low impact velocities, however, theory predicts an above surface electron emission contribution of 100 electrons for the case of Kr^{36+} impact on LiF, which should be comparable to the Xe^{40+} case. At lower charge states, even though the interaction time becomes sufficiently long, not enough positive charges are created at the surface to give rise to a potential barrier strong enough to retain slow electrons.

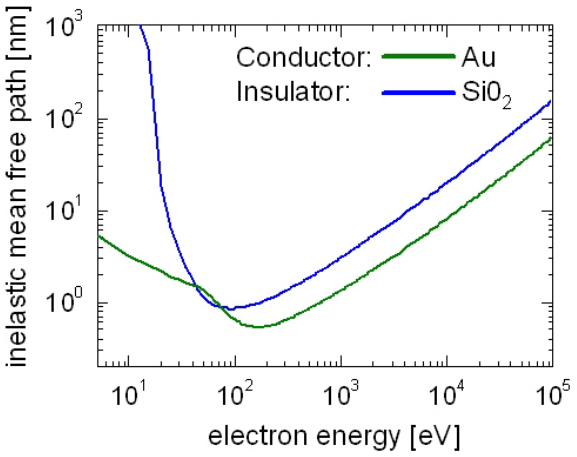

Fig. 4.2-29: Inelastic mean free path of slow electrons in conducting gold and a model insulator, SiO2. Inside the band gap of the insulator, the mean free path becomes extremely large. Picture from [1] using data provided by W. Werner.

4.2.5 Time Structure Analysis

Using the setup described in 4.1.5, the time structure of particle emission after HCI impact on insulating targets was measured. During the tests of the setup for time structure measurements of the electron emission from LiF and KBr, ion-ion auto-correlation spectra were obtained to analyze the time structure of the incident ion beam. For this purpose, both SCAs (creating the start and stop-signal for time measurement) were set to an energy window corresponding to the "main" events, i.e. more than 100 electrons created directly by the HCI impact. Fig. 4.2-30 shows a spectrum taken with Xe^{30+} on stainless steel. Although the EBIT was operated in leaky mode, supposedly providing a continuous beam, the ion-ion autocorrelation shows a distinctly peaked time structure instead of a smooth decreasing curve. This peak structure can only be explained with some kind of pulsed structure of the beam [3].

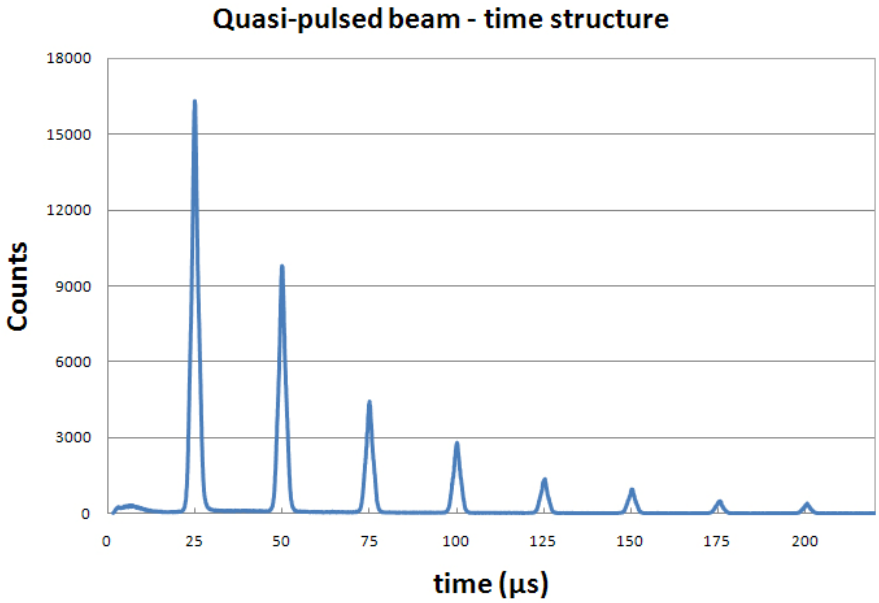

Fig. 4.2-30: Time structure spectrum of a supposedly leaky mode HCI beam from the EBIT at FZD. The spectrum was taken with a Xe^{30+} beam on steel. After any HCI impact at t = 0, the time until the next ion impact is almost exclusively a multiple of 26 µs. This mode of extraction was thus termed quasi-pulsed [3].

The most likely explanation for this behavior is that the trap potential of the EBIT (c.f. chapter 2.1.3) is not stable, but fluctuates with a frequency of ca 38 kHz thus letting small bunches of particles escape, which then form the "quasi-pulsed" ion beam. In this context, it should be mentioned that in the leaky mode of the Dresden EBIT-II, the voltage difference between an open and a completely closed trap for any given charge state is about 0.2 V. Thus a voltage drop as little as 0.01 V of the trap potential can indeed lead to a highly increased escape probability for trapped ions. Such fluctuations can e. g. originate from a capacitive or inductive coupling of one of the other devices near the drift tubes or connected to the same ground potential, like a turbo molecular pump. DC power supplies, as the one used for the trap potential, are also known to show some high-frequency ripples in the output signal which in this case seems to be the most likely cause of the fluctuations.

When the EBIT trap potential is lowered at regular time intervals by some of the mentioned disturbances, the chance for an ion escaping is much higher than usual. Between the windows of

opportunity created in this way, the chance of an ion leaving the trap goes down compared to a true leaky-mode beam, because ions which would have had the required temperature have already left the trap in the last window and some time is needed for another ion to gather the necessary temperature.

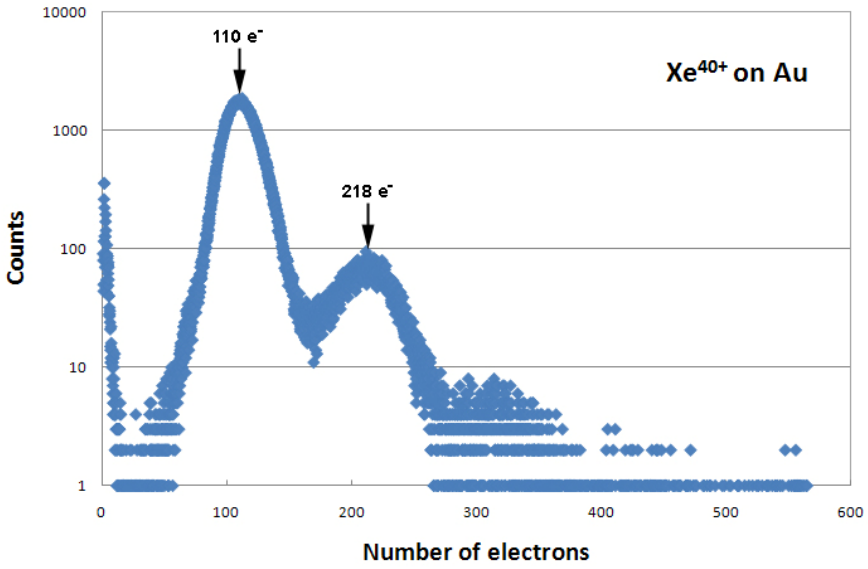

Fig. 4.2-31: Electron statistics spectrum of Xe^{40+} on gold. Apart from the main peak corresponding to a single ion hitting the target (yield approx. 110 e^-), there is a secondary peak due to the fact that two ions may leave the trap at the same time. When they hit the surface of the target within the time resolution of the detector, the number of electrons doubles (approx. 218 electrons) [3].

Due to the quasi-pulsed structure of the beam, there is a non-negligible probability that two or even more ions leave the trap at the same time (i.e. a small ion bunch). This leads to one or more secondary peaks in the electron statistics spectra taken with such quasi-pulsed beams (see Fig. 4.2-31 and Fig. 4.2-32).

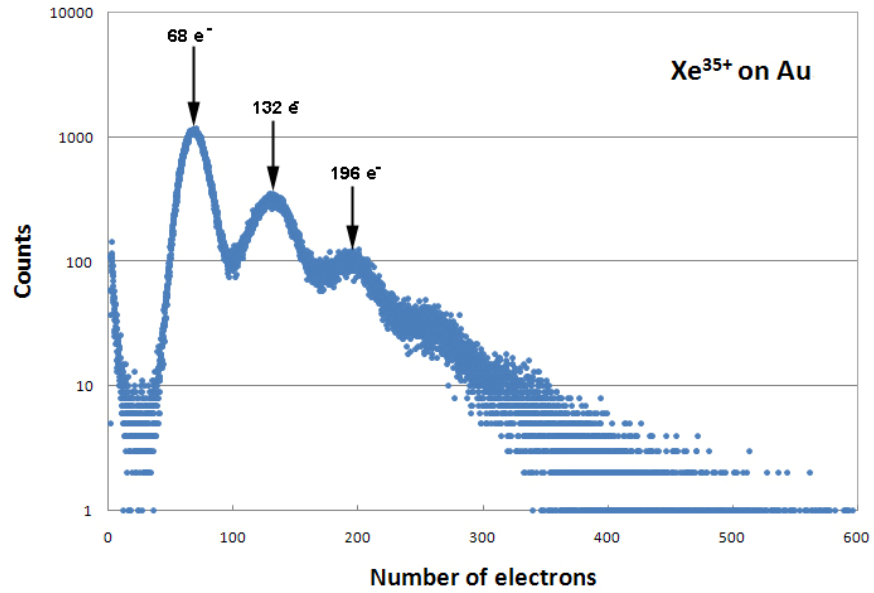

Fig. 4.2-32: Electron statistics spectrum of Xe^{35+} on gold. This spectrum shows even more than one secondary peak due to three or four ions leaving the trap at the same time [3].

This quite stable pulsed structure of the beam (with a time period of $t_{QP} \approx 26$ µs) proved to be a valuable asset in calibrating the spectra of the time-structure measurements of the electron emission. As the time t_{QP} between the peaks is constant, one can easily find $t = 0$ of the spectra, assuming an uncertainty of much less than t_{QP}. As the time-to-amplitude converter is actually able to measure nanosecond time delays, this assumption seems reasonable.

After this verification of the test setup and the unexpected insights gained in the time structure of the EBIT beam, the setup was changed to analyze the time structure of emitted particles after HCI impact. This investigation was triggered by an observation made with the electron statistics detector. Electron statistics spectra of HCI impact on insulating targets can roughly be divided into two regions of interest (see Fig. 4.2-33). The first represents events with many electrons emitted simultaneously as expected directly at HCI impact. The second is comprised of few electron events that represent the background signal, usually one of the following

- field emission (completely independent from the ion beam)
- Electron emission from the ion beam at locations where the collection efficiency is bad. This can be in front of the entry aperture, where the chance of even one electron passing the aperture and electron repeller are slim, or some place in the target chamber hit by ions that missed the target. As the collection potentials are optimized for the target, only a fraction of the emitted electrons at different locations in the chamber will be registered. (rate of these events should be proportional to the beam intensity)

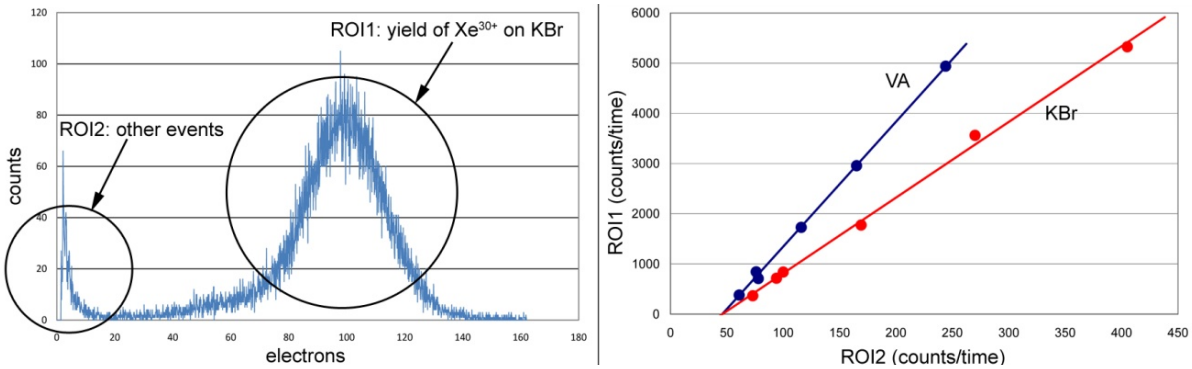

Fig. 4.2-33: left) Electron statistics spectra of HCI impact on insulating targets divided into two regions of interest (ROI). right) plotting the count rates in both ROI vs. each other for various different beam intensities, a material dependence of the background rate was observed. The background signal from the insulating KBr increases more with beam intensity than for the conducting stainless steel (VA) surface [3].

Plotting the count rates in both regions of interest vs. each other for various different beam intensities, a material dependence of the background rate was observed. This strongly suggests that some of the events found in the background signal are caused by the HCI impact on the insulator itself. As all particles registered within the time resolution of the setup (< 1 µs) are counted into the main peak, and the electron flight times in the detector setup are in the order of 10 ns, the first assumption was that some electrons are emitted significantly after the HCI impact on the surface. Electron impact on KBr and LiF is known to induce color centers (e.g. electrons trapped at the lattice site of a negative ion), which can then decay via electron emission some time later.

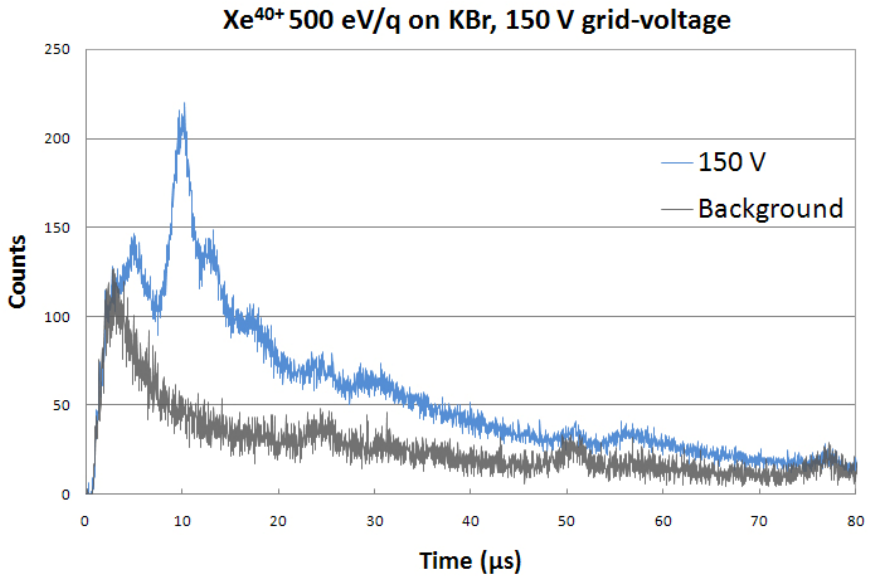

Fig. 4.2-34: Time structure spectrum of 500 eV/q Xe^{40+} impact on KBr taken at a grid voltage of 150 V (blue curve). Several distinct peaks are protruding from the background signal (grey) indicating low electron number events that are causally related to the HCI impact at t=0 [3].

To analyze the origin of the unidentified background signal, the setup was tuned to measure the time interval between high electron number events and the following low electron number events (see Fig. 4.2-34). To obtain a background spectrum, the heating of the target was turned off so that the insulating target would charge up (due to the bombardment with positively charged Xe-ions). Such a positively charged target (up to +200 V) lets no negative ion or slow electron escape from the target's surface hence all events registered by the detector do not originate from the target.

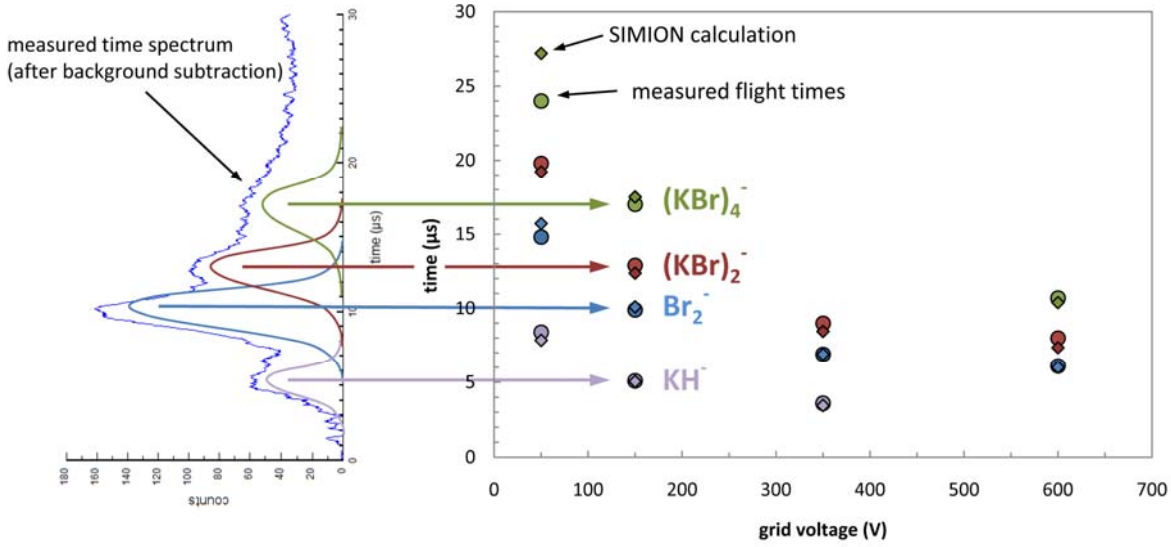

Fig. 4.2-35: The peaks in the time structure spectra (left, c.f. Fig. 4.2-34) of Xe^{40+} impact on KBr are found to depend on the applied grid voltage (right). SIMION calculations (diamonds) for target material ions and negatively charged clusters fit the observed delay times (circles) very well. Due to the relatively large uncertainties of the experiment and the ambiguous masses of K (m=39) and Br (m=80) the identification of the peaks can only be seen as preliminary [3].

These measurements verify the causal relationship of HCI impact and the background events, as only then a distinct time structure between the two is expected. However, further measurements showed that the observed delay times depend on the applied grid voltage (see Fig. 4.2-35), indicating that the delay times represent some sort of time-of-flight of particles inside the setup. Time of flight of electrons in our setup is extremely short (< 10 ns), so they can be excluded as the source of the additional background signal in electron statistics spectra.

The observed dependence of delay times on the grid voltage only makes sense for negative Potassium or Bromine ions and negatively charged KBr clusters created at the time of impact of the HCI on the KBr target. The observed delay times in the time structure spectra are then simply the flight times of the ion clusters from the target surface to the detector. Higher collection grid voltages mean higher potential difference between target and grid and thus higher velocities of the ions leading to a shorter time-of-flight. SIMION flight-time calculations confirmed this assumption, as the observed delay times for the different grid voltages are matched very well by the calculated flight times of the different negative ions.

"No fair, you changed the outcome by measuring it!"
Prof. Hubert Farnsworth of futurama,
after his race horse lost in a "quantum finish"

5 Conclusions and Outlook

The present study of the interaction of slow highly charged ions (HCI) with insulator surfaces was successful in demonstrating the capability for nanostructuring by exclusive means of the HCI's potential energy and significantly advanced the understanding of the fundamental electronic processes during impact. Apart from questions answered, the present work leads to the rise of a number of new questions, and a path is outlined for future work to investigate these.

Stable and truly topographic nanostructures were found on CaF_2 singly crystal surfaces after HCI bombardment. The structures were shown to be induced by the potential energy of single highly charged xenon ions. A threshold in the potential energy of the projectile between 12 and 14 keV was found for the onset of nanostructuring. Both the size of produced features and the threshold in potential energy were only weakly dependent on the projectile's kinetic energy. A comparison of the present results to studies on other materials revealed that – though the nature and size of the features differ greatly – potential energy thresholds are a general feature in nanostructuring with slow HCI.

A phase transition (melting) on the nano-scale was found to be responsible for the production of slow HCI induced nanostructures on CaF_2. Electrons emitted during the interaction of the projectile with the surface strongly heat a nanoscopic volume of the lattice. Apart from the onset of melting, a second threshold is expected when the deposited energy is sufficient for sublimation. Indeed a sudden increase in the evolution of hillock volume versus potential energy was observed around 50 keV – in excellent agreement with theoretical predictions. However, additional study of this phenomenon is necessary for two reasons: Firstly, the opening of the L-shell of xenon, the projectile ion, at exactly the threshold energy calls for the use of a different (heavier) projectile to exclude sub-shell effects in the experiment. Secondly, the second threshold was only observed at the highest kinetic energies and needs to be verified at very low impact velocities. The production of a decelerated beam of heavy ions with potential energies above 50 keV is ongoing work at the Heidelberg-EBIT right now, and can only be used for a follow-up work to this thesis.

The theoretical model developed for the case of HCI induced nanostructures on CaF_2 should be expanded to other materials where thresholds in potential energy were also found. A comprehensive model for the production of nanostructures using slow HCI seems in reach and needs to be refined and verified by an extension of experiments to different materials, systematically investigating the potential energy thresholds for different kinetic energies. Work is currently in progress for graphite (HOPG), mica, LiF and PMMA, a photo-resist commonly used in the production of microelectronics.

Using a new setup for the determination of electron yields during impact of slow HCI on insulating targets, the velocity dependence of electron yields was determined between virtually zero velocity and $7 \cdot 10^5$ ms^{-1}. Compared to conducting targets, only a weak dependence of the electron yield on the impact velocity was found above approximately $1 \cdot 10^5$ ms^{-1}. For the highest charge state

used (Xe^{40+}), a sharp drop of the electron yield was observed for the insulator at very low impact velocities. The retention of slow electrons by a positive charge patch formed on the surface during impact is discussed as a possible explanation for this drop. With the anticipated availability of decelerated beams of high charge state projectiles, this phenomenon can be further investigated in the future. Once the velocity dependence of the yield is better understood by theory, the self-image charge acceleration of HCI towards an insulating surface can be quantified by a study of the deviation of measured yields at extremely low velocities.

The construction of a setup for time-structure analysis of emitted particles led to the unexpected observation of negatively charged ions and clusters from a KBr surface during HCI impact. This technique can be improved to quantitatively measure negative ion yields and determine their mass-over-charge ratio as a by-product while measuring electron yields. By a change of detector bias to negative high voltage, positive secondary ions can also be detected. At extremely low impact velocities, reflected primary ions can be measured and their charge state resolved, allowing a test of the much-discussed trampoline-effect.

"So long, and thanks for all the fish!"
The hitchhiker's guide to the galaxy,
Douglas Adams

6 Acknowledgements

There can be no research without research funding, and the present work has especially benefitted from the generous support of Austrian and European Grants, which allowed for extensive travel to various research facilities that can provide slow highly charged ions. I therefore gratefully acknowledge the support of the Austrian Research Foundation FWF (Projects No. 17449 and M894-N02) as well as the European Projects ITS-LEIF (RII3#026015) and AIM (Contract No. 025646).

I feel extraordinarily lucky for the choice of my supervisor. Prof. Friedrich Aumayr has shown me the beauty of experimental physics from the moment on he instructed me to put together my first ultra-high vacuum setup. I was amazed by his ability to explain any remote physics problem I could come up with during lunch-breaks by means of his legendary "paper napkin" sketches.

I will always remember the late Prof. Hannspeter Winter, who had the ability to apply small and subtle changes to abstract or paper drafts that made such big improvements on the readability that I was often wondering if it was still the same text at all.

I am grateful to Prof. Joachim Burgdörfer, Christoph Lemell and Beate Solleder from the Institute for Theoretical Physics of the Vienna University of Technology for their contributions to this work. If the understanding of ion-insulator interactions has improved by this work, it is thanks to their insights and calculations. I thank all members of the theory group for the numerous shared lunch breaks and spent evenings.

I want to thank everybody from the workgroup of Prof. Aumayr at the Institut für Allgemeine Physik for making the past four years such a memorable and enjoyable time. Many of my colleagues have become close friends, especially the three students who participated in my work as their diploma theses. Martin Simon was my companion for many trips to the Heidelberg-EBIT in Germany. Not only was he so successful in figuring out the details of the extraction beamline that he was instantly hired by them as a PhD student, but he made our stays productive and fun by his intelligent and kind nature. One thing though, that we could never achieve, was efficient time management. After a few days of beam-time, we would always end up with one of us sleeping from 8 AM to noon, the other sleeping from 1 AM to supper, and both working through the nights. Robert Ritter came with me to Caen, France, where he introduced me to a dangerous hobby ("all in!") that will undoubtedly keep our friendship alive well beyond our time at the University. He called me his "elder brother" in his thesis, which is both an honor and a little weird - for he actually introduced me to atomic force microscopy. Daniel Winklehner helped the construction of the setup for electron yield measurements and put this to great use during our beam-times at the Forschungszentrum Dresden, Germany. Our trips were never boring, at least not for me, as he sometimes still smilingly complains about the long hours waiting for me to finish playing poker (the above mentioned hobby I picked up in Caen). Two project students contributed to the results presented here, Bernhard Kaiser and Alexander Zavarsky. I thank them both for their company, which was much appreciated.

Of my fellow PhD students at the Vienna University of Technology, I especially thank Artur Golczewski and Sylvicley Figueira da Silva for their friendship and support. Syl was my office-mate as well as a member of our band, and while we never actually made it to perform in public, our demo-songs will always remind me of the great time we had during jam-sessions. Artur was always ready to discuss results and theories during my work, even though his research topic was quite different from mine. I wish him the best of luck for his new career as a screenwriter - I anticipate great things from him, although I will surely beat his high-score on Singstar (Playstation) soon!

Ayman El-Said came to our group as a Post-Doc and brought with him his experience in swift-heavy-ion irradiation of insulating targets and a plan to try nanostructuring with slow highly charged ions. He kindly took me onto his project, which eventually turned out to be extremely successful. I thank him for his companionship and his insights into the many “Voodoo-like” tweaks one has to master to get good images with the atomic force microscope.

Christine Toupal-Pinter made the paperwork after beam-times a pleasure (at least less of a torture) by her effective and friendly way to deal with it. She is in a position where good work often goes unnoticed and only mistakes come to the surface, and I greatly appreciate that there were never any from her side – while she managed to correct a few of my own.

Representative for the whole EBIT group at the Max Planck Institute in Heidelberg, I thank José Crespo López-Urrutia, who has the rare ability to create an effective and work-intensive, but at the same time supportive and friendly environment. During my first visit, I felt I was in the Disneyland of Physics, not only for the great machinery they use, but for the great companionship of the people.

I am grateful to Stefan Facsko and Rene Heller from Forschungszentrum Dresden for their help and friendship. They set high standards for any type of user-facility: usually the ion-beam was already set-up and ready-to-go 10 minutes before we arrived. Rene showed me around into the local Poker-scene in Dresden, where we spent our evenings in bleak and smoke-filled rooms, having a great time.

For the ARIBE facility in Caen, I want to thank Prof. Bernd Huber and Christine Malot for their support. They are also the driving force behind the ITS-LEIF network, and their many hours invested into this project made my travels to research facilities so much easier.

I have been enjoying the love and support of my wife, Elfi, for the past 10 years. She has lifted me up when I was crushed by failed projects, she has forced me on when I was drifting away into idleness; she has been there to discuss the non-scientific problems of my work and has endured my talking about the scientific ones. For this and for much more I thank her.

I want to thank my mother, Senta, who has invested all her strength and energy into the education of her three sons after the untimely death of my father. During this difficult time, and ever since, she has always put us first. I am deeply grateful to her and can only hope that the successes I achieved will make her proud and happy. I thank her companion in life, Klaus, for giving her back the joyful life she has been robbed of and for planting the seeds of my interest in experimental work when he introduced me to carpentry when I was 14.

Finally, I thank Matt Groening, Scott Adams and Jorge Cham for creating such great series as Futurama, Dilbert and the PhD comics, lightening up my every day during the past 4 years.

7 References

[1] M. Simon, diploma thesis (Vienna University of Technology, Vienna, 2007)
[2] R. Ritter, diploma thesis (Vienna University of Technology, Vienna, 2008)
[3] D. Winklehner, diploma thesis (Vienna University of Technology, Vienna, 2008)
[4] A.S. El-Said, R. Heller, W. Meissl, R. Ritter, S. Facsko, C. Lemell, B. Solleder, I.C. Gebeshuber, G. Betz, M. Toulemonde, W. Möller, J. Burgdörfer, and F. Aumayr, Phys. Rev. Lett. **100**, 237601 (2008).
[5] W. Meissl, D. Winklehner, F. Aumayr, M.C. Simon, R. Ginzel, J.R. Crespo López-Urrutia, J. Ullrich, B. Solleder, and J. Burgdörfer, e-J. Surf. Sci. Nanotech. **6**, 54 (2008).
[6] F. Aumayr, A.S. El-Said, and W. Meissl, Nucl. Instrum. Methods Phys. Res. B **266**, 2729 (2008).
[7] C. Lemell, A.S. El-Said, W. Meissl, I.C. Gebeshuber, C. Trautmann, M. Toulemonde, J. Burgdörfer, and F. Aumayr, Solid State Electron. **51**, 1398 (2007).
[8] M. Fürsatz, W. Meissl, S. Pleschko, I.C. Gebeshuber, N. Stolterfoht, HP. Winter, and F. Aumayr, J. Phys. Conf. Ser. **58**, 319 (2007).
[9] A.S. El-Said, W. Meissl, M.C. Simon, J.R. Crespo Lopez-Urrutia, I.C. Gebeshuber, J. Laimer, HP. Winter, J. Ullrich, and F. Aumayr, Rad. Effects Def. Solids **162**, 467 (2007).
[10] A.S. El-Said, W. Meissl, M.C. Simon, J.R. Crespo Lopez-Urrutia, C. Lemell, J. Burgdörfer, I.C. Gebeshuber, HP. Winter, J. Ullrich, C. Trautmann, M. Toulemonde, and F. Aumayr, Nucl. Instrum. Methods Phys. Res. B **258**, 167 (2007).
[11] A.S. El-Said, W. Meissl, M.C. Simon, J.R. Crespo Lopez-Urrutia, I.C. Gebeshuber, M. Lang, HP. Winter, J. Ullrich, and F. Aumayr, Nucl. Instrum. Methods Phys. Res. B **256**, 346 (2007).
[12] W. Meissl, M.C. Simon, J.R. Crespo López-Urrutia, H. Tawara, J. Ullrich, HP. Winter, and F. Aumayr, Nucl. Instrum. Methods Phys. Res. B **256**, 520 (2007).
[13] W. Meissl, M.C. Simon, J.R. Crespo Lopez-Urrutia, H. Tawara, J. Ullrich, HP. Winter, and F. Aumayr, Rev. Sci. Instrum. **77**, 093303 (2006).
[14] F. Aumayr, J. Stöckl, M. Fürsatz, W. Meissl, and HP. Winter, e-J. Surf. Sci. Nanotech. **4**, 388 (2006).
[15] D. Hasselkamp, in *Particle Induced Electron Emission II*, edited by G. Höhler (Springer, Heidelberg, 1992), Vol. 123, p. 1
[16] J. Schou, Scanning Microsc. **2**, 607 (1988).
[17] M. Rösler and W. Brauer, in *Particle Induced Electron Emission I*, edited by G. Höhler (Springer, Berlin, 1991), Vol. 122.
[18] R. Baragiola, in *Chap. IV in Low energy Ion-Surface Interactions*, edited by J.W. Rabalais (Wiley, 1993).
[19] P. Sigmund, (Mat.Fys.Medd., Copenhagen, 1993), Vol. 43, p. 2.
[20] H. Gnaser, *Low-Energy Ion Irradiation of Solid Surfaces* (Springer Berlin, 1999).
[21] H.D. Hagstrum, Phys.Rev. **96**, 325 (1954).
[22] H.D. Hagstrum, Phys.Rev. **96**, 336 (1954).
[23] A. Arnau, F. Aumayr, P.M. Echenique, M. Grether, W. Heiland, J. Limburg, R. Morgenstern, P. Roncin, S. Schippers, R. Schuch, N. Stolterfoht, P. Varga, T.J.M. Zouros, and HP. Winter, Surf. Sci. Reports **27**, 113 (1997).
[24] H. Winter, Physics Reports **367**, 387 (2002).
[25] F. Aumayr and HP. Winter, in *Slow Heavy-Particle Induced Electron Emission from Solid Surfaces*, edited by J. Burgdörfer and H. Winter (Springer, Berlin, Heidelberg, 2007), Vol. 225, p. 79.
[26] T. Neidhart, F. Pichler, F. Aumayr, HP. Winter, M. Schmid, and P. Varga, Phys. Rev. Lett. **74**, 5280 (1995).
[27] M. Sporn, G. Libiseller, T. Neidhart, M. Schmid, F. Aumayr, HP. Winter, P. Varga, M. Grether, and N. Stolterfoht, Phys. Rev. Lett. **79**, 945 (1997).
[28] F. Aumayr and HP. Winter, Phil. Trans. Roy. Soc. (London) **362**, 77 (2004).
[29] R. Heller, S. Facsko, R.A. Wilhelm, and W. Moller, Phys. Rev. Lett. **101**, 096102 (2008).

[30] F. Watt, A. Bettiol, J. van Kan, E. Teo, and M. Breese, Int. J. Nanoscience **4** (2005).
[31] S. Facsko, T. Dekorsy, C. Koerdt, C. Trappe, H. Kurz, A. Vogt, and H. Hartnagel, Science **285**, 1551 (1999).
[32] M. Castro, R. Cuerno, L. Vázquez, and R. Gago, Phys. Rev. Lett. **94** (2005).
[33] B. Ziberi, F. Frost, T. Höche, and B. Rauschenbach, Phys. Rev. B **72**, 7 (2005).
[34] E. Akcöltekin, T. Peters, R. Meyer, A. Duvenbeck, M. Klusmann, I. Monnet, H. Lebius, and M. Schleberger, Nature Nanotechnology **2**, 290 (2007).
[35] J. Burgdörfer, P. Lerner, and F.W. Meyer, Phys. Rev. A **44**, 5674 (1991).
[36] J. Burgdörfer and C. Lemell, in *Slow Heavy-Particle Induced Electron Emission from Solid Surfaces*, edited by J. Burgdörfer and HP. Winter (Springer, Berlin, Heidelberg, 2007), Vol. 225, p. 1.
[37] J. Burgdörfer, in *Fundamental Processes and Applications of Atoms and Ions*, edited by C.D. Lin (World Scientific, Singapore, 1993).
[38] F. Aumayr and HP. Winter, e-J. Surf. Sci. Nanotech. **1**, 171 (2003).
[39] J.P. Briand, S. Thuriez, G. Giardino, G. Borsoni, M. Froment, M. Eddrief, and C. Sébenne, Phys. Rev. Lett. **77**, 1452 (1996).
[40] J.P. Briand, L. de Billy, P. Charles, S. Essabaa, P. Briand, R. Geller, J.P. Desclaux, S. Bliman, and C. Ristori, Phys. Rev. Lett. **65**, 159 (1990).
[41] R. Morgenstern and J. Das, Europhysics News **25**, 3 (1994).
[42] HP. Winter and F. Aumayr, J.Phys.B:At.Mol.Opt.Phys. **32**, R39 (1999).
[43] HP. Winter and F. Aumayr, Euro. Phys. News **33**, 215 (2002).
[44] H. Winter, Europhys.Lett. **18**, 207 (1992).
[45] H. Winter, C. Auth, R. Schuch, and E. Beebe, Phys. Rev. Lett. **71**, 1939 (1993).
[46] F. Aumayr, H. Kurz, D. Schneider, M.A. Briere, J.W. McDonald, C.E. Cunningham, and HP. Winter, Phys. Rev. Lett. **71**, 1943 (1993).
[47] F.W. Meyer, L. Folkerts, H.O. Folkerts, and S. Schippers, Nucl. Instrum. Methods Phys. Res. B **98**, 441 (1995).
[48] C. Lemell, HP. Winter, F. Aumayr, J. Burgdörfer, and F.W. Meyer, Phys. Rev. A **53**, 880 (1996).
[49] L. Wirtz, C. Lemell, C.O. Reinhold, L. Hägg, and J. Burgdörfer, Nucl. Instrum. Methods Phys. Res. B **182**, 36 (2001).
[50] L. Wirtz, C.O. Reinhold, C. Lemell, and J. Burgdörfer, Phys. Rev. A **67**, 12903 (2003).
[51] V.A. Morozov, F.W. Meyer, and P. Roncin, Phys. Scr. **T80**, 69 (1999).
[52] D. Schneider, D. DeWitt, M.W. Clark, R. Schuch, C.L. Cocke, R. Schmieder, K.J. Reed, M.H. Chen, R.E. Marrs, L. M, and R. Fortner, Phys. Rev. A **42**, 3889 (1990).
[53] T. Schenkel, A.V. Hamza, A.V. Barnes, and D.H. Schneider, Progr. Surf. Sci. **61**, 23 (1999).
[54] L.P. Ratliff, E.W. Bell, D.C. Parks, A.I. Pikin, and J.D. Gillaspy, Appl. Phys. Lett. **75**, 590 (1999).
[55] G. Hayderer, S. Cernusca, M. Schmid, P. Varga, HP. Winter, and F. Aumayr, Phys. Scripta **T92**, 156 (2000).
[56] N. Nakamura, M. Terada, Y. Nakai, Y. Kanai, S. Ohtani, K. Komaki, and Y. Yamazaki, Nucl. Instrum. Methods Phys. Res. B **232**, 261 (2005).
[57] M. Terada, N. Nakamura, Y. Nakai, Y. Kanai, S. Ohtani, K. Komaki, and Y. Yamazaki, Nucl. Instrum. Methods Phys. Res. B **235**, 452 (2005).
[58] M.A. Levine, R.E. Marrs, J.R. Henderson, D.A. Knapp, and M.B. Schneider, Phys. Scr. **T22**, 157 (1988).
[59] E.D. Donets, Phys. Scr. **T3**, 11 (1983).
[60] D. Schneider, M.W. Clark, B. Penetrante, J. McDonald, D. DeWitt, and J.N. Bardsley, Phys. Rev. A **44**, 3119 (1991).
[61] J. Gillaspy, (NOVA Science Publisher Inc., 1999).
[62] P. Beiersdorfer, H. Chen, D.B. Thorn, and E. Träbert, Phys. Rev. Lett. **95**, 233003 (2005).
[63] A. Lapierre, U.D. Jentschura, J.R.C. López-Urrutia, J. Braun, G. Brenner, H. Bruhns, D. Fischer, A.J.G. Martínez, Z. Harman, W.R. Johnson, C.H. Keitel, V. Mironov, C.J. Osborne, G.

Sikler, R.S. Orts, V. Shabaev, H. Tawara, I.I. Tupitsyn, J. Ullrich, and A. Volotka, Phys. Rev. Lett. **95**, 183001 (2005).
[64] A.J. González Martínez, J.R. Crespo López-Urrutia, J. Braun, G. Brenner, H. Bruhns, A. Lapierre, V. Mironov, R. Soria Orts, H. Tawara, M. Trinczek, and J. Ullrich, Phys. Rev. Lett. **94**, 203201 (2004).
[65] J. Gillaspy, *Trapping Highly Charged Ions: Fundamentals and Applications* (NOVA Science Publisher Inc., 2000).
[66] F. Currell, *The Physics of Multiply and Highly Charged Ions - Vol. 2: Interactions with Matter* (Kluwer Academic Pub., Dordrecht/NL, 2003).
[67] J.R. Crespo López-Urrutia, B. Bapat, B. Feuerstein, D. Fischer, H. Lörch, R. Moshammer, and J. Ullrich, Hyperfine Interact. **146/147**, 109 (2003).
[68] A.J. González Martínez, PhD thesis (Ruperto-Carola Universität, Heidelberg, 2005)
[69] F. Grossmann, R. Heller, M. Kreller, U. Kentsch, S. Landgraf, V.P. Ovsyannikov, M. Schmidt, F. Ullmann, and G. Zschornack, Nucl. Instrum. Methods Phys. Res. B **256**, 565 (2007).
[70] V.P. Ovsyannikov and G. Zschornack, Rev. Sci. Instrum. **70**, 2646 (1999).
[71] G. Zschomack, R. Heller, M. Kreller, S. Landgraf, F. Grossmann, U. Kentsch, V.P. Ovsyannikov, M. Schmidt, and F. Ullmann, Review of Scientific Instruments **77**, 03A904 (2006).
[72] J.F. Ziegler, J.P. Biersack, and U. Littmark, *The Stopping and Range of Ions in Matter* (Pergamon, New York, 1985).
[73] G. Schiewietz, E. Luderer, G. Xiao, and P.L. Grande, Nucl. Instrum. Methods Phys. Res. B **175**, 1 (2001).
[74] W.M. Arnoldbik, N. Tomozeiu, and F.H.P.M. Habraken, Nucl. Instrum. Methods Phys. Res. B **203**, 151 (2003).
[75] F. Aumayr and HP. Winter, Nucl. Instrum. Methods Phys. Res. B **233**, 111 (2005).
[76] C. Müller, A. Benyagoub, M. Lang, R. Neumann, K. Schwartz, M. Toulemonde, and C. Trautmann, Nucl. Instrum. Methods Phys. Res. B **209**, 175 (2003).
[77] C. Müller, M. Cranney, A.S. El-Said, N. Ishikawa, A. Iwase, M. Lang, and R. Neumann, Nucl. Instrum. Methods Phys. Res. B **191**, 246 (2002).
[78] N. Khalfaoui, C.C. Rotaru, S. Bouffard, M. Toulemonde, J.P. Stoquert, F. Haas, C. Trautmann, J. Jensen, and A. Dunlop, Nucl. Instrum. Methods Phys. Res. B **240**, 819 (2005).
[79] A.S. El-Said, M. Cranney, N. Ishikawa, A. Iwase, R. Neumann, K. Schwartz, M. Toulemonde, and C. Trautmann, Nucl. Instrum. Methods Phys. Res. B **218**, 492 (2004).
[80] A.S. El-Said, R. Neumann, K. Schwartz, and C. Trautmann, Rad. Eff. Def. Sol. **157**, 649 (2002).
[81] G. Binning, C.F. Quate, and C. Gerber, Phys. Rev. Lett. **56**, 930 (1986).
[82] A.S. El-Said, F. Aumayr, S. Della-Negra, R. Neumann, K. Schwartz, M. Toulemonde, C. Trautmann, and K.O. Voss, Nucl. Instrum. Methods Phys. Res. B **256**, 313 (2007).
[83] R.L. Fleischer, P.B. Price, and R.M. Walker, J. Appl. Phys. **36**, 3645 (1965).
[84] H. Dammak, A. Dunlop, D. Lesueur, A. Brunelle, S. Della-Negra, and Y. Le Beyec, Phys. Rev. Lett. **74** 1135 (1995).
[85] L.T. Chadderton, Radiation Measurements **36**, 13 (2003).
[86] C. Trautmann, K. Schwartz, and O. Geiss, J. Appl. Phys. **83** (1998).
[87] K. Schwartz, C. Trautmann, A.S. El-Said, R. Neumann, M. Toulemonde, and W. Knolle, Phys. Rev. B **70**, 184104 (2004).
[88] C. Trautmann, M. Toulemonde, J.M. Costantini, J.J. Grob, and K. Schwartz, Phys. Rev. B **62**, 13 (2000).
[89] M. Boccanfuso, A. Benyagoub, K. Schwartz, C. Trautmann, and M. Toulemonde, Nucl. Instrum. Methods Phys. Res. B **191**, 301 (2002).
[90] I. Manika, J. Maniks, K. Schwartz, M. Toulemonde, and C. Trautmann, Nucl. Instrum. Methods Phys. Res. B **209**, 93 (2003).
[91] D. Lesueur and A. Dunlop, Rad. Eff. Def. Sol. **126**, 163 (1993).
[92] M. Toulemonde, C. Dufour, and E. Paumier, Phys. Rev. B **46**, 14362 (1992).

[93] D.H. Schneider, M.A. Briere, J. McDonald, and J. Biersack, Rad.Eff.Def.Solids **127**, 113 (1993).
[94] C. Ruehlicke, M.A. Briere, and D.H. Schneider, Nucl. Instrum. Methods Phys. Res. B **99**, 528 (1995).
[95] D.C. Parks, M.P. Stöckli, E.W. Bell, L.P. Ratliff, R.W. Schmieder, F.G. Serpa, and J.D. Gillaspy, Nucl. Instrum. Methods Phys. Res. B **134**, 46 (1998).
[96] D.C. Parks, R. Bastasz, R.W. Schmieder, and M. Stöckli, J. Vac. Sci. Technol. B **13**, 941 (1995).
[97] D. Schneider, M.A. Briere, M.W. Clark, J. McDonald, J. Biersack, and W. Siekhaus, Surf.Sci. **294**, 403 (1993).
[98] I.C. Gebeshuber, S. Cernusca, F. Aumayr, and HP. Winter, Int. J. Mass Spectrom. Ion Proc. **229**, 27 (2003).
[99] J. Liu, R. Neumann, C. Trautmann, and C. Müller, Phys. Rev. B **64**, 184115 (2001).
[100] K. Mochiji, S. Yamamoto, H. Shimizu, S. Ohtani, T. Seguchi, and N. Kobayashi, J.Appl.Phys. **82**, 6037 (1997).
[101] T. Meguro, A. Hida, Y. Koguchi, S. Miyamoto, Y. Yamamoto, H. Takai, K. Maeda, and Y. Aoyagi, Nucl. Instrum. Methods Phys. Res. B **209**, 170 (2003).
[102] R. Minniti, L.P. Ratliff, and J.D. Gillaspy, Phys. Scripta **T92**, 22 (2001).
[103] M. Tona, H. Watanabe, S. Takahashi, Y. Fujita, T. Abe, S. Jian, N. Nakamura, N. Yoshiyasu, C. Yamada, M. Sakurai, and S. Ohtani, J. Phys. Conf. Ser. **58**, 331 (2007).
[104] M. Tona, H. Watanabe, S. Takahashi, N. Nakamura, N. Yoshiyasu, M. Sakurai, T. Terui, S. Mashiko, C. Yamada, and S. Ohtani, Surf. Sci. **601**, 723 (2007).
[105] M. Tona, H. Watanabe, S. Takahashi, N. Nakamura, N. Yoshiyasu, M. Sakurai, T. Terui, S. Mashiko, C. Yamada, and S. Ohtani, Nucl. Instrum. Methods Phys. Res. B **256**, 543 (2007).
[106] M. Tona, H. Watanabe, S. Takahashi, N. Nakamura, N. Yoshiyasu, M. Sakurai, C. Yamada, and S. Ohtani, Nucl. Instrum. Methods Phys. Res. B **258**, 163 (2007).
[107] J. Stöckl, T. Suta, F. Ditroi, HP. Winter, and F. Aumayr, Phys. Rev. Lett. **93**, 263201 (2004).
[108] H. Kurz, F. Aumayr, C. Lemell, K. Töglhofer, and HP. Winter, Phys. Rev. A **48**, 2182 (1993).
[109] C. Lemell, J. Stöckl, J. Burgdörfer, G. Betz, HP. Winter, and F. Aumayr, Phys. Rev. Lett. **81**, 1965 (1998).
[110] J. Burgdörfer and F.W. Meyer, Phys. Rev. A **47**, R20 (1993).
[111] H. Eder, F. Aumayr, and HP. Winter, Nucl. Instrum. Methods Phys. Res. B **154**, 185 (1999).
[112] H. Winter, Progr. Surf. Sci. **63**, 177 (2000).
[113] M. Vana, F. Aumayr, P. Varga, and HP. Winter, Nucl. Instrum. Methods Phys. Res. B **100**, 284 (1995).
[114] L. Hägg, C.O. Reinhold, and J. Burgdörfer, Phys. Rev. A **55**, 2097 (1997).
[115] L. Hägg, C.O. Reinhold, and J. Burgdörfer, in *Photonic, Electronic and Atomic Collisions*, edited by F. Aumayr and H. Winter (World Scientific Publ. Ltd, Singapore, 1998), p. 683
[116] L. Wirtz, G. Hayderer, C. Lemell, J. Burgdörfer, L. Hägg, C.O. Reinhold, P. Varga, HP. Winter, and F. Aumayr, Surf.Sci **451**, 197 (2000).
[117] M. Vana, F. Aumayr, P. Varga, and HP. Winter, Europhys. Lett. **29**, 55 (1995).
[118] N. Stolterfoht, J.H. Bremer, V. Hoffmann, R. Hellhammer, D. Fink, A. Petrov, and B. Sulik, Phys. Rev. Lett. **88**, 133201 (2002).
[119] T. Ikeda, Y. Kanai, T.M. Kojima, Y. Iwai, T. Kambara, Y. Yamazaki, M. Hoshino, T. Nebiki, and T. Narusawa, Appl. Phys. Lett. **89**, 163502 (2006).
[120] K. Schiessl, W. Palfinger, K. Tokesi, H. Nowotny, C. Lemell, and J. Burgdorfer, Phys. Rev. A **72**, 062902 (2005).
[121] G. Binning, H. Rohrer, C. Gerber, and E. Weibel, Appl. Phys. Lett **40**, 178 (1982).
[122] G. Friedbacher and H. Fuchs, Pure Appl. Chem. **71** (1999).
[123] F. Aumayr, G. Lakits, and HP. Winter, Appl.Surf.Sci. **47**, 139 (1991).
[124] L. Wirtz, J. Burgdörfer, M. Dallos, T. Müller, and H. Lischka, Phys. Rev. A **68**, 032902 (2003).
[125] C.P. Bhalla, Phys. Rev. A **8**, 2877 (1973).

[126] A. Barany and C.J. Setterlind, Nucl. Instrum. Methods Phys. Res. B **98**, 184 (1995).
[127] J.P. Albert, C. Jouanin, and C. Gout, Phys. Rev. B **16**, 925 (1977).
[128] M. Toulemonde, C. Dufour, A. Meftah, and E. Paumier, Nucl. Instrum. Methods Phys. Res. B **166/167**, 903 (2000).
[129] U. Kentsch, H. Tyrroff, G. Zschornack, and W. Möller, Phys. Rev. Lett. **87**, 105504 (2001).
[130] G. Grochtmann, R.J. Meyer, F. Peters, and L. Gemlin, *Gmelins Handbuch der anorganischen Chemie* (Verlag Chemie, Berlin, 1970).
[131] M. Toulemonde, W. Assmann, C. Dufour, A. Meftah, F. Studer, and C. Trautmann, Mat. Fys. Med. Dan. Vid. Selsk. **52**, 263 (2007).
[132] J.D. Gillaspy, D.C. Parks, and L.P. Ratliff, J. Vac. Sci. Technol. B **16**, 3294 (1998).
[133] J.M. Pomeroy, H. Grube, A.C. Perrella, and J. Gillaspy, Appl. Phys. Lett. **91**, 073506 (2007).
[134] G. Lakits, F. Aumayr, and HP. Winter, Rev. Sci. Instrum. **60**, 3151 (1989).
[135] H. Eder, M. Vana, F. Aumayr, and HP. Winter, Rev. Sci. Instrum. **68**, 165 (1997).
[136] C. Lemell, J. Stöckl, HP. Winter, and F. Aumayr, Rev. Sci. Instrum. **70**, 1653 (1999).
[137] D. Kost, S. Facsko, W. Moller, R. Hellhammer, and N. Stolterfoht, Phys. Rev. Lett. **98**, 225503 (2007).
[138] F. Aumayr, H. Kurz, HP. Winter, D. Schneider, M.A. Briere, J.W. McDonald, and C.E. Cunningham, Rev. Sci. Instrum. **64**, 3499 (1993).
[139] I.G. Hughes, J. Burgdörfer, L. Folkerts, C.C. Havener, S.H. Overbury, M.T. Robinson, D.M. Zehner, P.A. Zeijlmans van Emmichhoven, and F.W. Meyer, Phys. Rev. Lett. **71**, 291 (1993).
[140] H. Kurz, F. Aumayr, D. Schneider, M.A. Briere, J.W. McDonald, and HP. Winter, Phys. Rev. A **49**, 4693 (1994).
[141] H. Kurz, F. Aumayr, C. Lemell, K. Töglhofer, and HP. Winter, Phys. Rev. A **48**, 2192 (1993).
[142] B. Svensson and G. Holmén, J. Appl. Phys. **52**, 6928 (1981).
[143] L.A. Dietz and J.C. Sheffield, Rev. Sci. Instrum. **44**, 183 (1973).
[144] K. Tökési, D. Varga, L. Kövér, and Mukoyama, Spectr. Rel. Phenom. **76** (1995).
[145] M. Hattass, T. Schenkel, A.V. Hamza, A.V. Barnes, M.W. Newman, J.W. McDonald, T.R. Niedermayr, G.A. Machicoane, and D.H. Schneider, Phys. Rev. Lett. **82**, 4795 (1999).
[146] B. Solleder, PhD thesis (Vienna University of Technology, Vienna, 2008)

LEBENSLAUF

Walter Meissl

AUSBILDUNG

2005 - 2008 Technische Universität Wien

Doktoratsstudium

- Gebiet: Das Verhalten von Isolatoroberflächen beim Beschuss mit langsamen hochgeladenen Ionen

2000 - 2005 Technische Universität Wien

Diplomstudium (2. Abschnitt)

- Dipl.-Ing. (mit Auszeichnung) am 14. April 2005
- Diplomarbeit zur numerischen Plasmasimulation für eine Satellitenmission der europäischen Weltraumorganisation (ESA)

2002 International Space University

ISU Summer Session Program ´02

- 2-monatiges Sommerstudium zu weltraumrelevanten Themen
- abgehalten am California Polytechnical Institute in L.A. (USA)

1997 - 2000 Technische Universität Graz

Diplomstudium (1. Abschnitt)

- 1998 12-monatige Unterbrechung wegen Zivildienst

1989 - 1997 Gymnasium Carnerigasse, Graz

AHS (humanistischer Zweig)

- Matura mit Auszeichnung

BERUFSERFAHRUNG

2005 - 2008 Technische Universität Wien

Projektassistent

- wissenschaftliche Tätigkeit im Rahmen der Dissertation

2003 - 2005 Austrian Research Centers in Seibersdorf

freier Mitarbeiter

- wissenschaftliche Tätigkeit im Rahmen der Diplomarbeit

SPRACHEN

- Deutsch (Muttersprache)
- Englisch (fließend)
- Japanisch (Anfänger)

Wien, 29. Oktober 2008 Walter Meissl